Mémoire

Auteur : Schmidt, Vincent
Promoteur(s) : Alvera Azcarate, Aida; Barth, Alexander
Faculté : Faculté des Sciences
Diplôme : Master en sciences spatiales, à finalité approfondie
Année académique : 2022-2023
URI/URL : http://hdl.handle.net/2268.2/18684

University of Liège

Faculty of Sciences

Department of Astrophysics, Geophysics and Oceanography

Master thesis

Multivariate detection and propagation speed of planetary Rossby waves from satellite observations of the equatorial Pacific Ocean

---

A thesis presented for the degree of Master in Space Sciences by

Vincent SCHMIDT

under the supervision of Aida ALVERA-AZCÁRATE and Alexander BARTH

and committee: Jean-Marie BECKERS, Louis FRANÇOIS, Guy MUNHOVEN

Academic year 2022-2023

Abstract

Theme: Multivariate detection and propagation speed of planetary Rossby waves from satellite observations of the equatorial Pacific Ocean.

Supervisors: Aida ALVERA-AZCÁRATE and Alexander BARTH

Rossby waves propagate in the ocean because of the Earth's rotation and the stratification of water layers, and they can take several months to cross an oceanic basin like the Pacific Ocean. These planetary Rossby waves can be measured with satellite data thanks to their signature at the oceanic surface.

After introducing the planetary waves, I recall theoretical concepts useful to their study. Then, I detail a reduced gravity model with 2 active layers as a refinement of the most common model with 1 active layer, presenting the dispersion relations for the different types of oceanic equatorial waves. Next I present several data sets from satellites in remote sensing (sea surface height and temperature), obtained during the last 30 years to detect the presence of planetary Rossby waves in the equatorial Pacific Ocean. So the propagation speed is determined by using Hovmöller diagrams and the technique of the Radon transform. Indeed, I developed during my master thesis a tool to detect planetary Rossby waves and calculate their speed. Possible changes in the propagation speed on a decadal scale are suggested, due to possible changes in the stratification. The influence of climatic events like El Niño or La Niña is also presented in comparison with the oceanic Niño index.

Finally, a discussion on the propagation speeds of planetary waves completes the conclusive section and perspectives to this work are proposed. The Rossby waves were first studied in atmospheric geophysics, then in oceanography, and in astrophysics nowadays.

Keywords: planetary waves, satellite observations, propagation speed, climatic events, physical oceanography, remote sensing.

Résumé

Thème: Détection multivariée et vitesse de propagation des ondes planétaires de Rossby à partir d'observations satellites dans l'océan pacifique équatorial.

Promoteurs: Aida ALVERA-AZCÁRATE et Alexander BARTH

Les ondes de Rossby se propagent dans l'océan grâce à la rotation de la Terre et la stratification des couches d'eau, et elles peuvent prendre plusieurs mois à traverser un bassin océanique comme l'Océan Pacifique. Ces ondes planétaires de Rossby peuvent être mesurées avec des données satellitaires grâce à leur signature à la surface de l'océan.

Après avoir introduit les ondes planétaires, je rappelle des concepts théoriques utiles à leur étude. Puis, je détaille un modèle à gravité réduite à 2 couches actives comme raffinement au modèle plus courant à 1 couche active, en présentant les relations de dispersion pour les différents types d'ondes équatoriales océaniques. Je présente ensuite plusieurs jeux de données issues des satellites en télédétection (hauteur et température à la surface de l'océan), obtenues pendant les derniers 30 ans, pour détecter la présence des ondes planétaires de Rossby en Océan Pacifique équatorial. La vitesse de propagation est alors déterminée en utilisant des diagrammes de Hovmöller et la technique de la transformée de Radon. En effet, j'ai développé pendant mon mémoire un outil numérique pour détecter les ondes planétaires de Rossby et calculer leur vitesse. De possibles changements dans la vitesse de propagation des ondes à l'échelle décennale sont suggérés, dus à d'éventuels changements dans la stratification. L'influence des événements climatiques comme El Niño ou La Niña est aussi présentée en comparaison avec l'indice de Niño océanique.

Pour finir, une discussion sur les vitesses de propagation des ondes planétaires complète la section conclusive et des perspectives à ce travail sont proposées. Les ondes de Rossby ont d'abord été étudiées en géophysique de l'atmosphère, puis en océanographie, et le sont également en astrophysique de nos jours.

Mots-clés: ondes planétaires, observations satellitaires, vitesse de propagation, événements climatiques, océanographie physique, télédétection.

Abbreviations

ATSR/ERS-1 : Along-track scanning radiometer / ESA remote sensing series-1
AVHRR : Advanced very high resolution radiometer
CMEMS : Copernicus Marine Environment Monitoring Service
ECMWF : European Centre for Medium-range Weather Forecasts
ERM : Exact Repeat Mission
GFO : Geosat Follow On
MetOp-A : Meteorological Operational satellite-A
NOAA : National Oceanic and Atmospheric Administration
SeaWiFS : Sea-viewing wide field of view sensor
TOPEX/Poseidon : Topographic experiment / radar altimeter

CHL : chlorophyll
ENSO : El Niño - Southern Oscillation
ITCZ : intertropical convergence zone
SSH : sea surface height
SSS : sea surface salinity
SST : sea surface temperature
WSC : wind stress curl

Bu : Burger number
Fr : Froude number
Ro_T : temporal Rossby number
Ro : Rossby number
Ek : Ekman number

Acknowledgements

Contents

1 Introduction: planetary waves

In the Solar System where we distinguish the main star (the Sun), eight planets (Mercury, Venus, Earth, Mars, Jupiter, Saturn, Uranus, Neptune), their moons and small bodies (like dwarf planets, comets, asteroids). The planets occupy an important place: with their specific elliptic orbits around their star, their synodic rotation periods and their physical properties, the planets are interesting targets to study various natural phenomena. Several points need to be discussed if we want to compare a particular phenomenon on different planets in a planetological perspective. First, for terrestrial planets like the Earth, the rotation period is a single value, but for gas giant planets like Jupiter, the differential rotation phenomenon (variation of the rotation period from the equator to the pole) also occurs. Thus the local latitude is an important parameter for rotation. An especially interesting feature for Jupiter is the presence of the Great Red Spot in its atmosphere (HIDE 1968) which is a large-scale phenomenon (PEDLOSKY 1987, CUSHMAN-ROISIN & BECKERS 2010) studied by geophysical fluid dynamics. A second point is the density of the propagating medium of the waves: on the Earth, the atmosphere (air density $\sim 1.3 kg/m^3$), the density is low compared to in the ocean (water density $\sim 1024 kg/m^3$). Consequently this has an impact on the vertical layers of fluid and the stratification, with an interface at the sea surface, and meteorologists usually study both, as the ocean-atmosphere system. So we expect different time scales and velocities of the waves, propagating in the air or in water. Here the focus is on oceanic waves, not on atmospheric waves. A third point is the range of temperatures at the surface of the planets (hotter near the star, colder beyond the snowline): if we are interested by the presence of oceans on the planets, for the icy bodies, the surface consists mainly of ice and oceans are possible only in depth (scientists think there are subsurface oceans on Europa, Ganymede, Titan, Enceladus, Dione and ongoing missions like JUICE by ESA and Europa Clipper by NASA will confirm or infirm this hypothesis). This happens because matter like water is in liquid phase only in a certain range of values for the density, pressure and temperature, as illustrated in a classical phase diagram.

In our planet the Earth, the Pacific Ocean is the largest ocean basin and certainly one of the more interesting places to study oceanic planetary waves. It is latitudinally divided in the North Pacific Ocean and the South Pacific Ocean, and is bounded by Asia and Oceania in the west and America in the east.

In the past, signatures of planetary waves were detected in the Pacific Ocean with remote sensing satellites using different variables: sea surface height (SSH) with satellite altimetry like Geosat/ERS-1 or TOPEX/Poseidon or Jason series (Jacobs et al. 1993, Belonenko et al. 2016), sea surface temperature (SST) with ATSR on the ERS-1 satellite (Hill, Robinson, Cipollini 2000), sea surface salinity (SSS) with Aquarius satellite (Belonenko et al. 2018), chlorophyll (CHL) with SeaWiFS GAC level 3 data from NASA-GSFC DAAC (Killworth 2004), wind stress curl (WSC) with data from the European Centre for Medium-range Weather Forecasts (ECMWF) (White et al. 1998) but also in the Atlantic Ocean, in the South Indian Ocean (Subrahmanyam et al. 2009, Menezes et al. 2014, Banks et al. 2016) and in the South Antarctic Ocean (Belonenko et al. 2020). The satellite observations of planetary waves are discussed mainly in section 4. I will study planetary waves in a narrow region of the Pacific Ocean, around the equator: [10°N, 10°S] and [150°E, 80°W]. This region is framed in Fig. 1. I will look at temporal changes in the propagation speed of these waves in function of the latitude near the equator during the period 1993-2022. Other classical types of waves also occur in the equatorial Pacific Ocean: Kelvin waves, mixed gravity-planetary Yanai waves, inertia-gravity Poincaré waves (LeBlond & Mysak 1978, Cushman-Roisin & Beckers 2010), but I focus here only on planetary Rossby waves.
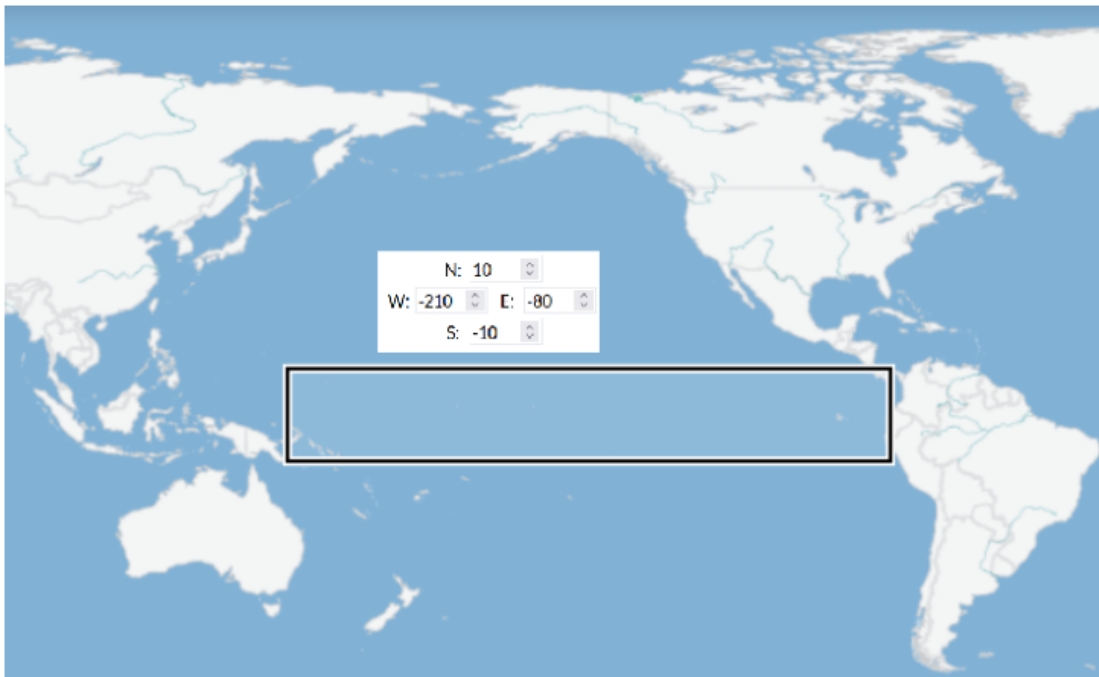
Fig. 1 – Map of the Earth surface where the region of interest in the equatorial Pacific Ocean is framed.

These waves were studied (among others) by Carl-Gustav ROSSBY who published one famous paper about the zonal circulation of the atmosphere (ROSSBY et al. 1939) and a bit after about the propagation of frequencies and energy in oceanic and atmospheric waves (ROSSBY 1945). He developed some important concepts in geophysical fluid dynamics like the radius of deformation or the propagation of planetary waves who currently bear his name. In short, the Rossby radius of deformation is the distance covered by a wave during one inertial period (modulo a 2π factor) and the propagation of planetary Rossby waves is westward along lines of constant latitude. The planetary Rossby waves cause variations of the sea surface height, transport energy and influence the weather.

The oceanic circulation is particular around the equator in the Pacific Ocean: there are ocean surface currents (the north equatorial current, the equatorial countercurrent and the south equatorial current) with surface convergence zones which produce downwelling and surface divergence zones which produce upwelling, but right on the equator there is a strong eastward current (the equatorial undercurrent). Fig. 2 shows the main currents in the eastern equatorial Pacific Ocean, as a map (a) and as a diagrammatic section (b).

Let us notice that the thermocline depth is greater at $10°S$ of latitude than at $10°N$ of latitude, due to the north equatorial countercurrent (NECC). The eastward equatorial undercurrent (EUC) is strong with velocities up to $1m/s$ and it is typically situated from about $50m$ to $200m$ depth (VALLIS 2017).

In fact, the intertropical convergence zone (ITCZ) generally associated with the zone of highest surface temperature is not situated perfectly at $0°$ of latitude, but slightly on the north (this is because there is a much greater proportion of land in the N hemisphere than in the S hemisphere). Around the ITCZ, the Hadley circulation in the atmosphere (direct Hadley cell between $0°$ and $30°$ N/S of latitude) is such that the trade winds blow to the west in the equatorial zone. But the greater is the speed of the wind, the greater is the wind stress acting on the sea surface and the stronger are the surface currents generated. The equatorial divergence associated to these winds produces a strong upwelling and seasonal variations of the trade winds modify the position of the ITCZ during the year.
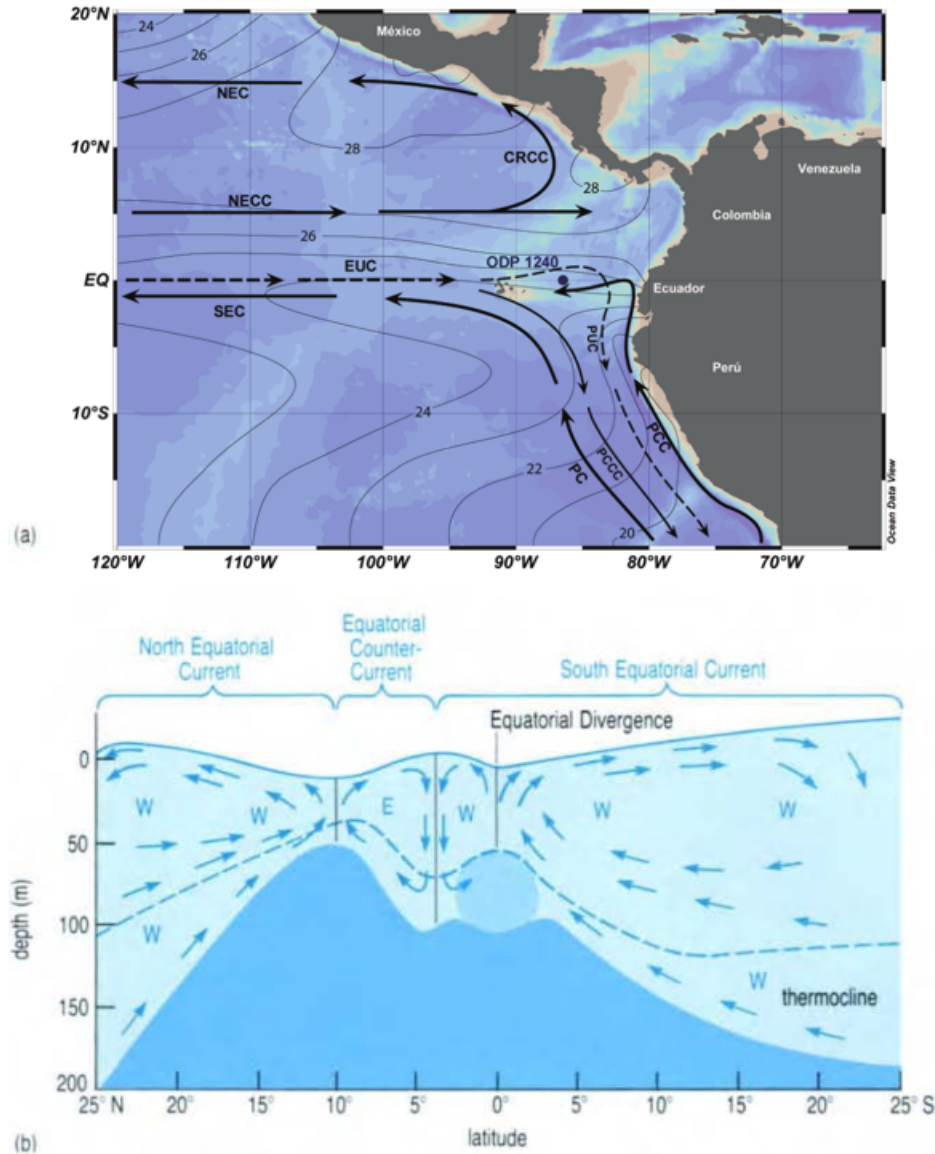
Fig. 2 – Illustration of the main surface and sub-surface currents in the eastern equatorial Pacific Ocean. Top (a): Map of these currents, where we distinguish the North Equatorial Current (NEC), the North Equatorial Counter-Current (NECC), the Costa Rica Coastal Current (CRCC), the Equatorial Undercurrent (EUC), the South Equatorial Current (SEC), the Peru Undercurrent (PUC), the Peru Current (PC), the Peru Coastal Current (PCC), and the Peru-Chile Counter-Current (PCCC). Black isotherms represent annual average temperature and the black dot corresponds to the Ocean Drilling Program (ODP) site 1240 were scientists studied coccolithophore assemblages (Carbarcos et al. 2014). Bottom (b): Diagrammatic section with the main currents in equatorial latitudes. The letters E and W indicate eastward and westward flow. The geostrophic current is assumed to be zero in the bottom darker blue region which is situated below the thermocline. The medium blue disc at 0° of latitude at about $100m$ depth represents the Equatorial Undercurrent (Colling 2004).

The equatorial countercurrent is thus located between $4°N$ and $10°N$ in the Pacific Ocean, and is due to the convergence zone around $4°N$ and the divergence zone around $10°N$, giving rise to an horizontal gradient of pressure driving a

geostrophic current towards the E (COLLING 2004, KLINGER & HAINE 2019). The equatorial undercurrent (also referred as the Cromwell current) is particular because it is below the influence of wind and it was studied (PEDLOSKY 1987) with a simple 2-layer model whose lower layer corresponds to the undercurrent, where potential vorticity is conserved, including nonlinearities. It is based on a previous work (BRYDEN & BRADY 1985) where the authors used a 3D circulation model of the upper equatorial Pacific Ocean, in the narrow region [5°N, 5°S] and [150°W, 110°W]. In the Pacific Ocean, at larger latitudes, we find the subtropical gyres (clockwise in the N hemisphere and anticlockwise in the S hemisphere) between $10°$ and $40°$ of latitude which contribute to the large-scale circulation, with associated currents (like the Kuroshio current along the islands of Japan). The planetary Rossby waves are here studied assuming a flat bottom in the ocean basin. If we take into account the topography, then we speak about topographic planetary waves in a stratified ocean, but because of the bottom boundary condition, the separation of the equations into barotropic and baroclinic modes is then no longer possible (LEBLOND & MYSAK 1978). In this master thesis, we assume a flat bottom. We also do not consider the lateral boundary effects, like wave reflection or trapping by an escarpment or by seamounts and islands. Some papers (CHELTON et al. 2000, LEE et al. 2012, YIN et al. 2014) also discuss tropical instability waves which propagate westward in the Pacific Ocean and their relation to El Niño/La Niña events: these waves are absent during El Niño events and become vigorous especially during La Niña events. The relation between planetary waves and the climatic events like El Niño-Southern Oscillation (ENSO) is discussed in section 5.

Planetary waves move slowly in the ocean at a speed of a few cm/s. As an example, the propagation speed of baroclinic Rossby waves at $9-15°N$ in the Pacific Ocean was estimated at $v \sim 20cm/s$ (ABE et al. 2014), this is lower than the speed of the Gulf Stream in the Atlantic Ocean estimated at $v \sim 100cm/s$ or the speed of the Kuroshio Current in the Pacific Ocean. Barotropic planetary waves (density is only a function of pressure, just rotation is important) move more rapidly than baroclinic planetary waves (stratification and rotation are important) which take months to cross an ocean basin at low latitudes, and years to decades at higher latitudes. Comparison between theory and satellite observations on the speed of waves were done in the Atlantic and Pacific basins (KILLWORTH & BLUNDELL 1999). Some scientists remarked that the observed speed is mainly faster than the speed given by the standard linear

theory (Chelton & Schlax 1996, Killworth et al. 1997). Outside the equatorial zone, the wave speed reduces with increasing latitude and this latitude dependence of speed can be compared with theoretical predictions. The wave speed also varies with longitude: in general, it increases toward the west of ocean basins (Hill, Robinson, Cipollini 2000), but this aspect could not be investigated in this master thesis, because the Radon transform needs a large range of longitudes to give good results. The space-time Hovmöller plots and the Radon transform (Robinson 2010) can be applied to obtain the alignment of planetary waves signatures and determine graphically the propagation speed. This is discussed in the section 5. In the atmosphere, the scale of planetary waves is of the order of thousands of km and in the ocean, their scale is of the order of hundreds of km.

The Rossby waves were also detected in astrophysical bodies (stars, including our Sun) other than Earth. Known as r-modes (r- for rotation, in contrast to p-modes with p- for pressure and g-modes with g- for gravity) begun also studied since an article from 45 years ago (Papaloizou & Pringle 1978) and the astronomy & astrophysics research currently continues (Provost et al. 1981, Saio et al. 2018, Damiani et al. 2020, Albekioni et al. 2023) in particular in asteroseismology (the upstream theory is quite similar to the geophysical viewpoint, but the propagation of these modes in stars acts also radially and not only at the surface of the stellar bodies). These r-modes are observed through the changes in luminosity in stellar light curves with space missions and surveys, like CoRoT, Kepler, TESS, and PLATO in the future years. It is certainly very interesting to study stellar modes and waves in these bodies, but our planet remains actually the only one in our Solar System with liquid water on its surface (there are icy satellites of Jupiter and Saturn which possibly include a big interior ocean but it is covered by ice on the surface, consequently satellite altimetry will not be the more suitable way to study it). I think this is a chance to have such a surface ocean of water on our planet and the development of remote sensing devices (in particular satellites) is the occasion to study it.

The Rossby waves are also an importance on the climate, in particular in atmospheric geophysics: they help the heat transfer from the tropical latitudes to the poles. This can explain features of polar variability. Atmospheric Rossby waves permit to study the temperature fluctuations during a large period, pro-

viding evidence that global warming (which is complex because of multiple scales of processes) occurs. This is of importance in climate change. Oceanic Rossby waves induce ocean-atmosphere exchanges at equatorial latitudes and mid-latitudes, by dispersing the energy across ocean basins. There is also a connection between the variation of oceanic Rossby waves and the intensity of El Niño/La Niña events in the Pacific Ocean.

We will try to answer the three following questions in this master thesis:
1. How to detect by satellite observations the presence of planetary Rossby waves in the ocean?
2. How to compare a theoretical model with the satellite observations about the propagation speeds of baroclinic planetary waves?
3. How to quantify the possible changes in the propagation speed with the latitude, on a decadal scale, or in regard with climatic events?

The organisation of the next sections is the following. In section 2, I review the theoretical background on planetary waves, discussing the rotation and stratification, the beta-plane approximation, the vorticity conservation principle, the baroclinic deformation radius and the dispersion relation. In section 3, I develop a multi-layered reduced gravity model to estimate theoretically the propagation speed of baroclinic planetary waves. In section 4, I focus on the satellite observations of planetary waves, through sea surface height and sea surface temperature detection approach, then I introduce the Hovmöller diagram and the 2D Radon transform, leading to my results on the observed speeds. In section 5, I discuss El Niño and La Niña events in the El Niño-Southern Oscillation climate pattern. In section 6, I conclude by a discussion on the propagation speed of planetary waves and on Rossby waves, with possible perspectives of this master thesis.

2   Theoretical background

Before diving into the modelling of planetary waves and the satellite detection of planetary waves, we need to introduce in this section some concepts that will be useful for the further understanding.

The theory of geostrophic dynamics and quasi-geostrophic planetary waves is explained in reference books (Chap 3 and 6 of PEDLOSKY 1987, Chap 5 of VALLIS 2006, Chap 9 and 16 of CUSHMAN-ROISIN & BECKERS 2010) about geophysical fluid dynamics.

Let us write the velocity in cartesian components by $\vec{v} = (u, v, w)$ and denote corresponding velocity scales by U in the horizontal and W in the vertical.

2.1   Rotation and stratification

Let us introduce two important concepts for this master thesis: rotation and stratification.

The *rotation* is principally due to the motion of a celestial body around one particular axis. If we assume that the rotation rate is constant (there is in reality a small variation, but it is negligible at human lifetime), it is usually characterized by a constant value Ω which is the Earth's angular rotation rate. In this thesis, we will preferably use f_0 which is the reference Corolis parameter. Indeed, when we consider a frame of reference in rotation, it is non-inertial and we need to add pseudo-forces (these are in fact pseudo-accelerations, so we will denote here $\vec{a}_{Cor}$ for the Coriolis acceleration) because of this rotation in the equations of motion.

By denoting $\vec{r'}$ the position vector relative to the rotating reference frame, $\vec{v'}$ the velocity vector relative to the rotating reference frame and $\vec{a'}$ the acceleration vector relative to the rotating reference frame, this acceleration is linked to the inertial acceleration by

$$\vec{a'} \;=\; \vec{a}_{in} - \vec{a}_{Cor} - \vec{a}_{fug} \tag{1}$$

where $\vec{a}_{in}$ is the inertial acceleration, $\vec{a}_{Cor} = -2\vec{\Omega} \times \vec{v'}$ is the Coriolis acceleration and $\vec{a}_{fug} = \vec{\Omega} \times (\vec{\Omega} \times \vec{r'})$ is the centrifugal acceleration.

The horizontal component of the Coriolis term $2\Omega\left(v\,sin(\phi) - w\,cos(\phi)\right)$ is orthogonal to the velocity over the Earth surface, where ϕ is the latitude. We usually define $f_0 \;=\; 2\Omega\,sin(\phi)$ as the reference Coriolis parameter and

$\tilde{f_0} = 2\,\Omega\,cos(\phi)$ as the reciprocal Coriolis parameter. So exactly at the equator $(\phi = 0)$, this term is zero.

In geophysical fluid dynamics, the rotation is important and if we neglect the dissipation effects (no viscosity terms), the equations of motion are modified by

$$\rho_0 \left(\frac{du}{dt} - f_0\,v + \tilde{f_0}\,w \right) = -\partial_x p \tag{2}$$

$$\rho_0 \left(\frac{dv}{dt} + f_0\,u \right) = -\partial_y p \tag{3}$$

$$\rho_0 \left(\frac{dw}{dt} - \tilde{f_0}\,u \right) = -\partial_z p - \rho\,g \tag{4}$$

where ρ_0 is the reference fluid density, p is the pressure and g is the gravity. Let us notice that the centrifugal acceleration term was absorbed in the gravitational acceleration: the effective gravitational force per unit volume (sum of the true gravitational force and the centrifugal pseudo-force) is $\rho\,g$ in norm and it is directed vertically downward. In this last term, $\rho = \rho_0 + \rho'$ is the fluid density which varies (instead of ρ_0 which is a constant) as the term ρ' is the variation due to the stratification and small fluid motions.

By examining the relative importance of the various terms, we will neglect the terms involving $\tilde{f_0}$, but we keep the terms involving f_0: because large-scale flows are nearly 2D ($W << U$), we get $\Omega\,W << \Omega\,U$, where W is the vertical velocity scale and U is the horizontal velocity scale. These flows are also shallow ($H << L$), where H and L are the vertical and horizontal length scales. In the equation (8), the left-hand side terms are negligible and we recover the hydrostatic balance.

To account the relative importance of the rotation, we define the Rossby number as $Ro = \dfrac{U}{\Omega\,L}$ and the temporal Rossby number as $Ro_T = (\Omega\,T)^{-1}$, where T is the temporal scale. If we also take into account viscosity effects with the kinematic eddy viscosity ν, we define the Eckman number as $Ek = \dfrac{\nu}{f_0\,H^2}$. Usually Ek is small (except in a boundary layer).

The *stratification* is principally due to the gravitation force which is directed to the center of mass of a celestial body. A stratified fluid consists of fluid parcels of various densities (lower densities being found above higher densities). This stratification, which is mostly vertical, affects the fluid velocity. When there is

also an horizontal component in the stratification, it can lead to instabilities or to coastal upwelling as near a coast.

From the equation

$$\frac{d^2 h}{dt^2} + N^2 h = 0 \tag{5}$$

where h is the height, the coefficient N^2 can be positive or negative. When it is positive, oscillations of frequency N are solutions of this equation, but when it is negative, growing exponentials (which imply an instability like convection) are solutions of this equation. We usually define the Brunt-Väisälä frequency by

$$N^2 = -\frac{g}{\rho_0} \frac{d\rho}{dz}$$

when $d\rho/dz < 0$ and sometimes we will mention its square root N as the stratification frequency.

In this case, when a fluid parcel is displaced upward, it is heavier than its surroundings and it has a vertical velocity. It then reaches its original height and continues to be displaced downward, so it is now lighter than its surroundings and it then reaches its original height. By buoyancy, the fluid parcel has oscillations at frequency N around its equilibrium height.

To account the relative importance of the stratification, we define the Froude number as $Fr = \frac{U}{N H}$.

Let's remark that when the Burger number [1] is of order unity, $\left(\frac{\Omega}{N}\right)^2 = \left(\frac{H}{L}\right)^2$, Ω being the Earth's angular rotation rate and N being the square root of the Brunt–Väisälä frequency, H being the vertical length scale and L being the horizontal length scale, with generally $H << L$, thus this is a small factor.

So when both rotation and stratification influence on the same order the fluid flow, the horizontal length scale takes a particular value $L = (N H)/\Omega$. In the atmosphere, its typical value is $L \sim 500 km$ for a vertical length scale of $H \sim 1km$, and in the ocean, its typical value is $L \sim 50km$ for a vertical length scale of $H \sim 100m$ (CUSHMAN-ROISIN & BECKERS 2010).

---

[1]The Burger number Bu is a measure of stratification in presence of rotation. It is the square of the Rossby number $Ro = U/(\Omega L)$ divided by the Froude number $Fr = U/(N H)$, where U is the horizontal velocity scale.

2.2 Beta-plane approximation

If there is a small perturbation y/R_e of the latitude

$$\phi = \phi_0 + y/R_e$$

where R_e is the mean Earth radius, the Coriolis parameter also has a small variation and by a Taylor series, $f = 2\,\Omega\,sin(\phi_0) + 2\,\Omega\,y/R_e\,cos(\phi_0) + ...$ So by keeping the first two terms, we get $f = f_0 + \beta_0\,y$.

This is the beta-plane approximation, where the coefficient in the second term is $\beta_0 = 2\,(\Omega/R_e)\,cos(\phi_0)$. This coefficient is called the beta parameter. The Cartesian framework where the beta term is neglected is called the *f-plane* and that where it is retained is called the *beta-plane* (CUSHMAN-ROISIN & BECKERS 2010).

If the term $\beta_0\,y$ is small compared to the term f_0, the beta-plane approximation can be used at mid-latitudes. But the region where this approximation is really important is the equatorial region. Along the equator, the reference Coriolis parameter is zero. So the terms $f_0\,u$ and $f_0\,v$ in the equations of motion disappear. This is the case in the tropical regions. But if there is no horizontal Coriolis Force, the currents are not geostrophically balanced, and there is a difference between the tropical and extra-tropical regions. In the expression of the beta term, y measures the meridional distance from the equator line. So, along the equator, we get $f = 0 + \beta_0\,y$ and this is called the equatorial beta-plane approximation. Consequently, in this approximation, we add the terms $-\beta_0\,y\,v$ and $+\beta_0\,y\,u$ in the equations of motions and we get

$$\rho_0\left(\frac{du}{dt} - \beta_0\,y\,v\right) = -\partial_x p \tag{6}$$

$$\rho_0\left(\frac{dv}{dt} + \beta_0\,y\,u\right) = -\partial_y p \tag{7}$$

$$0 = -\partial_z p - \rho\,g \tag{8}$$

Let us notice that usually we use the sea surface elevation variable $\eta = b + h - H$ where b is the bottom elevation above a reference level, h is the instantaneous fluid layer height and H is the constant depth from a reference surface, or simply the height h instead of the pressure p in these equations.

The beta-plane approximation is necessary in the wave theory to derive the

planetary Rossby wave solutions, which historically appear during last century to explain the motion of mid-latitude weather patterns.

2.3 Vorticity conservation principle

The vorticity is defined as the rotational of the velocity.

$$\zeta \;=\; \zeta_0 + \zeta_z + \zeta_p \tag{9}$$

In general, the total vorticity ζ consists in three parts: first the relative vorticity $\zeta_0 = \partial_x v - \partial_y u$, next the vertical stretching term ζ_z and then the planetary vorticity $\zeta_p = \beta_0 y$ coming from the beta-plane approximation $f = f_0 + \beta_0 y$.

When there is no vertical streatching term, the vorticity conservation principle writes simply (with the local fluid layer thickness h):

$$\frac{dq}{dt} = \frac{\partial_x v - \partial_y u + f}{h} = 0 \tag{10}$$

The potential vorticity $q = \zeta/h$ is conserved only if we neglect dissipation: if we consider dissipation, the are additional terms on the right hand side of this equation. The potential vorticity can be interpreted as circulation per volume.
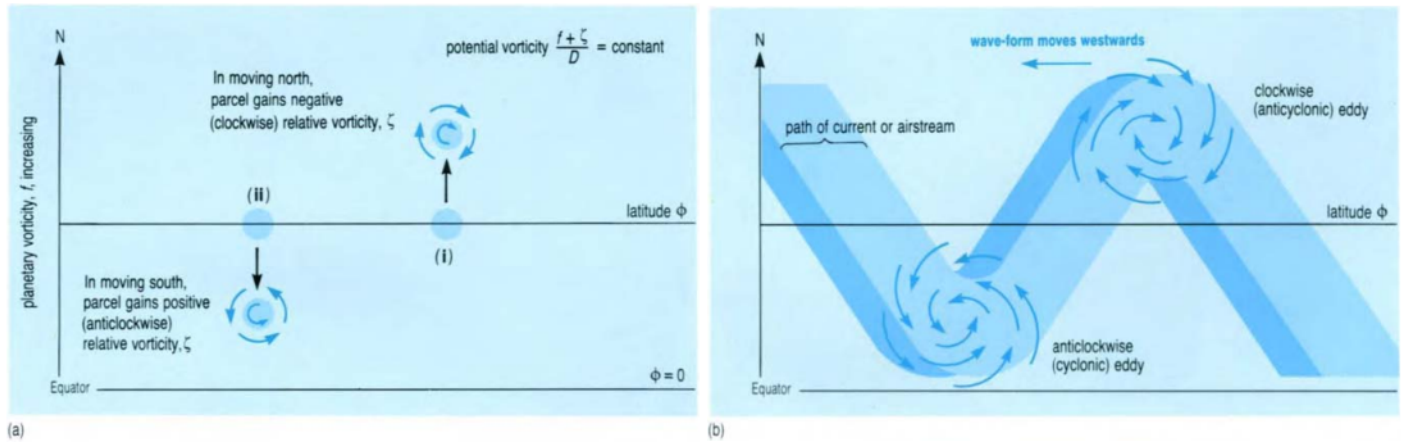
Fig. 3 – Diagram showing that the conservation of potential vorticity implies a westward propagation of planetary waves. (a): a parcel of air or water oscillates about a line of latitude while gaining and losing relative vorticity. (b): a path taken by a current affected by a planetary wave, with cyclonic and anticyclonic eddies along a line of latitude (COLLING 2004).

Basically, the mechanism of planetary waves is related to the conservation of potential vorticity. Let's imagine a parcel of air or water at latitude ϕ in the Northern hemisphere. D denotes the depth, f denote the planetary vorticity & ζ denote the relative vorticity. By the conservation principle (equation (10)),

the quantity $q = \dfrac{f + \zeta}{D}$ must be a constant. What happens if initially $\zeta = 0$ (no rotational motion relative to the Earth) and the parcel of air or water is displaced equatorwards or polewards? Because f varies with ϕ, it will acquire positive ζ and will rotate anticlockwise to compensate the loss in f if it moves equatorwards to the south or negative ζ and will rotate clockwise to compensate the gain in f if it moves polewards to the north (Fig. 3 (a)). Then, let's imagine a row of such air or water parcels flowing in a current along a line of latitude ϕ. If the flow is displaced equatorwards or polewards, oscillations corresponding to planetary waves occur around the original line of latitude, with the cyclonic eddies and the anticyclonic eddies pushing air or water to the west (Fig. 3 (b)). If we assume there is no strong current directed to the east, these planetary waves move as usual westwards.

The vorticity conservation principle is important because of the squeezing of the water column, producing an oscillation. The Rossby waves can exist only in the presence of an ambient potential vorticity gradient (Pedlosky 1987).

2.4 Deformation radii in the Pacific Ocean

In the introduction, we defined the Rossby radius of deformation as the distance covered by a wave during one inertial period. This is $R = c/f$ at speed c.

In the f-plane, the internal and external deformation radii are:

$$R_{int} = \frac{N\,H}{f_0} \quad , \quad R_{ext} = \frac{(g\,H)^{1/2}}{f_0} \tag{11}$$

Physically, the barotropic waves feel the large external radius of deformation, whereas the baroclinic waves feel the short internal radius of deformation. By introducing the reduced gravity g' which is much shorter than the gravity g, we set $N = (g'/H)^{1/2}$ to get $R = (g'\,H)^{1/2}/f_0$.

Fig. 4: these radii can be computed & displayed in a map (Emery et al. 1984).

Usually, the internal deformation radius is called the Rossby deformation radius and it is far smaller than the external deformation radius which is the deformation radius of the free surface. An interpretation of the Rossby deformation radius is that when the scale of the motion is of the order of it, the potential energy E_{pot} which is available is of the same order as the kinetic energy E_{cin}, thus if the scale of motion L is bigger than R_{int}, then $E_{pot} > E_{cin}$.

EXTERNAL ROSSBY RADIUS OF DEFORMATION

INTERNAL ROSSBY RADIUS OF DEFORMATION

RADII ARE IN KILOMETERS

ANNUAL AVERAGE
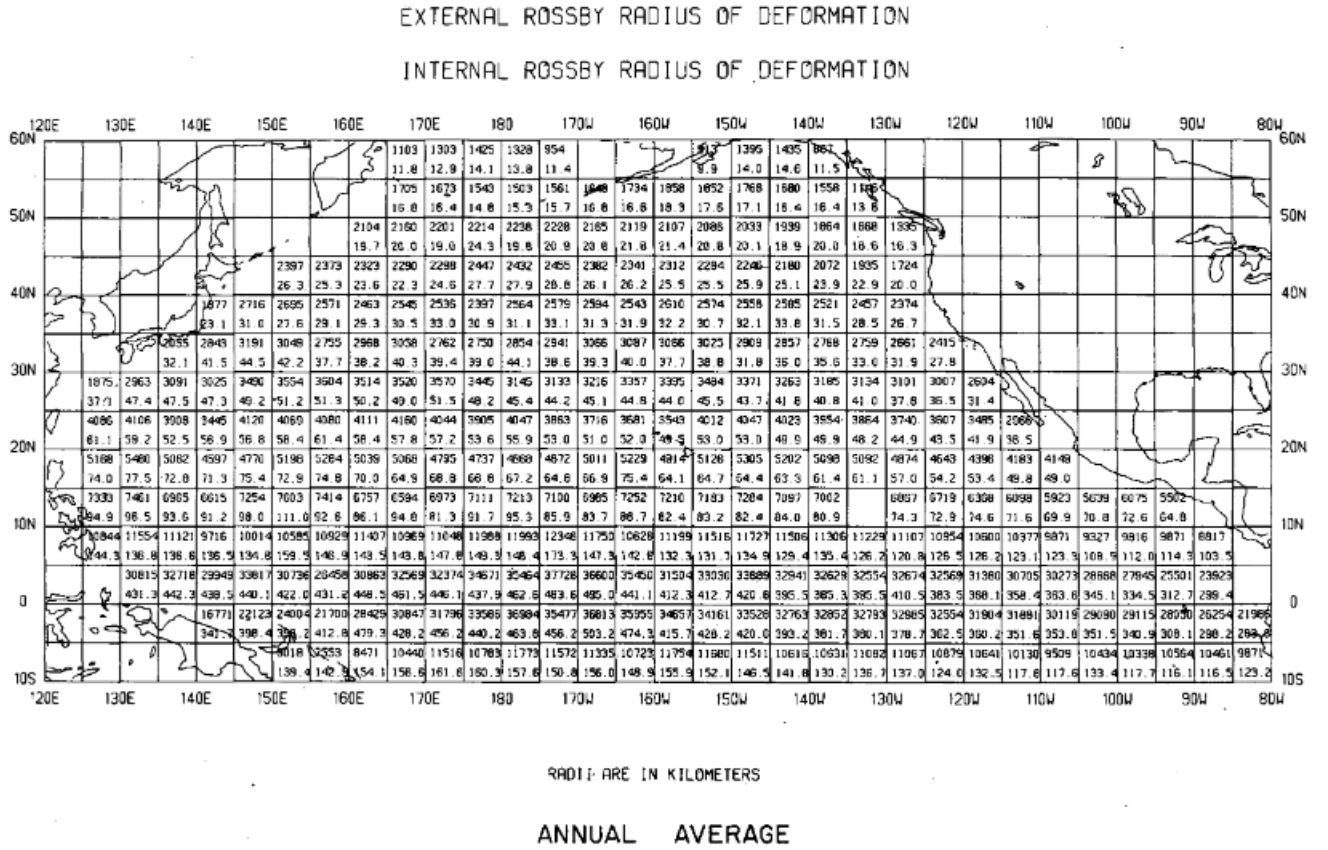
Fig. 4 – External (upper numbers) and internal (lower numbers) radii of deformation expressed in km for the North Pacific Ocean (from EMERY et al. 1984).

At the equatorial region, we can define the equatorial radius of deformation:

$$R_{eq} = \left(\frac{(g' H)^{1/2}}{\beta_0} \right)^{1/2} \tag{12}$$

where $(g' H)^{1/2} = c \sim 1,4 m/s$ typically in the tropical ocean with $H \sim 100m$, g' being here a suitable reduced gravity characterizing the stratification and H being a layer thickness. One can estimate $\beta_0 = 2\Omega/R_e \sim 2.10^{-11} m^{-1} s^{-1}$, with Ω being the Earth's angular rotation rate and R_e being the Earth's radius. Thus one can estimate $R_{eq} \sim 250km$ for the tropical ocean (CUSHMAN-ROISIN & BECKERS 2010), but if we look at Fig. 4, its value is typically higher than $400km$ at the equator line (EMERY et al. 1984).

To study planetary Rossby waves in the Pacific Ocean, far from the coasts, a multi-layer model of an ocean of uniform depth on the β-plane is usually chosen: we consider both rotation and stratification effects. We then separate

the vertical and horizontal dependences to obtain simple barotropic and baroclinic modes. Most of the energy goes into a combination of barotropic and baroclinic planetary waves, especially in the first baroclinic modes. The theoretical Rossby radius of deformation R_m and the propagation speed c_m can be estimated for a mode m at latitude ϕ and are linked by (CHELTON et al. 1998):

$$R_m \;=\; \frac{c_m}{|f_0(\phi)|} \qquad\qquad \text{if } |\phi| \geq 5° \tag{13}$$

$$R_m \;=\; \left(\frac{c_m}{\beta_0(\phi)}\right)^{1/2} \qquad\qquad \text{if } |\phi| < 5° \tag{14}$$

where $f_0 = 2\,\Omega\,\sin(\phi)$ is the Coriolis parameter and $\beta_0 = df/dy = 2\,\Omega\,R_e^{-1}\cos(\phi)$ is its latitudinal variation, with Ω being the Earth's angular rotation rate and R_e being the mean Earth radius.

2.5   Dispersion relation and phase speed

Let us assume that the time derivatives are small terms, that the rotation is important and that viscous effects are negligible: $Ro_T << 1$, $Ro << 1$, $Ek << 1$.

In the linear theory, the linearized 3D equations are cast onto an infinite and discrete set of vertical normal modes. Under the beta-plane approximation, we can obtain normal modes corresponding to planetary waves.

With variation $\sim e^{k\,x - \omega\,t}$ for wave solutions propagating in the x-direction, with a structure in y-direction, we obtain a cubic equation in ω (LEBLOND & MYSAK 1978, PEDLOSKY 1987) also referred as the parabolic cylinder equation (ALBEKIONI et al. 2023):

$$\frac{d^2 V}{dy^2} + \left(\frac{\omega^2 - \beta_0^2 y^2}{c^2} - \frac{\beta_0 k}{\omega} - k^2\right) V = 0 \tag{15}$$

where the solution $V(y)$ is given by a Hermite polynomial of degree m multiplying a decreasing exponential in $-y^2$. We obtain thus a dispersion relation for ω_m and the phase velocity of the waves is given approximately by

$$\frac{\omega_m}{k} = c_m \;\simeq\; \frac{-\beta_0\,R_{eq}^2}{2m+1} \tag{16}$$

where R_{eq} is the equatorial radius of deformation (corresponding to the first baroclinic radius of deformation) and $m \geq 1$ is a natural number (corresponding to the number of the baroclinic mode). With this relation, by calculating

β_0 at the right latitude, we can estimate theoretically the propagation speed of equatorial planetary waves and then compare it to the observations.

Let us denote the wavevector by $\vec{k} = (k_x, k_y, k_z)$ with the wavenumbers k_x, k_y and k_z.

The dispersion relation of barotropic planetary waves from beta-plane geostrophic dynamics is

$$\omega = \frac{-\beta_0\, k_x}{k_x^2 + k_y^2 + R_{ext}^{-2}} \tag{17}$$

The dispersion relation of baroclinic planetary waves from quasi-geostrophic dynamics is:

$$\omega_m = \frac{-\beta_0\, k_x}{k_x^2 + k_y^2 + R_m^{-2}} \tag{18}$$

where m is a natural number. This is the presence of stratification that permits the existence of an infinite and discrete set of planetary waves, the first being barotropic and all others being baroclinic. The barotropic and the 1st baroclinic components carry most of the energy of the planetary waves in the ocean.

From the dispersion relation, we can easily obtain the zonal phase speed:

$$c_m = \frac{\omega_m}{k_x} \tag{19}$$

and we see that the direction can, in theory, only be westward for Rossby planetary waves. Because the external radius of deformation is larger than the internal radii of deformation, barotropic waves propagate more rapidly than baroclinic waves.

3   Multi-layered model

To account of the stratification of the ocean, it is common to discretize it in the vertical, obtaining a multi-layered model. In this idealization, there is a finite number n of moving layers, each having its thickness and its uniform density (thus the density varies in steps in the vertical).

For a layer k, we define recursively the interfacial heights from the bottom of the ocean: $z_n = b$ and then for $k \in [1, n]$, $z_{k-1} = z_k + h_k$ where h_k is the thickness of the layer k.

For a layer k, we usually define the Montgomery potential by $P_1 = p_{atm} + \rho_0\, g\, z_0$ and then for $k \in [1, n-1]$, $P_{k+1} = P_k + \Delta\rho\, g\, z_k$, where z_0 corresponds to the surface level and $\Delta\rho$ is the density difference between two successive layers.

There are different types of multi-layered models: with free surface on the top or with rigid-lid on the top, or with reduced gravity.

Here we are interested in what is observed at the sea surface and we assume that the ocean is sufficiently deep, so we choose a theoretical reduced gravity model, where the *reduced gravity* is defined by $g' = g\, \Delta\rho/\rho_0$ with $\rho_0 = \rho_1$.

3.1   The 1.5-layer model

Let us first recall the reduced gravity model with 1 active layer (called 1.5-layer model). Below a certain depth, below the upper active ocean (here with only 1 active layer), the ∞ deep ocean is at rest with a constant density.

The reduced gravity is $g' = g(\rho_2 - \rho_1)/\rho_1$.

The gravest mode is the 1st baroclinic mode.

Let us write the shallow-water equations[2]

$$\partial_t u - \beta_0\, y\, v = -g'\partial_x h \tag{20}$$

$$\partial_t v + \beta_0\, y\, u = -g'\partial_y h \tag{21}$$

$$\partial_t h + H\left(\partial_x u + \partial_y v\right) = 0 \tag{22}$$

where H is the thermocline depth.

Let us assume zero meridional flow: $v = 0$ and define the speed $c = (g'\, H)^{1/2}$,

---

[2]To write the shallow water equations in atmospheric and oceanic modelling, we assume the hydrostatic approximation, the shallow-fluid approximation and the traditional approximation which neglects Coriolis terms with vertical velocity. We also assume the Boussinesq approximation which ignores all the variations of the density of the fluid in linear momentum equations, except when associated with the gravitational term.

radius $R_{eq} = (c/\beta_0)^{1/2}$ and time $T_{eq} = (\beta_0 c)^{-1/2}$. We obtain an expression for (u, h) for the equatorial Kelvin waves.

But the set of equations $\{(20),(21),(22)\}$ has additional solutions, corresponding to the Poincaré waves and the Rossby waves. By assuming oscillatory solutions for (u, v, h)

$$u = U(y) \cos(kx - \omega t)$$
$$v = V(y) \sin(kx - \omega t)$$
$$h = A(y) \cos(kx - \omega t)$$

we obtain an equation for the meridional structure $V(y)$:

$$\frac{d^2 V}{dy^2} + \left(\frac{\omega^2 - \beta_0^2 y^2}{c^2} - \frac{\beta_0 k}{\omega} - k^2 \right) V = 0 \tag{23}$$

and it has the solution $V(y) = \mathcal{H}_m \left(\frac{y}{R_{eq}} \right) exp \left(\frac{-y^2}{2 R_{eq}^2} \right)$, where $\mathcal{H}_m$ is the Hermite polynomial of degree m.

The roots exist only when they satisfy the dispersion relation:

$$\frac{\omega^2}{c^2} - k^2 - \frac{\beta_0 k}{\omega} = \frac{2m + 1}{R_{eq}^2} \tag{24}$$

There are 3 roots for each $m \geq 1$ when k varies.
2 roots correspond to Poincaré waves:

$$\omega_m \simeq \pm \left(\frac{2m + 1}{T_{eq}^2} + g' H k^2 \right)^{1/2} \tag{25}$$

and 1 root corresponds to Rossby waves:

$$\omega_m \simeq \frac{-\beta_{0,eq} k R_{eq}^2}{2m + 1} \tag{26}$$

with $\beta_{0,eq} \simeq 2.29\,10^{-11} m^{-1} s^{-1}$ and $R_{eq} \simeq 250 km$ (CUSHMAN-ROISIN & BECKERS 2010). I can estimate the theoretical propagation speeds of 1st baroclinic Rossby waves at the equator ($lat = 0°$):

$$v_1 = \omega_1/k \simeq \frac{-\beta_{0,eq} R_{eq}^2}{2 + 1} \simeq -48 cm/s$$

where there is a negative sign because the x-axis goes from west to east, but the Rossby waves propagate from east to west.

To evaluate the propagation speed outside of the equator line ($lat \neq 0°$), we need to calculate $\beta_0 = \beta_{0,eq}\, cos(lat)$ and estimate $R = \left(\dfrac{\sqrt{g'H}}{\beta_0}\right)^{1/2}$ (which takes in theory its maximum value at the equator line) by measuring the depth H in the corresponding latitude.

3.2   The 2.5-layer model

The equations governing the dynamics of a reduced gravity model with 2 active layers are the following:

$$(\partial_t + u_1\,\partial_x + v_1\,\partial_y)\, u_1 - f\, v_1 = -g'\,\partial_x(2h_1 + h_2) \tag{27}$$
$$(\partial_t + u_1\,\partial_x + v_1\,\partial_y)\, v_1 + f\, u_1 = -g'\,\partial_y(2h_1 + h_2) \tag{28}$$
$$\partial_t\, h_1 + \partial_x(h_1 u_1) + \partial_y(h_1 v_1) = 0 \tag{29}$$
$$(\partial_t + u_2\,\partial_x + v_2\,\partial_y)\, u_2 - f\, v_2 = -g'\,\partial_x(h_1 + h_2) \tag{30}$$
$$(\partial_t + u_2\,\partial_x + v_2\,\partial_y)\, v_2 + f\, u_2 = -g'\,\partial_y(h_1 + h_2) \tag{31}$$
$$\partial_t\, h_2 + \partial_x(h_2 u_2) + \partial_y(h_2 v_2) = 0 \tag{32}$$

The Fig. 5 illustrates a reduced gravity model with n active layers. Here, we assume $n = 2$. Table 1 of this figure gives the recursive relations of the Montgomery potential for reduced gravity models until just 3 active layers.
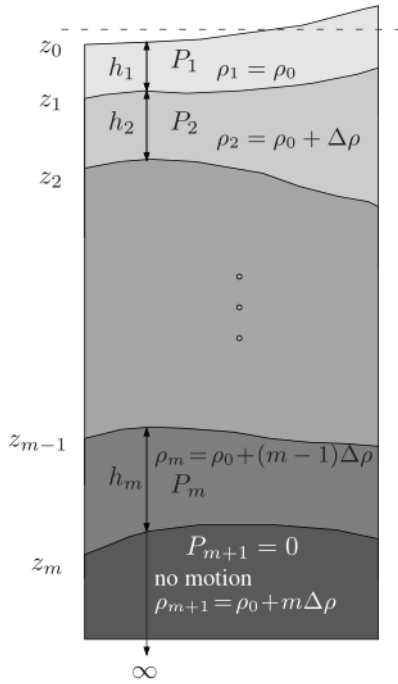
Table 1.   REDUCED GRAVITY MODELS.

One layer:
$$z_1 = -h_1 \qquad\qquad P_1 = \rho_0 g' h_1$$

Two layers:
$$z_1 = -h_1 \qquad\qquad P_1 = \rho_0 g'(2h_1 + h_2)$$
$$z_2 = -h_1 - h_2 \qquad\qquad P_2 = \rho_0 g'(h_1 + h_2)$$

Three layers:
$$z_1 = -h_1 \qquad\qquad P_1 = \rho_0 g'(3h_1 + 2h_2 + h_3$$
$$z_2 = -h_1 - h_2 \qquad\qquad P_2 = \rho_0 g'(2h_1 + 2h_2 + h_3$$
$$z_3 = -h_1 - h_2 - h_3 \quad P_3 = \rho_0 g'(h_1 + h_2 + h_3)$$

Fig. 5 – Illustration of the reduced gravity layered model (from CUSHMAN-ROISIN & BECKERS 2010).

To study the equatorial dynamics, we consider the beta-plan: $f = \beta_0 y$. We also neglect the pressure above the water. Moreover, we linearize the equations so as to neglect the advective terms and we assume that the height of the layers varies little so as to highlight H_1 in equation (29) and H_2 in equation (32).

The system of 6 equations with 6 unknowns $(u_1, v_1, h_1, u_2, v_2, h_2)$ becomes:

$$\partial_t u_1 - \beta_0 y v_1 = -g' \partial_x (2h_1 + h_2) \tag{33}$$

$$\partial_t v_1 + \beta_0 y u_1 = -g' \partial_y (2h_1 + h_2) \tag{34}$$

$$\partial_t h_1 + H_1 (\partial_x u_1 + \partial_y v_1) = 0 \tag{35}$$

$$\partial_t u_2 - \beta_0 y v_2 = -g' \partial_x (h_1 + h_2) \tag{36}$$

$$\partial_t v_2 + \beta_0 y u_2 = -g' \partial_y (h_1 + h_2) \tag{37}$$

$$\partial_t h_2 + H_2 (\partial_x u_2 + \partial_y v_2) = 0 \tag{38}$$

Let us notice that in this model, the surface elevation[3] η is smaller than the interface elevation ξ (because the density difference between the layers is smaller than the density itself), so ξ replaced η in the right-hand side of the equations of motion. And because H is constant, $\partial_t h_j \simeq \partial_t \xi_j$ for $j = 1, 2$.

3.2.1   Kelvin waves

We set the meridional flow to zero: $v_1 = 0 = v_2$, the equations (35) and (38) indicate a simple relation between u_1 & h_1 and between u_2 & h_2, and we assume solutions of the form:

$$u_1 = G_1(x + ct) g_1(y) + F_1(x - ct) f_1(y) \tag{39}$$

$$v_1 = 0 \tag{40}$$

$$h_1 = \hat{K}_1 G_1(x + ct) g_1(y) + \tilde{K}_1 F_1(x - ct) f_1(y) \tag{41}$$

$$u_2 = G_2(x + ct) g_2(y) + F_2(x - ct) f_2(y) \tag{42}$$

$$v_2 = 0 \tag{43}$$

$$h_2 = \hat{K}_2 G_2(x + ct) g_2(y) + \tilde{K}_2 F_2(x - ct) f_2(y) \tag{44}$$

By replacing the variables by these expressions in the equations (35) and (38), we find $\hat{K}_1 = \dfrac{-H_1}{c}$, $\tilde{K}_1 = \dfrac{H_1}{c}$, $\hat{K}_2 = \dfrac{-H_2}{c}$ and $\tilde{K}_2 = \dfrac{H_2}{c}$.

By replacing the variables by these expressions in the equations (33) and (36),

---

[3]The surface elevation η is usually linked to the height h and to the mean depth H by the relation $h = \eta + H$, but when there is an interface with interface elevation ξ, it is linked by $h = \eta + H + \xi$. And here, $\eta << \xi$, so $\partial_t h \simeq \partial_t \xi$.

these must be verified $\forall x, t$, so we obtain:

$$c\, G_1'\, g_1 \;=\; 2\, g'\, \frac{H_1}{c}\, G_1'\, g_1 + g'\, \frac{H_2}{c}\, G_2'\, g_2 \tag{45}$$

$$c\, F_1'\, f_1 \;=\; 2\, g'\, \frac{H_1}{c}\, F_1'\, f_1 + g'\, \frac{H_2}{c}\, F_2'\, f_2 \tag{46}$$

and

$$c\, G_2'\, g_2 \;=\; g'\, \frac{H_1}{c}\, G_1'\, g_1 + g'\, \frac{H_2}{c}\, G_2'\, g_2 \tag{47}$$

$$c\, F_2'\, f_2 \;=\; g'\, \frac{H_1}{c}\, F_1'\, f_1 + g'\, \frac{H_2}{c}\, F_2'\, f_2 \tag{48}$$

By defining $c \geq 0$, we set then $G_1'\, g_1 = 0 = G_2'\, g_2$ to rule out increasing exponential solutions and by taking $(46) - (48)$, we obtain a relation between $F_2'\, f_2$ and $F_1'\, f_1$:

$$F_2'\, f_2 = \left(-\frac{g'\, H_1}{c^2} + 1 \right) F_1'\, f_1 \tag{49}$$

By injecting it either in (33) or in (36) (same result), we obtain an equation for c^2:

$$1 \;=\; \frac{g'(2H_1 + H_2)}{c^2} - \frac{g'^2 H_1 H_2}{c^4} \tag{50}$$

$$\Longleftrightarrow \quad 0 \;=\; c^4 - c^2 (g'(2H_1 + H_2)) + g'^2 H_1 H_2 \tag{51}$$

$$\Longrightarrow \quad c_{\pm}^2 \;=\; g'\left((H_1 + H_2/2) \pm \sqrt{H_1^2 + H_2^2/4} \right) \tag{52}$$

and we note $c_+^2 = g'\, \tilde{H}_+$ and $c_-^2 = g'\, \tilde{H}_-$.

Then we continue with the equations (34) and (37) and we take $(34) - (37)$ and $(34) - 2.(37)$, which gives by injecting the result

$$F_1\, f_1(y) \;=\; 2\, F_2\, f_2(y) + \frac{g'\, H_2}{\beta_0\, c}\, \frac{1}{y}\, F_2\, f_2'(y) \tag{53}$$

from $(34) - 2.(37)$ into $(34) - (37)$:

$$0 = f_2(y) \;+\; \frac{g'}{\beta_0\, c}\, \frac{1}{y}\left(H_2 + 2\, H_1 - \frac{g'}{\beta_0\, c}\, \frac{1}{y}\, H_1 H_2\, \frac{1}{y} \right) f_2'(y) \tag{54}$$

$$+\; \left(\frac{g'}{\beta_0\, c}\, \frac{1}{y} \right)^2 H_1 H_2\, f_2''(y) \tag{55}$$

This is a 2nd order differential equation in $f_2(y)$ whose solution is:

$$f_2 \;=\; C_1\, exp\left(-y^2 / \left(\frac{2\, g'\, \tilde{H}_+}{\beta_0\, c} \right) \right) + C_2\, exp\left(-y^2 / \left(\frac{2\, g'\, \tilde{H}_-}{\beta_0\, c} \right) \right) \tag{56}$$

Indeed, we verify it for example by denoting α_1 and α_2 the exponents of the exponentials, by calculating f_2' and f_2'':

$$f_2' = -y \frac{\beta_0 c}{g'} \left(C_1 \frac{e^{\alpha_1}}{\tilde{H}_+} + C_2 \frac{e^{\alpha_2}}{\tilde{H}_-} \right)$$

$$f_2'' = \frac{-\beta_0 c}{g'} \left(C_1 e^{\alpha_1} \left(\frac{1}{\tilde{H}_+} + \frac{1}{\tilde{H}_+^2} y^2 \frac{-\beta_0 c}{g'} \right) + C_2 e^{\alpha_2} \left(\frac{1}{\tilde{H}_-} + \frac{1}{\tilde{H}_-^2} y^2 \frac{-\beta_0 c}{g'} \right) \right)$$

and then by injecting these expressions in the 2nd order differential equation, we obtain for the term in $C_1 e^{\alpha_1}$:

$$0 = \tilde{H}_+^2 - (H_2 + 2H_1)\tilde{H}_+ + H_1 H_2 \tag{57}$$

and likewise for the term in $C_2 e^{\alpha_2}$:

$$0 = \tilde{H}_-^2 - (H_2 + 2H_1)\tilde{H}_- + H_1 H_2 \tag{58}$$

that correspond well to equalities by developing (57) and (58) with $\tilde{H}_+$ and $\tilde{H}_-$. This fixes the height $\tilde{H}_\pm$ and at the same time the speed $c_\pm$.

The summary for the equatorial Kelvin waves with this model is thus:

$$u_1 = c_+ F_1(x - c_+ t)(C_1 e^{\alpha_1}) + c_- F_1(x - c_- t)(C_2 e^{\alpha_2}) \tag{59}$$
$$v_1 = 0 \tag{60}$$
$$h_1 = H_1 (F_1(x - c_+ t)(C_1 e^{\alpha_1}) + F_1(x - c_- t)(C_2 e^{\alpha_2})) \tag{61}$$
$$u_2 = c_+ F_2(x - c_+ t)(C_1 e^{\alpha_1}) + c_- F_2(x - c_- t)(C_2 e^{\alpha_2}) \tag{62}$$
$$v_2 = 0 \tag{63}$$
$$h_2 = H_2 (F_2(x - c_+ t)(C_1 e^{\alpha_1}) + F_2(x - c_- t)(C_2 e^{\alpha_2})) \tag{64}$$

and

$$c_\pm = \left(g' \left((H_1 + H_2/2) \pm \left(H_1^2 + H_2^2/4 \right)^{1/2} \right) \right)^{1/2} \tag{65}$$

gives the possible propagation speeds of these Kelvin waves. The choice of the positive root is logical because we kept only the functions $F(x - ct)$ and not the functions $G(x + ct)$.

To get a graphic idea of the speeds $c_{\pm}$, we consider the adimensional parameters:

$$\frac{H_1}{H_2} \equiv \delta \tag{66}$$

$$\frac{c_+}{\sqrt{g' H_2}} \equiv \gamma_1 = \sqrt{\delta + 1/2 + \sqrt{\delta^2 + 1/4}} \tag{67}$$

$$\frac{c_-}{\sqrt{g' H_2}} \equiv \gamma_2 = \sqrt{\delta + 1/2 - \sqrt{\delta^2 + 1/4}} \tag{68}$$

and we vary δ, by example in the interval $[0, 10]$, as graphically represented in
Fig. 6. We see there that γ_1 starts from 1 for $\delta = 0$ and increases then, while
γ_2 starts from 0 for $\delta = 0$ and increases too, but it quickly reaches a plateau
without ever reaching to 1. We get so $\gamma_1 \geq 1$ and $\gamma_2 < 1$, or $c_+ \geq \sqrt{g' H_2}$ and
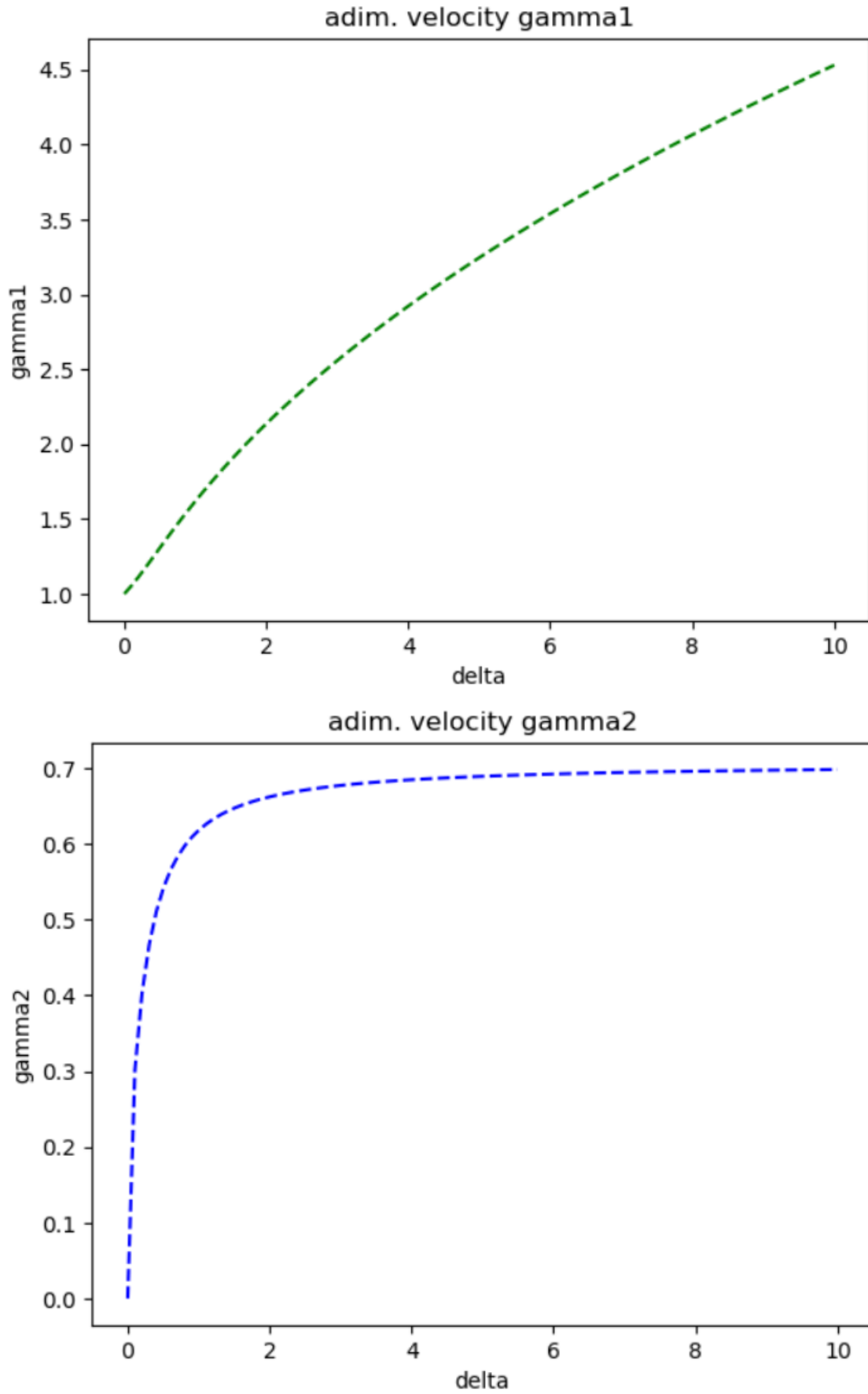$c_- < \sqrt{g' H_2}$.

Fig. 6 – Illustration of the adimensional velocities γ_1 and γ_2 for δ values in the interval $[0, 10]$.

3.2.2 Poincaré and Rossby waves

We assume oscillating solutions in cos and sin with $k_1 = k_2 \equiv k$:

$$
\begin{align}
u_1 &= U_1(y)\,\cos(k_1\,x - \omega\,t) \tag{69}\\
v_1 &= V_1(y)\,\sin(k_1\,x - \omega\,t) \tag{70}\\
h_1 &= A_1(y)\,\cos(k_1\,x - \omega\,t) \tag{71}\\
u_2 &= U_2(y)\,\cos(k_2\,x - \omega\,t) \tag{72}\\
v_2 &= V_2(y)\,\sin(k_2\,x - \omega\,t) \tag{73}\\
h_2 &= A_2(y)\,\cos(k_2\,x - \omega\,t) \tag{74}
\end{align}
$$

and we get then 6 equations for 6 variables $(U_1, V_1, A_1, U_2, V_2, A_2)$:

$$
\begin{align}
\omega\,U_1 - \beta_0\,y\,V_1 &= g'\,k\,(2\,A_1 + A_2) \tag{75}\\
\omega\,U_2 - \beta_0\,y\,V_2 &= g'\,k\,(A_1 + A_2) \tag{76}\\
-\omega\,V_1 + \beta_0\,y\,U_1 &= -g'\,(2\,A_1' + A_2') \tag{77}\\
-\omega\,V_2 + \beta_0\,y\,U_2 &= -g'\,(A_1' + A_2') \tag{78}\\
\omega\,A_1 + H_1\,(-k\,U_1 + V_1') &= 0 \tag{79}\\
\omega\,A_2 + H_2\,(-k\,U_2 + V_2') &= 0 \tag{80}
\end{align}
$$

After a few pages of calculations, we obtain expressions for the derivatives U_1', U_2', V_1' and V_2' in function of the not-derived variables:

$$
U_1' = \frac{\omega\,\beta_0\,y\,(U_1 - U_2) - \beta_0^2\,y^2\,(V_1 - V_2) - \dfrac{g'\,k}{\omega}\,(\beta_0 + \omega\,k)\,H_1\,V_1}{-g'\,k\,H_1} \tag{81}
$$

$$
U_2' = \frac{\omega\,\beta_0\,y\,(U_1 - 2\,U_2) - \beta_0^2\,y^2\,(V_1 - 2\,V_2) - \dfrac{g'\,k}{\omega}\,(\beta_0 + \omega\,k)\,(-H_2\,V_2)}{g'\,k\,H_2} \tag{82}
$$

$$
V_1' = k\,U_1 + \frac{\omega^2(U_1 - U_2) - \beta_0\,y\,(V_1 - V_2)\,\omega}{-g'\,k\,H_1} \tag{83}
$$

$$
V_2' = k\,U_2 + \frac{\omega^2(U_1 - 2\,U_2) - \beta_0\,y\,(V_1 - 2\,V_2)\,\omega}{g'\,k\,H_2} \tag{84}
$$

and we obtain thus 2 interesting cubic equations in ω for V_1'' and V_2'':

$$
V_1'' + \frac{\omega^2 - \beta_0^2\,y^2}{g'\,H_1}\,(V_1 - V_2) - k\,\frac{\beta_0 + \omega\,k}{\omega}\,V_1 = 0 \tag{85}
$$

$$
V_2'' + \frac{-\omega^2 + \beta_0^2\,y^2}{g'\,H_2}\,(V_1 - 2\,V_2) - k\,\frac{\beta_0 + \omega\,k}{\omega}\,V_2 = 0 \tag{86}
$$

By highlighting the operator $\mathcal{L}$ identical in both equations and by denoting $a(y) \equiv (\omega^2 - \beta_0^2 y^2)/g'$, we obtain the system:

$$\mathcal{L}(V_1) + \frac{a(y)}{H_1}(V_1 - V_2) = 0 \tag{87}$$

$$\mathcal{L}(V_2) + \frac{a(y)}{H_2}(2V_2 - V_1) = 0 \tag{88}$$

By setting $V_2 \equiv \lambda V_1$, we rewrite it:

$$\mathcal{L}(V_1) + a(y)\frac{1-\lambda}{H_1}V_1 = 0 \tag{89}$$

$$\mathcal{L}(V_1) + a(y)\frac{2\lambda - 1}{\lambda H_2}V_1 = 0 \tag{90}$$

For these two equalities to be true, it is necessary that the coefficients between $a(y)$ and V_1 are equal! We denote so $\delta = H_1/H_2$, we obtain the equality:

$$\lambda(1-\lambda) = \delta(2\lambda - 1) \tag{91}$$

$$\Longleftrightarrow \quad \lambda^2 + (2\delta - 1)\lambda - \delta = 0 \tag{92}$$

and we find:

$$\lambda_\pm = \frac{1}{2} - \delta \pm \sqrt{\delta^2 + \frac{1}{4}} \tag{93}$$

$$1 - \lambda_\pm = \delta + \frac{1}{2} \pm \sqrt{\delta^2 + \frac{1}{4}} \tag{94}$$

We then check that:

$$\lambda_\pm(1 - \lambda_\pm) = -2\delta^2 \pm 2\delta\sqrt{\delta^2 + 1/4} = \delta(2\lambda_\pm - 1) \tag{95}$$

We can therefore rewrite (85) and (86) in the form:

$$\mathcal{L}(V_1) + a(y)\frac{\delta + \frac{1}{2} \pm \sqrt{\delta^2 + \frac{1}{4}}}{H_1}V_1 = 0 \tag{96}$$

$$\Longleftrightarrow \quad \mathcal{L}(V_1) + \frac{\omega^2 - \beta_0^2 y^2}{g'\bar{H}_\pm}V_1 = 0 \tag{97}$$

$$\Longrightarrow \quad V_1'' + \left(\frac{\omega^2 - \beta_0^2 y^2}{g'\bar{H}_\pm} - k\frac{\beta_0 + \omega k}{\omega}\right)V_1 = 0 \tag{98}$$

with the heights $\boxed{\bar{H}_{\pm} = \dfrac{H_1 H_2}{H_1 + H_2/2 \pm \sqrt{H_1^2 + H_2^2/4}}}$.

Proceeding by analogy as in the reduced gravity model with 1 active layer, we get a solution which decreases offshore if:

$$\frac{\omega^2}{g'\,\bar{H}_+} - \frac{\beta_0}{\omega}\,k - k^2 = \frac{2m+1}{R_+^2} \tag{99}$$

and

$$\frac{\omega^2}{g'\,\bar{H}_-} - \frac{\beta_0}{\omega}\,k - k^2 = \frac{2m+1}{R_-^2} \tag{100}$$

with the internal deformation radii $R_+ = \left(\dfrac{\sqrt{g'\,\bar{H}_+}}{\beta_0}\right)^{1/2}$ and $R_- = \left(\dfrac{\sqrt{g'\,\bar{H}_-}}{\beta_0}\right)^{1/2}$.

We define likewise the two equatorial inertial times $T_+ = \dfrac{1}{\sqrt{\beta_0 \sqrt{g'\,\bar{H}_+}}}$ and

$T_- = \dfrac{1}{\sqrt{\beta_0 \sqrt{g'\,\bar{H}_-}}}$. We can rewrite the dispersion relations (99) and (100) by

defining the adimensional parameters $\tilde{k}_+ = k\,R_+$, $\tilde{\omega}_+ = \omega\,T_+$, $\tilde{k}_- = k\,R_-$ and $\tilde{\omega}_- = \omega\,T_-$ to obtain:

$$\tilde{\omega}_+^2 - \frac{\tilde{k}_+}{\tilde{\omega}_+} - \tilde{k}_+^2 \;=\; 2m+1 \tag{101}$$

and

$$\tilde{\omega}_-^2 - \frac{\tilde{k}_-}{\tilde{\omega}_-} - \tilde{k}_-^2 \;=\; 2m+1 \tag{102}$$

Finally, to find the dispersion relation of the Poincaré waves, we neglect the term in $\dfrac{\beta_0}{\omega}\,k$ in the dispersion relations (99) and (100) with $m \geq 1$:

$$\Longrightarrow \quad \frac{\omega^2}{g'\,H_+} \;\simeq\; \frac{2m+1}{R_+^2} + k^2 \tag{103}$$

$$\Longleftrightarrow \quad \omega^2 \;\simeq\; \frac{2m+1}{T_+^2} + g'\,H_+\,k^2 \tag{104}$$

which provides 2 roots and

$$\implies \quad \frac{\omega^2}{g' \, H_-} \simeq \frac{2m+1}{R_-^2} + k^2 \tag{105}$$

$$\iff \quad \omega^2 \simeq \frac{2m+1}{T_-^2} + g' \, H_- \, k^2 \tag{106}$$

which provides 2 roots too.

In short, we can write these relations in adimensional form:

$$\boxed{\tilde{\omega}_\pm^2 \simeq 2m+1 + \tilde{k}_\pm^2} \tag{107}$$

For the Rossby waves, $\dfrac{\beta_0}{\omega} \, k$ is the dominant term in the dispersion relations (99) and (100) with $m \geq 1$ and we also keep the term in k^2:

$$\implies \quad -\frac{\beta_0}{\omega} \, k \simeq \frac{2m+1}{R_+^2} + k^2 \tag{108}$$

$$\iff \quad \frac{\omega}{k} \simeq \frac{-\beta_0 \, R_+^2}{2m+1+R_+^2 \, k^2} \tag{109}$$

which provides 1 root and

$$\implies \quad -\frac{\beta_0}{\omega} \, k \simeq \frac{2m+1}{R_-^2} + k^2 \tag{110}$$

$$\iff \quad \frac{\omega}{k} \simeq \frac{-\beta_0 \, R_-^2}{2m+1+R_-^2 \, k^2} \tag{111}$$

which provides 1 root too.

In short, we can write these relations in adimensional form:

$$\boxed{\tilde{\omega}_\pm \simeq \frac{-\tilde{k}_\pm}{2m+1+\tilde{k}_\pm^2}} \tag{112}$$

We obtained well Rossby waves propagating westward as expected.

3.2.3 Yanai waves

We can also be interested in the $m = 0$ case who connects the Rossby waves to the Poincaré waves. These mixed waves between planetary and gravity waves are called Yanai waves. We assume $\omega \neq \sqrt{g' \, \bar{H}_\pm} \, k$ and

$$\left(\omega + \sqrt{g' \, \bar{H}_\pm} \, k\right) \left(\omega \, T_\pm - \frac{1}{\omega \, T_\pm} - k \, R_\pm\right) = 0 \tag{113}$$

MULTIVARIATE DETECTION AND PROPAGATION SPEED OF PLANETARY ROSSBY
WAVES FROM SATELLITE OBSERVATIONS OF THE EQUATORIAL PACIFIC OCEAN

29

is obtained by multiplying the dispersion relations (99) and (100) by $R_1 \sqrt{g' \bar{H}_\pm}$ and by highlighting, we find that 2 of these 6 terms equal zero, giving well the 4 terms.

We pass to adimensional form

$$\boxed{\tilde{\omega}_\pm^2 - \tilde{k}_\pm \tilde{\omega}_\pm - 1 = 0} \tag{114}$$

and we find so 4 roots

$$\Longleftrightarrow \quad \omega^2 - k \frac{R_\pm}{T_\pm} \omega - \frac{1}{T_\pm^2} \;=\; 0 \tag{115}$$

$$\Delta \;=\; \tilde{k}_\pm^2 + 4 \tag{116}$$

$$\Longrightarrow \quad \tilde{\omega}_\pm \;=\; \frac{\tilde{k}_\pm}{2} \pm \sqrt{\frac{\tilde{k}_\pm^2}{4} + 1} \tag{117}$$

By comparison with the literature, the dispersion relation (114) is correct but is more often noted in the form: $k = \dfrac{-\beta_0}{\omega} + \dfrac{\omega}{c}$.

Let us also remember that the case $m = -1$ corresponds to the Kelvin waves solution.

So we can represent all the obtained modes from (101) and (102) in a dispersion diagram for the equatorial waves (Fig. 9).

3.3   Density sections for the equatorial ocean

Fig. 7 (top): we see that the thermocline is deeper in the west than in the east in the equatorial Pacific Ocean. by considering a decrease of $10°C$ between the surface and the thermocline for the layer 1 and also a decrease of $10°C$ between the thermocline and the bottom of the layer 2, at $150°W$ of longitude and $0°$ of latitude, it is estimated that $H_1 \simeq 150m$ and $H_2 \simeq 250m$, so $\delta \simeq 0.6$.

Fig. 7 (bottom): we imagine in dark red a first layer and in medium red a second layer, and we see that the potential density does not exceed $1046kg/m^3$ at the bottom of the ocean. By considering an increase from $1041kg/m^3$ to $1043kg/m^3$ between the surface and the thermocline for the layer 1 and also an increase from $1043kg/m^3$ to $1045kg/m^3$ between the thermocline and the bottom of layer 2, at $150°W$ of longitude and $0°$ of latitude, it is estimated that $H_1 \simeq 200m$ and $H_2 \simeq 800m$, so $\delta \simeq 0.25$.
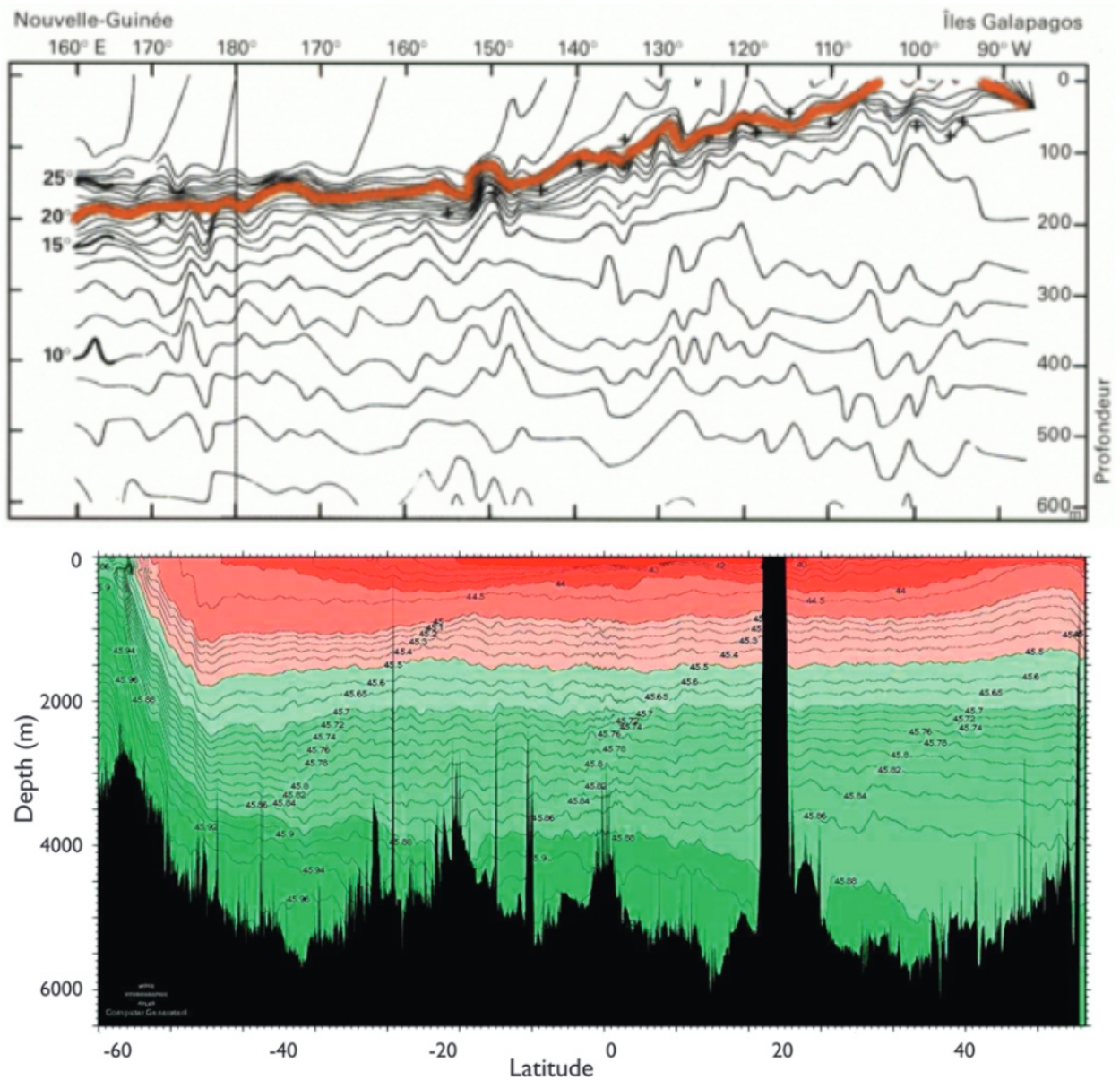
Fig. 7 – Illustration of the stratification in the equatorial Pacific Ocean. Top: section in temperature curves of the Pacific Ocean between the sea surface and $600m$ deep, realized with the oceanographic Coriolis ship in 1965 (from Merle 2006). Bottom: meridional section of potential density $(-1000kg/m^3)$ of the Pacific Ocean between the sea surface and the ocean bottom, according to the World Ocean Circulation Experiment (from Nikurashin & Vallis 2011).

Consequently, the adimensional parameter δ is small and for $\delta \sim 0.5$, we get $H_1 \sim H_2/2$ and $\dfrac{c_\pm}{\sqrt{g' H_2}} \sim \sqrt{1 \pm \sqrt{1/2}}$ and $1 - \lambda_\pm \sim 1 \pm \sqrt{1/2}$.

3.4 Limit from 2.5-layer to 1.5-layer model

To verify that our 2.5-layer model is a refinement of the more commonly used 1.5-layer model, let us consider that $H_1 = 0$.

In this case, $H_2 = H$, $\delta = 0$, $\gamma_1 = 1$, $\gamma_2 = 0$ and the 6 equations merge into 3 different equations (the shallow-water equations of the 1.5-layer model).

The propagation speeds of Kelvin waves are now $c_{\pm} = \left(g'\left(H_2/2 \pm H_2/2\right)\right)^{1/2}$ so $c_+ = \left(g'H\right)^{1/2}$ and $c_- = 0$.

The heights of Poincaré and Rossby waves are respectively now $\bar{H}_+ = 0$ and $\bar{H}_- = H_2 = H$. So we recover the radius $R_- = \left(\dfrac{(g'H)^{1/2}}{\beta_0}\right)^{1/2}$ and the time $T_- = \left(\beta_0 \left(g'H\right)^{1/2}\right)^{-1/2}$.

For $m = 1$, the propagation of 1st baroclinic Rossby waves is then given by

$$\frac{\omega}{k} = v_1 \simeq \frac{-\beta_0 \, R_-^2}{2+1}$$

The 2.5-layer model is thus compatible with the 1.5-layer model in the limit $H_1 \to 0$ and can be considered as a refinement of it. The 1st and the 2nd baroclinic modes are obtained with the 2.5-layer model, but here we focus only on 1st baroclinic modes.

By using Fig. 7 (bottom) with $H_2 = 800m$, $\rho_2 = 1045kg/m^3$, $\rho_1 = 1043kg/m^3$, our reduced gravity is $g' = 9.81\,(2/1043)m/s^2 \simeq 0.0188m/s^2$.

By recalculating the height for $R_{eq} = 250km$ and this value of g', we obtain $H = (\beta_0\,R_{eq}^2)^2/g' \simeq 109m$.

This height is probably smaller than in the reality. If we consider $H = 200m$ with the 1.5-layer model, we can estimate $R \simeq 291km$, but if we consider now $H = 800m$ with the 1.5-layer model, we can estimate $R \simeq 412km$ and if we consider $\bar{H}_- \simeq 1047m$ and $\bar{H}_+ \simeq 153m$ (values obtained for $H_1 = 200m$ and $H_2 = 800m$) with the 2.5-layer model, we estimate $R_- \simeq 440km$ and $R_+ \simeq 272km$. This value of R_- is the one that will be used to estimate the theoretical propagation speed of 1st baroclinic planetary waves.

The variation of β the latitude has a strong impact on the speed of planetary waves. C-G. ROSSBY and his collaborators found interesting to look at this variation from the pole to the equator (Fig. 8). But we are interested here with

the equatorial region, so there is a variation of β but *cos(lat)* remains close to 1 in this region.

The Rossby radius also varies with the latitude, so on the formula used to estimate the theoretical speeds, the baroclinic Rossby radius was $440km$ at the equator, $440/1.25 = 352km$ at 2.5° of latitude, $440/2 = 220km$ at 5° of latitude, and $440/2.5 = 176km$ at 10° of latitude. This variation of the Rossby radius with the latitude was deduced by respecting the proportions in the Fig. 6 in an article published in the Journal of Physical Oceanography (CHELTON et al. 1998) where the Rossby radius was a bit smaller ($100km$ at 10° of latitude and $230km$ close to 0° of latitude) to the chosen values here. The values for R_- are indicated in the third column of Table 1.

The theoretical propagation speeds are exactly the same in the southern hemisphere than in the northern hemisphere, by applying the operation: $lat \to -lat$.

VARIATION OF β WITH LATITUDE

φ	$10^{13} \cdot \beta = \dfrac{2\Omega \cos \varphi}{R} \cdot 10^{13}$
90°	0.0 cm^{-1} sec^{-1}
75°	0.593
60°	1.145
45°	1.619
30°	1.983
15°	2.212
0°	2.290

Fig. 8 – Variation of β_0 (here noted β) with the latitude φ, where Ω is the Earth's angular rotation rate and R is the mean Earth radius (from ROSSBY et al. 1939).

Table 1 – Table of the theoretical propagation speeds of 1st baroclinic planetary waves in the equatorial Pacific Ocean at different latitudes with the 2.5-layer model. The speeds are here positive by taking the norm of the velocity. The corresponding Rossby radii are indicated in the third column.

latitude [°]	theor. speed v_{th} [cm/s]	R_- [km]
10.00	23	176
7.50	29	196
5.00	37	220
3.75	58	275
2.50	94	352
1.25	122	400
0	148	440

We can thus now calculate β_0 in function of the latitude, estimate the variation of R_- and the propagation speed of 1st baroclinic planetary waves (Table 1).

3.5 Dispersion diagram for the equatorial waves

Fig. 9 presents the different modes or types of equatorial waves in a same dispersion diagram, corresponding to $\tilde{\omega}_\pm$ in function of $\tilde{k}_\pm$ (cf subsection 3.2).
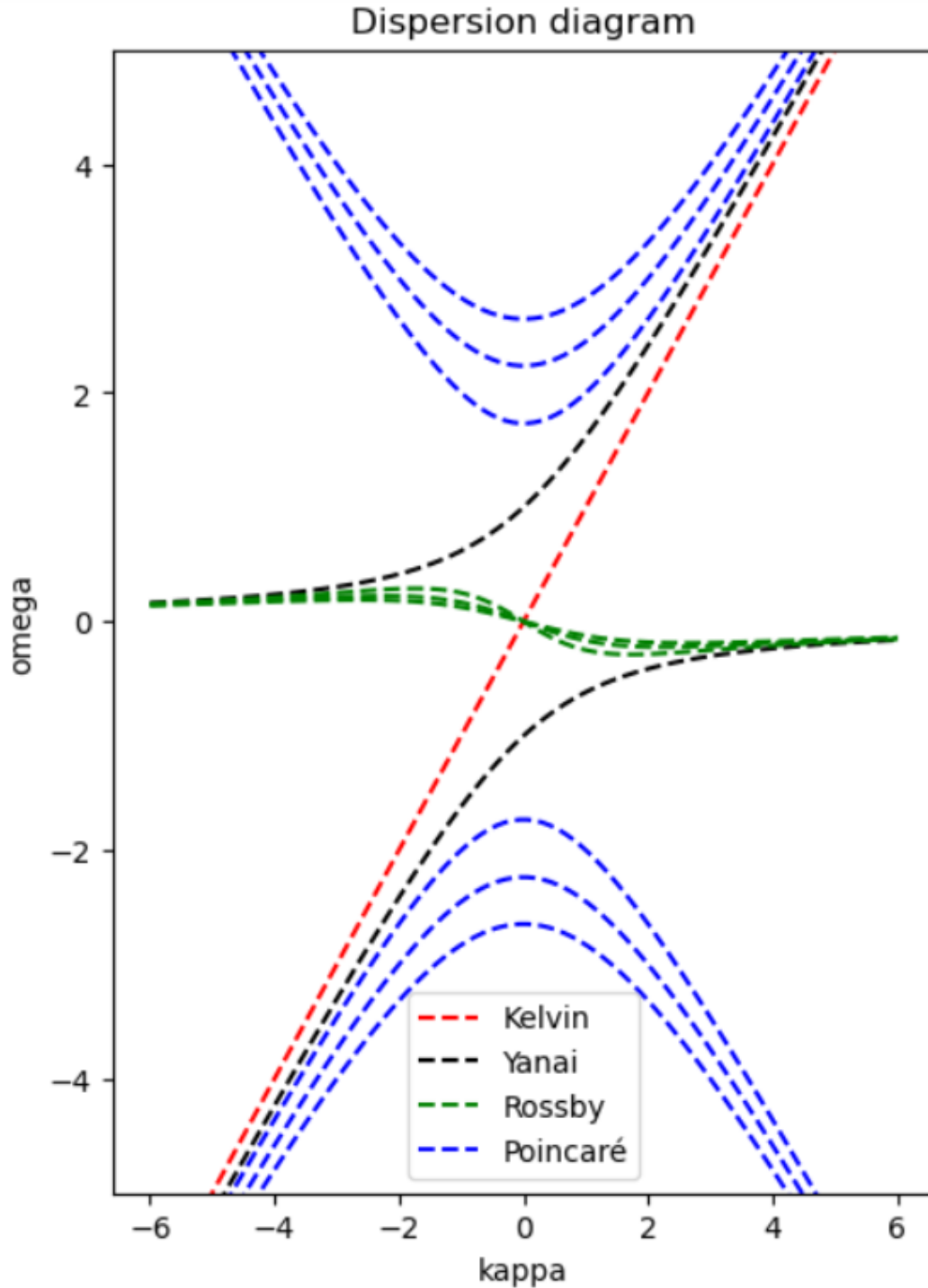

Fig. 9 – Dispersion diagram for the equatorial waves. In red: Kelvin waves ($m = -1$). In black: Yanai waves ($m = 0$). In green: Rossby waves ($m = 1, 2, 3$). In blue: Poincaré waves ($m = 1, 2, 3$).

4 Satellite observations

In this master thesis, a multivariate detection approach is chosen to study planetary waves from satellite observations of the ocean. Multivariate detection means that here we study the propagation, characteristics and front position in different variables: surface altimetry or sea surface height (SSH) and sea surface temperature (SST). Table 2 lists the two main variables and the corresponding satellites and instruments used by remote sensing scientists.

Table 2 – Characteristics in different main variables and the corresponding satellites.

variable	description	satellites and instruments
SSH	altimetry	Geosat, TOPEX/Poseidon, Jason-1, Jason-2, Jason-3
SST	temperature	ATSR on ERS-1, AVHRR on MetOp-A

In supplement, one can take an additional look at the sea surface salinity (SSS) or the ocean color variable (CHL) or at the geostrophic currents or at the wind : meridional surface wind and wind stress curl (WSC) were also studied by some scientists (White et al. 1998, Abe et al. 2014, Abe et al. 2016) in the case of oceanic planetary waves in the Pacific basin. This could be a nice complement for further research.

In this section, I review some basics about SSH and SST, show typical plots of SSH, SSHA, SST, SSTA, then I introduce the Hovmöller diagram and the Radon transform and after this, I summarize the results on the propagation speeds of 1st baroclinic planetary waves.

4.1 Sea surface height

With satellite data, the measurement of mesoscale activity over the World Ocean became possible since the launch of the Ocean Topography Experiment (TOPEX)/Poseidon and the European Remote Sensing altimetry satellites (ERS-1, ERS-2) in the 1990s and of the Geosat Follow On (GFO), Jason-1 and Envisat satellites in the 2000s (Alvera-Azcarate & Barth 2009), and then by Jason-2 and Jason-3 satellites.

The sea surface height (SSH) variable is measured by using one specific type of active microwave sensor (a radar altimeter), in the class of nadir-viewing devices. As its name suggests, it uses the radar principle to emit waves down to the sea surface and measure the time delay back up to the satellite after

echo reflection, calculating the altitude above the sea surface. This principle is illustrated in Fig. 10. This type of instrument is described in a reference book (Chap 11 in ROBINSON 2004). Such an instrument can also map the ocean surface topography, measured by altimeters and exploited by oceanographers.
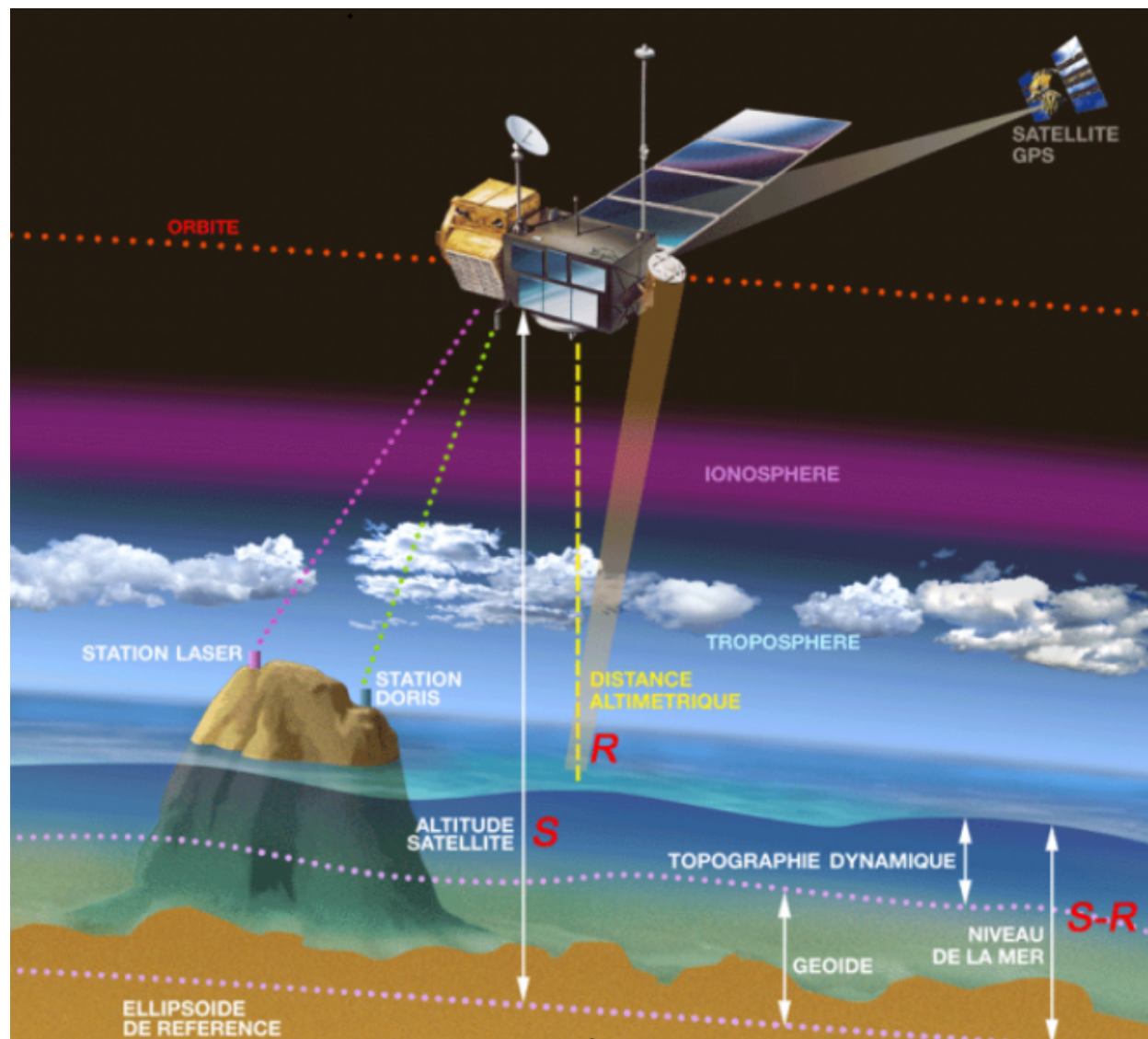

Fig. 10 – Illustration of the principle of altimetry. The ocean level (S-R) corresponds to the difference between the satellite altitude (S) in regard with the ellipsoid of reference and the sea surface altitude (R) (from CNES).

The reference level is a regular ellipsoid-shaped surface defined in a reference frame fixed in the rotating Earth, it follows approximately the Earth's shape at sea level. Different quantities are estimated: the height of the satellite H_{sat} relative to the reference level, the distance measured by the altimeter R_{alt} (actually with a precision of a few cm), the height h_{geoid} due to the distribution

of gravity over the Earth, the height h_{tide} due to the instantaneous tidal height, the height h_{atm} due to the atmospheric pressure distribution over the ocean, and finally the height $h_{dyn\,topo}$ (dynamic topography height) due to the displacement of the sea surface associated with the motion of the sea or of the ocean. These quantities are linked by a simple relation:

$$h_{dyn\,topo} = H_{sat} - R_{alt} - h_{geoid} - h_{tide} - h_{atm} \qquad (118)$$

The left-hand side is thus the displacement of the sea surface associated with the motion of the ocean and is interpreted with ocean surface currents.

To measure a distance, a satellite altimeter emits regular pulses, usually in the range $[2, 18]\,Ghz$ covering the S-, C-, X- and Ku- bands (to avoid interference with other sources) and the time delay for it to return is measured: $R_{alt} = c\,\Delta t/2 - \sum_i \Delta R_i$, where c is the signal speed, Δt is the time delay and R_i are corrections for delays in the round trip travel time of the satellite. The pulse duration is on the order of ns. Let us notice that the surface echo may be lost when the satellite moves over ice or land, so a technique called adaptive tracking is used.

To measure a correct distance, it is necessary to apply atmospheric corrections, like tropospheric correction and ionospheric correction. Moreover, there is a sea-state bias correction because the electromagnetic scattering from sea surface is not symmetrical about the mean height.It is also necessary to determine with accuracy the satellite position at the time the altimetric measurement is made, to know the value of H_{sat}. In practice, it is determined by a combination of mathematical modelling of the orbit, linked to observations by precision satellite tracking systems.

About the orbit, there is a trade-off between high orbit (much less atmospheric drag and less variability) and low orbit (less power requirements and finer spatial precision). Choosing a near-circular orbit is also useful to keep the altimeter always at the same height with the same footprint size on the ocean surface. So an orbit between $800km$ and $1300km$ altitude is usually chosen. To give an example, TOPEX/Poseidon and Jason-1 satellites had an inclination of $66°$ and a $1336km$ altitude at the equator, in a non-sun-synchronous circular orbit (ROBINSON 2004). TOPEX/Poseidon described 127 orbits during its 10-day repeat cycle, with a $315km$ cross-track separation at the equator within a cycle. Its satellite speed in orbit was $7.2km/s$, which corresponds to a ground-track speed of $5.8km/s$.

In summary, over the ocean, radar altimeters can provide 3 different types of measurements: (a) the distance between the satellite and the mean sea surface (to estimate the ocean surface topography), (b) the sea surface roughness (to estimate the local wind speed), and (c) the variability of SSH (to estimate the wave height, by the difference between troughs and ridges of the sea waves).

There is data interpolation onto a geographical grid and the spatial & temporal sampling characteristics depend on the exact orbit repeat cycle of the satellite. In this master thesis, I worked with level 4 data (the levels of processing go from L0 to L4, as illustrated in Fig. 11).

Processing level	Note
Level 0 (L0)	Unprocessed instrument data
Level 1 (L1)	Data processed to sensor unit
Level 2 (L2)	Derived geophysical variables
Level 3 (L3)	Georeferenced data
Level 4 (L4)	Data have had the greatest amount of processing applied, possibly including modelled output and measurements from several satellites and several days. All input data are validated.

Fig. 11 – The five main different processing levels in satellite data (from Marine Copernicus).

I downloaded data sets from CMEMS (Marine Copernicus) website, two by year during the period January 1993 - May 2022. Why two? This is because the data is stored from $-180°$ of longitude ($180°W$) to $180°$ of longitude ($180°E$), but the equatorial Pacific Ocean extends from $150°E$ to $80°W$, so I needed to download separately the data sets from $150°E$ to $180°E$ and the data sets from $180°W$ to $80°W$. I also restricted my data sets in the latitudinal range from $10°N$ to $10°S$ covering the equatorial band.

Because the period is long (30 years) and the lifetime of the satellites is shorter, the data comes from different satellite missions. Historically, the first altimeter to demonstrate that altimetric measurements from space can provide unique oceanographic information to the oceanographic community was with the altimeter of the Seasat mission. Then, it was the time for the Geosat altimeter

(based on the Seasat instrument). The Geosat Exact Repeat Mission (ERM) produced a global SSH dataset spanning 3 years. This data was used to obtain a better view of the horizontal nature of planetary waves and it was possible to estimate the barotropic mode from SSH data in addition to the first baroclinic mode (Jacobs 1993). But the low satellite altitude (with high atmospheric drag) made it difficult to estimate the orbit height and so the accuracy was not sufficiently good.

Later, surface altimetry data for 1993-2013 with TOPEX/Poseidon, Jason-1 and Jason-2 was used to study the spectral characteristics of planetary waves in the Northwestern Pacific Ocean (Belonenko 2016). Then Jason-2 was data was combined with the data obtained with Jason-3 launched in 2016.

The downloaded data is daily, that means that there is one available image by day. But I am interested in the slow propagating planetary Rossby waves, so I need to filter it. To filter the more rapidly propagating waves, I did an average over one month. This changes the temporal resolution from 1 day to one month. The monthly SSH means were taken as moving averages: for example for the mean centered on the 1st of January, I averaged data from 16th of December to 15th of January. Then to obtain SSH anomalies (SSHA), I calculated the climatology during the period 1993-2022 (1 for each month, so 12 in total): one for each 1st of January, one for each 1st of February, and so on, then I subtracted the climatology to the monthly SSH means, to obtain SSHA.

Because the large amount of data, I stored the original downloaded data on an external hard drive. After each of these 2 operations, I saved my monthly mean SSH data and SSHA data on a file *.nc* and I stored it on a dedicated computer folder. Then I used the Pyplot package to visualize the images with julia code on jupyter notebooks (15 different jupyter notebooks were used in total for the operations described in this section about satellite observations).

Let us now look at different maps of the equatorial Pacific Ocean obtained from the SSH data sets. Fig. 12 shows two examples of loaded mean SSH in equatorial Pacific Ocean in 1994. We see that the SSH varies by $\pm 0.25m$. Sometimes, there are variations larger than $\pm 0.3m$, but to keep the same color variations, I used the same color range $\pm 0.22m$ in the figures.

Fig. 13 shows two examples of climatology maps, for March and September. We see a band of higher SSH in September that is usually not present in March.
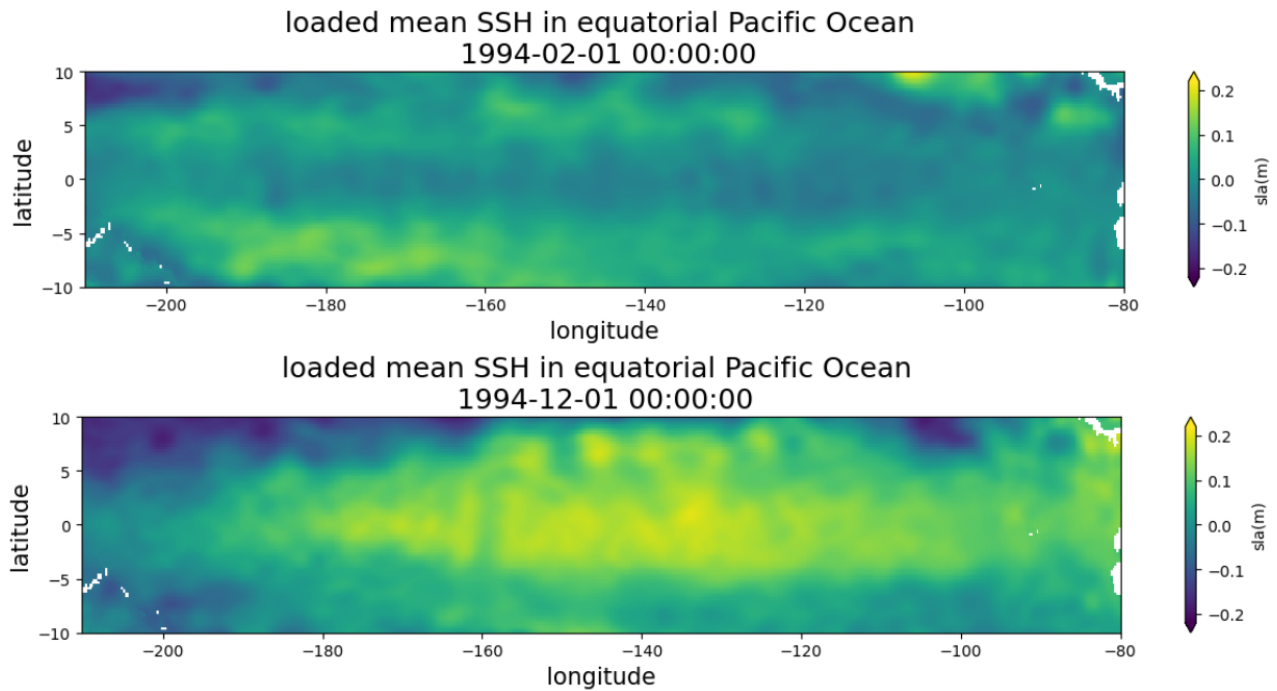
Fig. 12 – Maps of mean SSH in the equatorial Pacific Ocean. Top: mean around the 1st February 1994.
Bottom: mean around the 1st December 1994. As an illustration of the variations during the months, at the
equator, on the bottom image, the sea level altimetry (sla) is higher than on the top image.
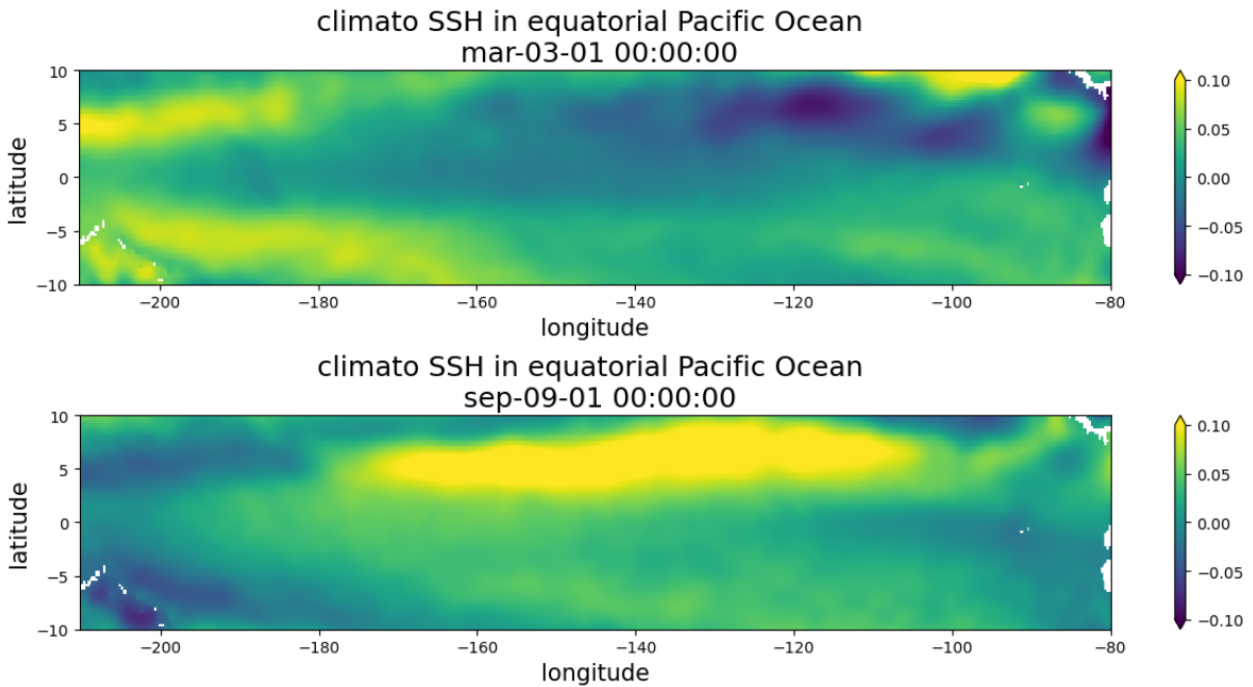

Fig. 13 – Maps of climatology for SSH in the equatorial Pacific Ocean. Top: climatology mean for each 1st
March. Bottom: climatology mean for each 1st September. As an illustration of the variations during the
months, at the equator, on the bottom image, there is a large band (in yellow) around 5°N of latitude with
higher SSH that is not present on the top image.

Three examples of SSHA maps are shown in Fig. 14. In the top, we see very low value of SSHA at the equator, in the middle it is a bit above $0.0m$ and in the bottom, we see very high value of SSHA at the equator. These large variations are mainly due to the El Niño/La Niña events in comparison with normal conditions (Fig. 14, middle). This will be discussed in section 5.
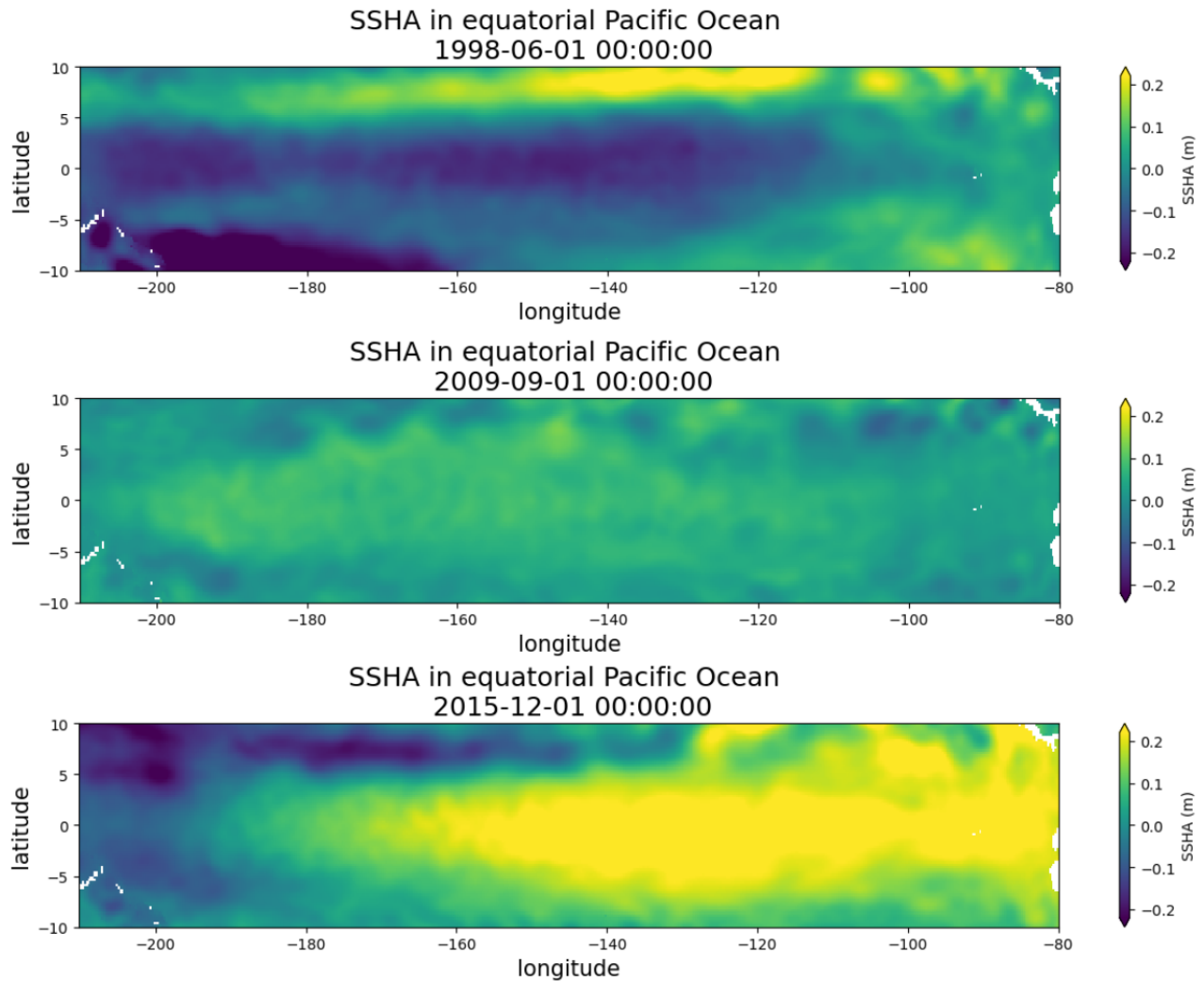

Fig. 14 – Maps of SSHA in the equatorial Pacific Ocean. Top: SSHA for 1st of June 1998. Middle: SSHA for 1st of September 2009. Bottom: SSHA for 1st of December 2015. In the top we see the La Niña event just after the large El Niño event beginning in 1997, normal conditions in the middle, and the El Niño event in 2015-2016 in the bottom.

The next step in data analysis is to plot the space-time Hovmöller diagram (subsection 4.3), but before, let us present another variable: the sea surface temperature.

4.2 Sea surface temperature

4.2.1 Radiometers

The sea surface temperature (SST) variable is measured using specific types of passive sensors (radiometers), in thermal-IR or in microwave. There are mainly two types of radiometers used to measure SST: IR and microwave radiometers. All surfaces emit radiation, but the strength depends on the surface temperature. By measuring the radiance, an IR radiometer detects the brightness temperature of the radiation. There are 2 spectral IR windows: between $3.5 - 4.1 \mu m$ and between $10.0 - 12.5 \mu m$. But none of the 2 bands is completely transparent, because the constituents of the atmosphere (mainly H_2O, O_3, CO_2) can absorb radiation emitted by the sea before reaching the detector in space and it also emits radiation. The apparent brightness measured by IR sensors is thus lower than its true temperature. To reduce the noise, the detectors are usually cooled at $T < 100K$ (lower than the typical ambient temperature of the satellite).
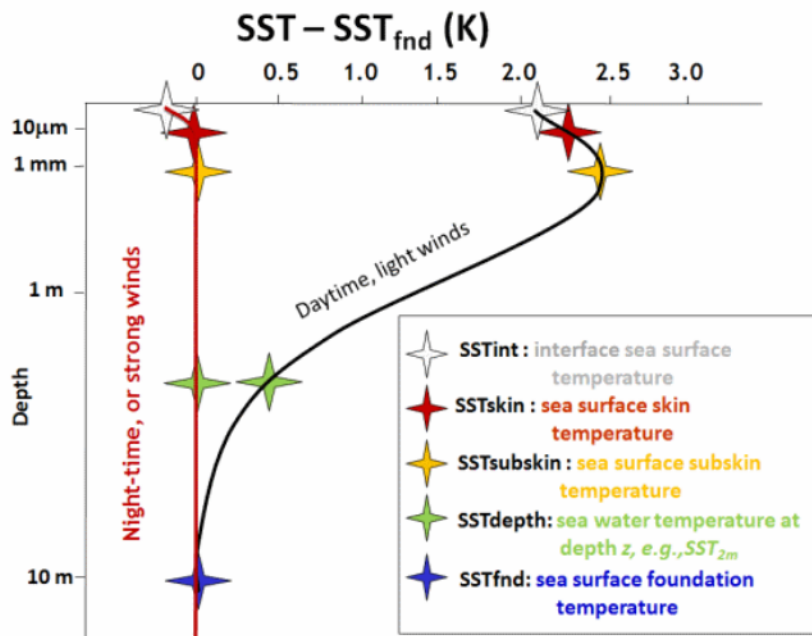

Fig. 15 – SST temperature in function of depth, as definitions proposed by the Group for High Resolution SST (from Eumetrain).

The satellites observe the SST at a location closer to the sea surface that usually measured by in-situ oceanographic instruments like buoys. The IR radiometers measure the skin SST. There is a small but not negligible difference between the skin SST and the bulk SST measurements. At a bit greater depth (below the thermal skin layer, depth $\sim 1mm$), there is what we call the sub-skin SST,

at greater depth (depth $\sim 1m$), there is what we call the depth SST, and at more greater depth (below the diurnal warming layer), there is what we call the foundation SST. The microwave radiometers measure the sub-skin SST, which is a bit higher to the skin SST[4]. The diurnal thermocline disappears at night, quite rapidly after sunset. The foundation SST is not affected by diurnal fluctuations. These different SST in function of depth are indicated in Fig. 15.

So spatial SST data measured by IR sensors can reveal oceanic phenomena altering the skin SST, occurring on a longer length scale than the spatial resolution of the sensor. Phenomena like upwelling or vertical mixing can influence the SST, bringing cooler water near the surface.

For microwave radiometers, which have a lower spatial resolution than with IR radiometers, liquid water in the form of precipitations can be a problem. There are 1 big spectral microwave window: in the $6-11\,Ghz$ frequency range. Moreover, in microwave radiometry, the apparent emissivity (typically $\epsilon < 0.5$) is lower than in IR radiometry. The IR measurement of SST and microwave radiometry are described in a reference book (Chap 7 & 8 in ROBINSON 2004).

4.2.2 Maps of SST anomalies

As for SSH, I downloaded data sets from CMEMS website, two by year during the period January 1993 - May 2022. The longitude range was $[150°E, 80°W]$ and the latitude range was $[10°S, 10°N]$, covering the equatorial band.

The data also comes from different satellite missions and the downloaded data is daily. I filtered it like for the SSH data by doing an average over one month, and then by calculating and subtracting it the climatology to obtain SST anomalies (SSTA).

The SSTA needed more memory than SSHA because the spatial resolution in the grid was different: $0.05°$ for SSTA instead of $0.25°$ for SSHA. I had 521 different values of longitude and 80 different values of latitude with SSH data, but now there are 2601 different values of longitude and 402 different values of latitude with SST data. About the temporal amount of data, there were 353 different dates, one for each month between January 1993 and May 2022. Another difference between SSH and SST data is that for SSH, the daily hour is 12 a.m. (midnight) and it is 12 p.m. (noon) for SST.

---

[4]The skin SST, affected by solar heating, corresponds to the thin surface layer where the molecular diffusion and heat conductivity processes dominate, the sub-skin SST, affected by turbulent mixing, corresponds to the base of the skin layer.
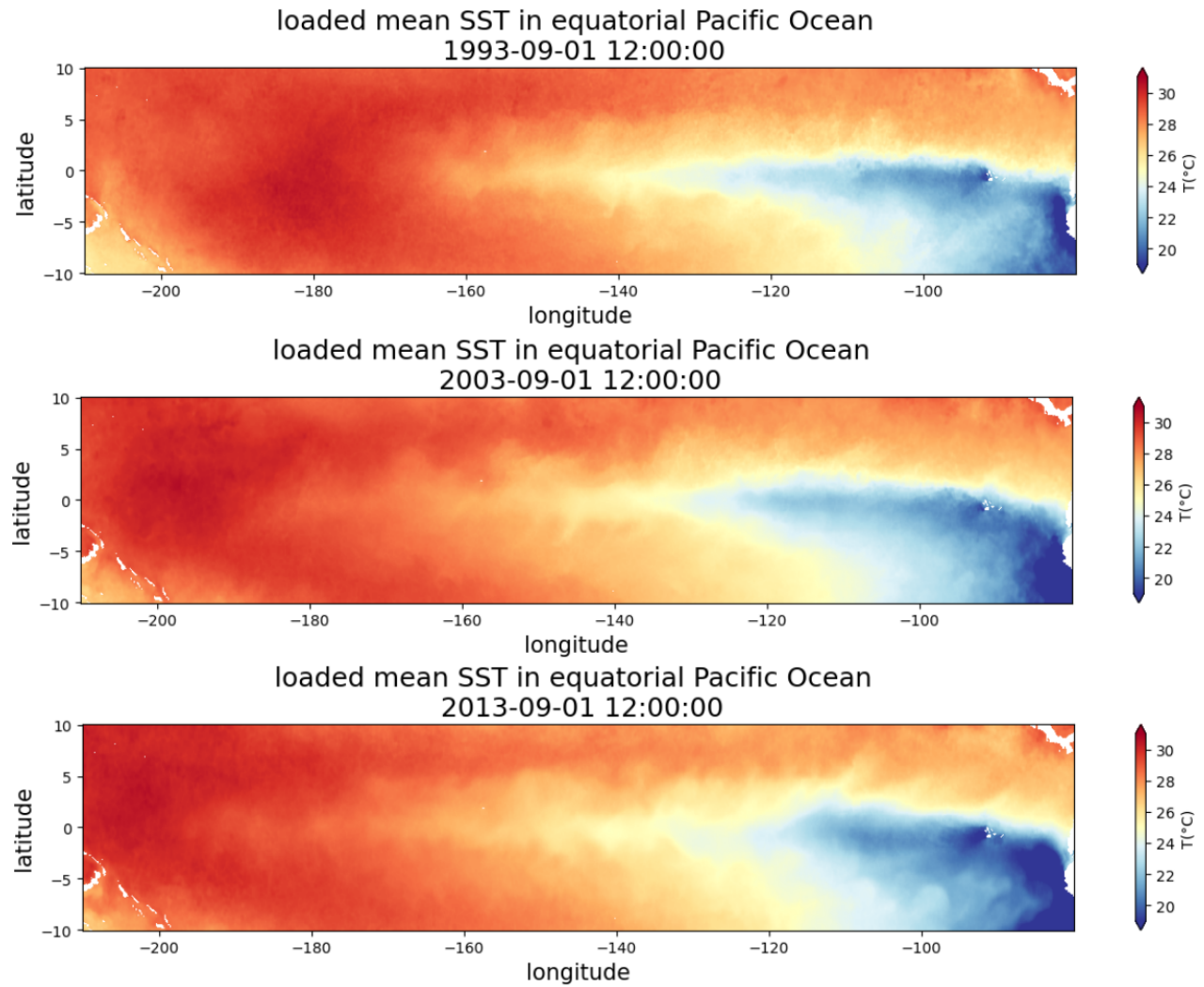
Fig. 16 – Map of mean SST (monthly average) in equatorial Pacific Ocean. Top: on 1st September 1993. Middle: on 1st September 2003. Bottom: on 1st September 2013. Because there are large seasonal variations, we still have to subtract the climatology to obtain useful SSTA data.
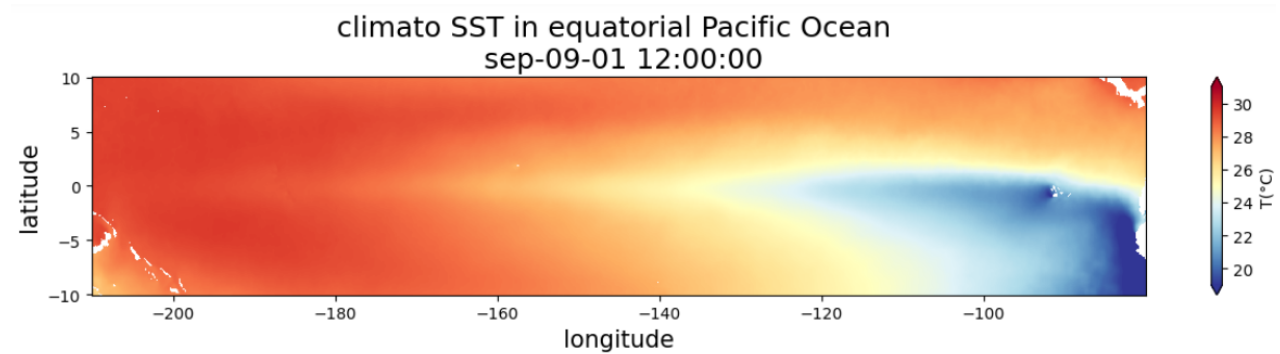

Fig. 17 – Map of climatology for SST in equatorial Pacific Ocean. Climatology mean for each of 1st September in the period 1993-2022. Because over the average over many years, the mesoscale structures are no more visible in the climatology map and become here smooth variations.

Let us now look at different maps of the equatorial Pacific Ocean obtained from the SST data sets. Fig. 16 shows mean SST maps obtained in September in different years. Fig. 17 shows the climatology map for SST in September month. We can then plot maps of SSTA, like in Fig. 18 by subtracting the climatology from the mean SST. In these 3 last figures, we see that the variation due to strong climatic events dominates on the seasonal variation at the equatorial region. I decided to use the same color variation for these 3 images to see well the SSTA variation.
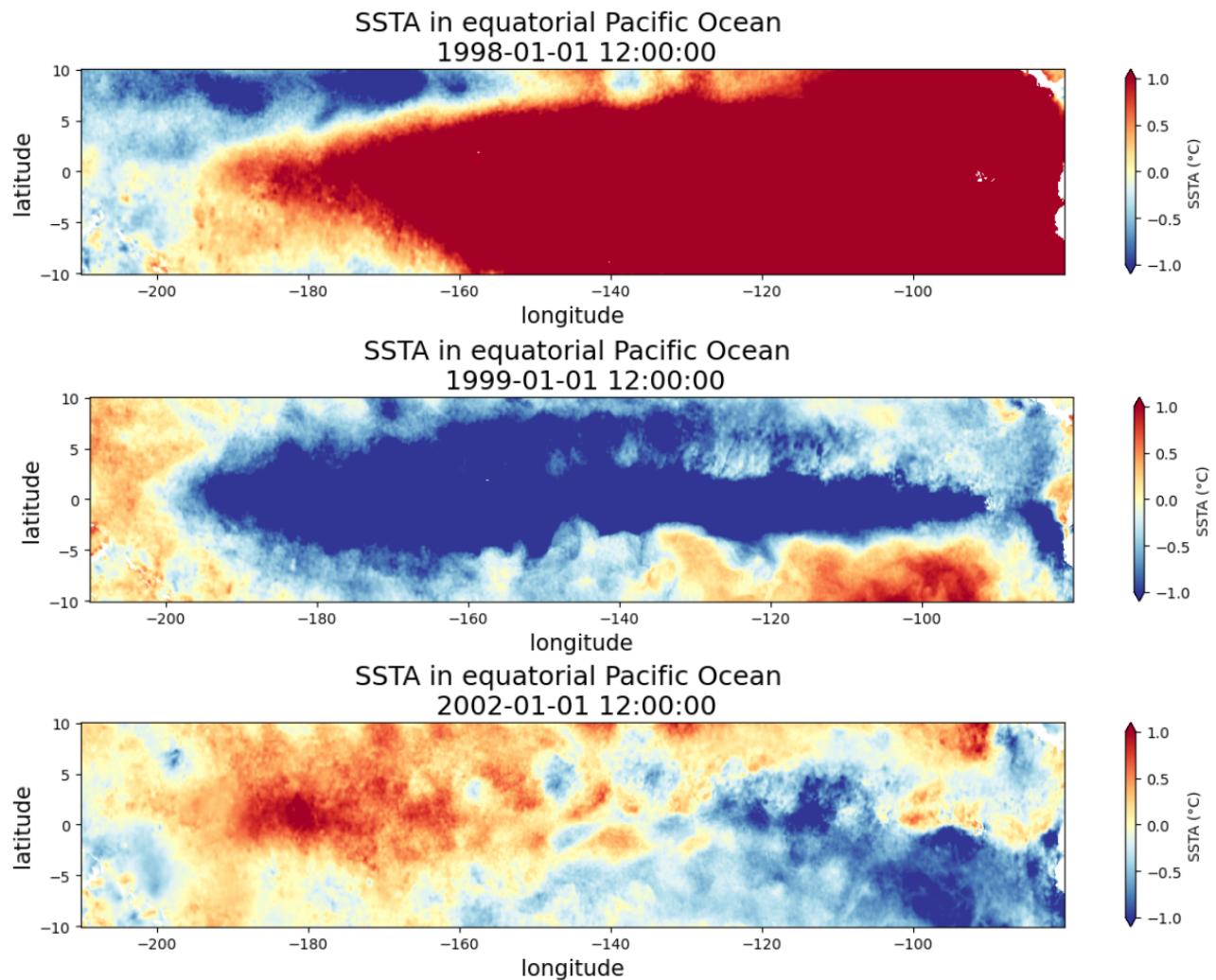

Fig. 18 – Maps of SSTA in equatorial Pacific Ocean. Top: in January 1998 during El Niño event. Middle: in January 1999 during La Niña event. Bottom: in January 2002 during normal conditions.

The next subsection illustrates the DINEOF reconstruction to obtain the empirical orthogonal functions (EOF) modes and try to visualize better the planetary Rossby wave signatures on the SST maps.

MULTIVARIATE DETECTION AND PROPAGATION SPEED OF PLANETARY ROSSBY
WAVES FROM SATELLITE OBSERVATIONS OF THE EQUATORIAL PACIFIC OCEAN

45

4.2.3 EOF from DINEOF reconstruction

I also did a DINEOF reconstruction (over the 20 first years of data) to obtain
the main EOF modes for my SST data. The EOF calculation and DINEOF
reconstruction are explained in different articles (BECKERS & RIXEN 2003,
ALVERA-AZCARATE et al. 2005, ALVERA-AZCARATE et al. 2007, BECKERS
et al. 2014). In fact, I did not distinguish well the planetary waves with the
SSTA, so I tried by subtracting also EOF modes 1, 3 and 6 instead of the clima-
tology, or both. Some EOF modes are shown in Fig. 19. The main variability
is explained by the 3 first modes (**81.26%** with EOF 1, **10.13%** with EOF 2,
4.45% with EOF 3), but the mode 6 (**0.40%** of variability) was also interesting
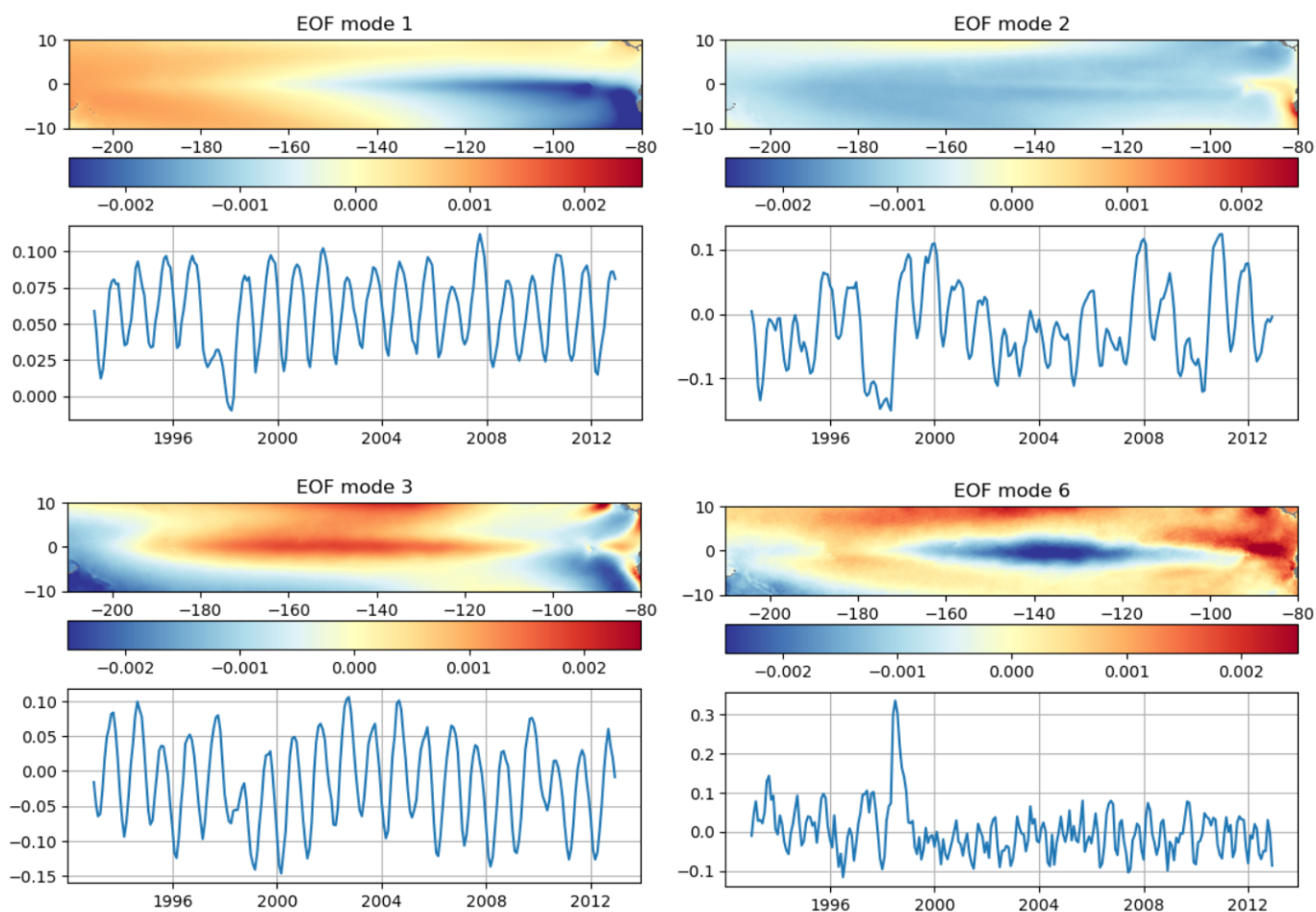for the climatic events occurring between 1997 and 1999.

Fig. 19 – EOF modes 1, 2, 3 and 6 and their variability over the years, from DINEOF reconstruction on the
period 1993-2012.

The comparison between initial data and reconstructed data is shown in Fig. 20, where we see a small difference because there are quasi no missing data in the L4 data sets (there are of course some land near the eastern and western coasts and with some islands, but these were masked before DINEOF reconstruction).
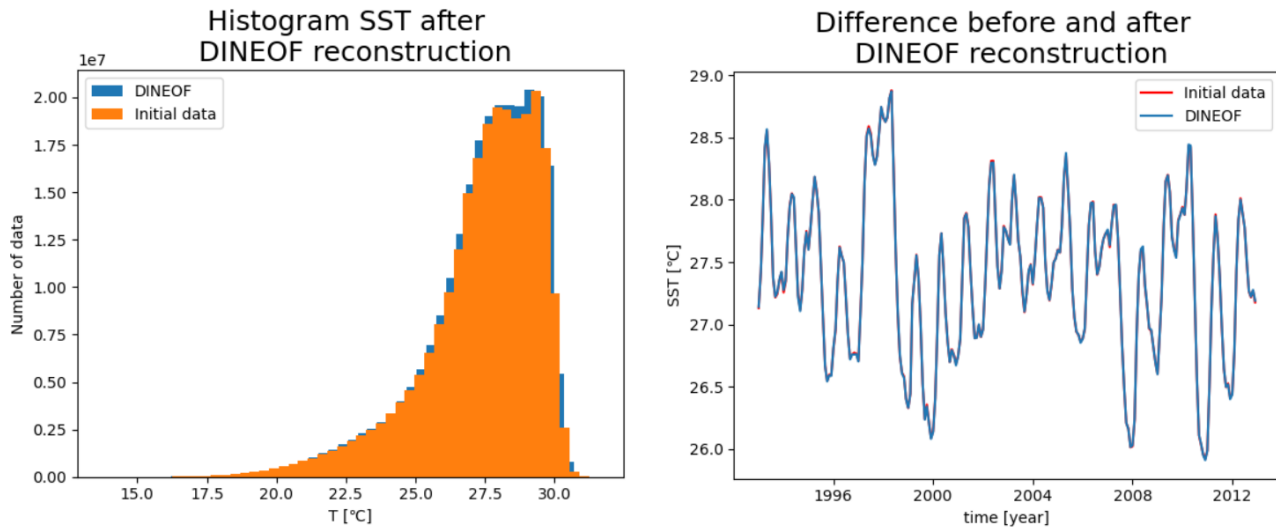

Fig. 20 – Histogram comparing the SST data before and after the DINEOF reconstruction on the period 1993-2012. Left: initial monthly mean SST data (orange) and reconstructed data (blue). Right: Difference between the two by plotting the SST in function of time. This difference is really small because I used L4 data.

EOF were used in different scientific domains, and the principal component analysis (PCA) commonly used in mathematical statistics is similar to EOF in matrix versions on discrete datasets (BECKERS & RIXEN 2003). There are other tools (like DINCAE which is a convolutional neural network) than DINEOF for removing missing data in geophysical data sets also developed and used at the GeoHydrodynamics and Environment Research (GHER) group at ULiège. Here the aim by using DINEOF was simply to obtain the EOF modes, so I do not describe here this technique into details.

The next step is to plot space-time Hovmöller diagrams for the chosen period of time and this will be the subject of next subsection.

4.3   Hovmöller diagram

To observe the propagation of oceanic planetary waves, it is necessary to look at
their signatures in a variable (like SSH, SST, SSS, or CHL) on successive dates
in a same region of the ocean. To do this, I used the anomalies of a variable
(in particular SSHA and SSTA) and then I plotted what are called, since the
work of Ernest HOVMÖLLER (HOVMÖLLER 1949) with the trough-and-ridge
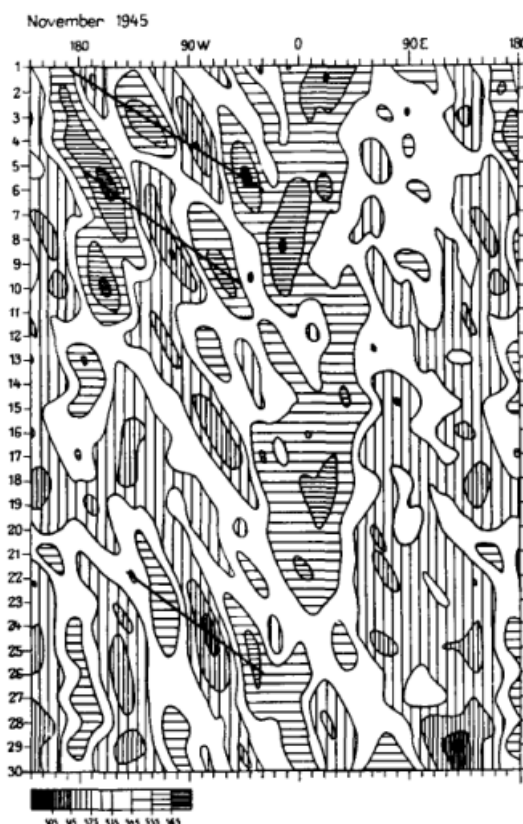diagrams (as Fig. 21) in an atmospheric context, *Hovmöller diagrams.*

Fig. 21 – Historical Hovmöller diagram: geopotential as function of longitude and time, during the month
of November 1945 and from average values of geopotentials at latitudes 35°N, 40°N, 45°N, 50°N, 55°N, 60°N.
Areas of low geopotential values (shown by vertical hatching) are troughs and areas of high geopotential
values (shown by horizontal hatching) are ridges. The straight lines indicate a succession of troughs and
ridges, revealing the propagation of waves (from HOVMÖLLER 1949).

These space-time diagrams have a space dimension on the x-axis (the longi-
tude), a time dimension on the y-axis (the time) and a variable dimension is
expressed with a color (the variable anomaly). An Hovmöller diagram corre-
sponds to a slice at constant latitude, and the propagation speed of planetary
waves is westward, but this speed is expected to vary with varying latitude.
Thus I selected constant values of latitude in my region of interest which is the

equatorial Pacific Ocean (around 10°N, 5°N, 2.5°N, 0°N, 2.5°S, 5°S, 10°S) and from several years of SSH or SST satellite data, I plotted the corresponding Hovmöller diagrams.

By considering the time series of anomaly data as a 3D cube of data, with the time as vertical dimension, an Hovmöller diagram is obtained by cutting a vertical slice through the cube, along a particular line of latitude. This is illustrated in Fig. 22.
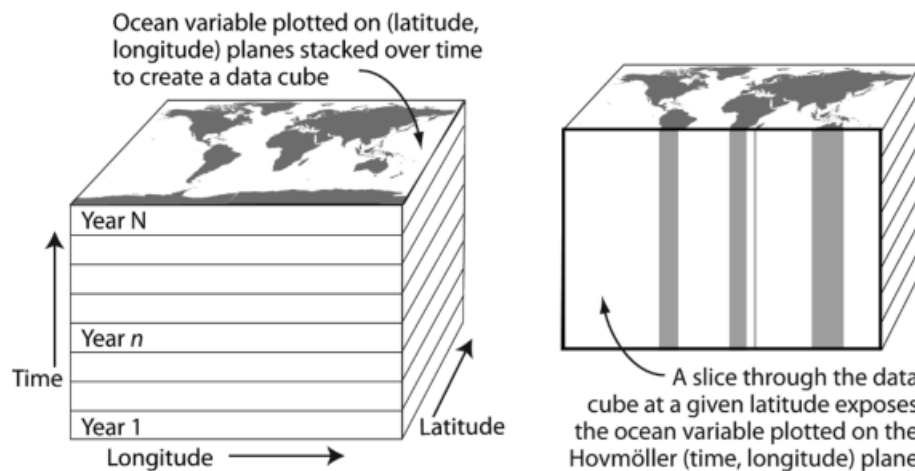
Fig. 22 – Left: schematic of the longitude-latitude-time data cube from maps of satellite data time series. Right: a vertical cut through the cube at a chosen latitude shows a map of how the selected ocean variable varies with longitude and time at the chosen latitude (from ROBINSON 2010).

When the signature of planetary waves is observed on an Hovmöller diagram, it is possible to estimate the phase speed of the waves by calculating the slope (or the angle with the horizontal or with the vertical) of the straight lines, as illustrated in Fig. 23.

Fig. 23 – Illustration of a planetary wave signature on a Hovmöller diagram (from ROBINSON 2010).

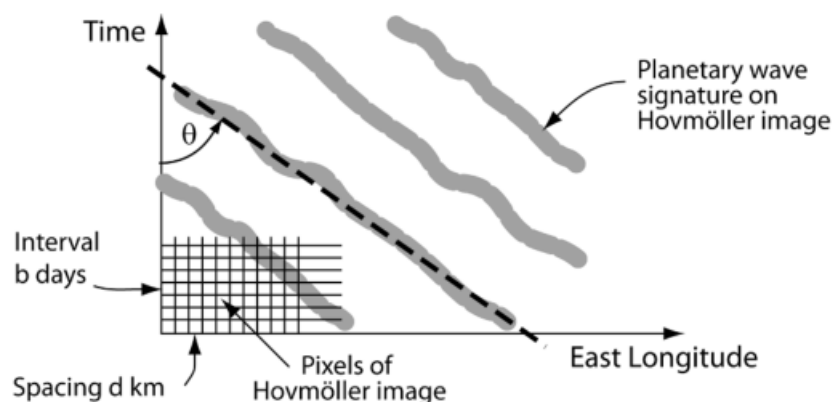Let us now notice that some data are missing values (where it is the continent or an island and not the ocean) and the location of these missing data on the L4 maps varies with the latitude. These missing values will be visible as vertical white lines in the Hovmöller diagrams. For the next step (see next subsection), the Radon transform cannot be calculated over missing data. This is why I use L4 data, and it is also why I need to cut regions of a certain longitude (a continental coast or the Galápagos islands appearing as vertical white lines) in the Hovmöller diagram before applying the Radon transform.

In Fig. 24, Hovmöller diagrams for SSHA and for SSTA were plotted, covering the period between 1993 and 2022, at the constant latitude of $0.125°N$ (because the spatial resolution of my SSH data was $0.25°$ and also because the data points were spaced in a grid passing at $\pm0.125°$ of latitude, the exact values of $10°N$, $0°N$ or $5°S$ were not available).
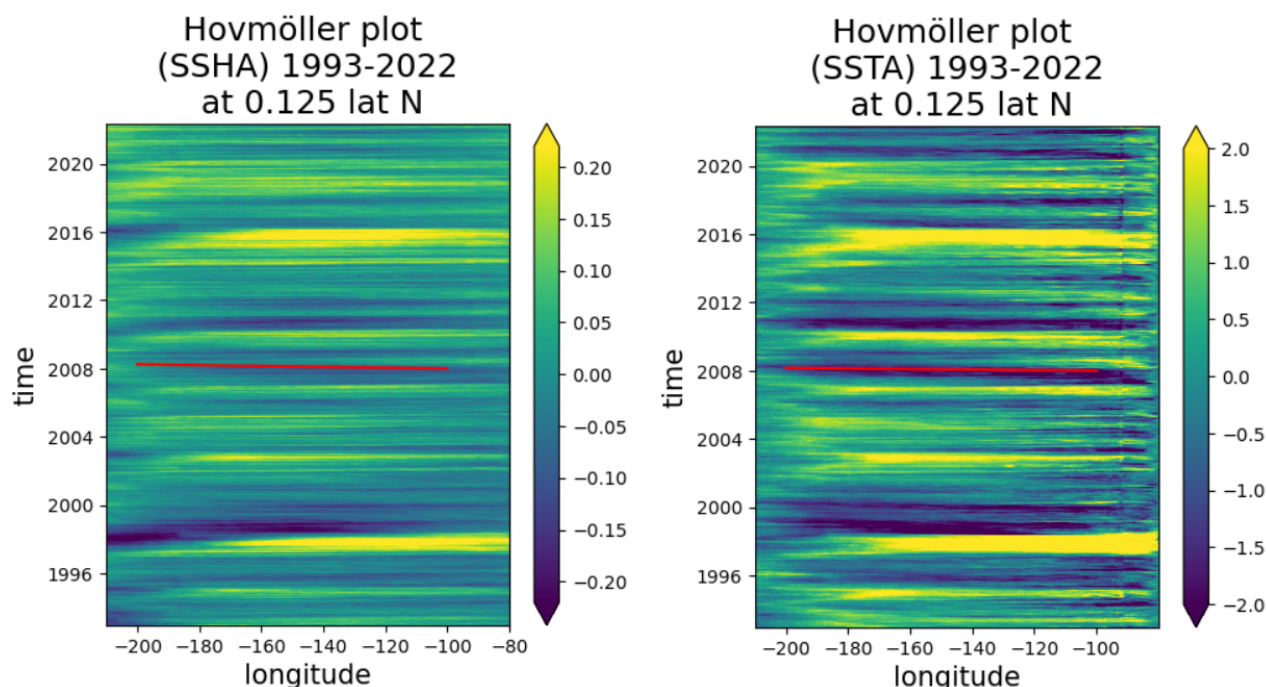
Fig. 24 – Hovmöller diagrams covering 30 years of data between 1993 and 2022 at $0°N$ of latitude. Left: for SSHA data. Right: for SSTA data. The red line indicates the expected theoretical propagation speed $v_1 \simeq 1.48 m/s$, so it needs only 3 months for the planetary waves to travel from $-100°$ to $-200°$ of longitude. The SSHA is here expressed in m, so its variation is about $\pm20cm$ and the SSTA is here expressed in $°C$, so its variation is about $\pm2.0°C$.

In Fig. 25, Hovmöller diagrams were plotted for SST data with subtraction of the climatology and/or EOF modes, between 1993-2012, at $9.975°N$ of latitude. We see that by subtracting the EOF 1 a periodic pattern reappears on the west,
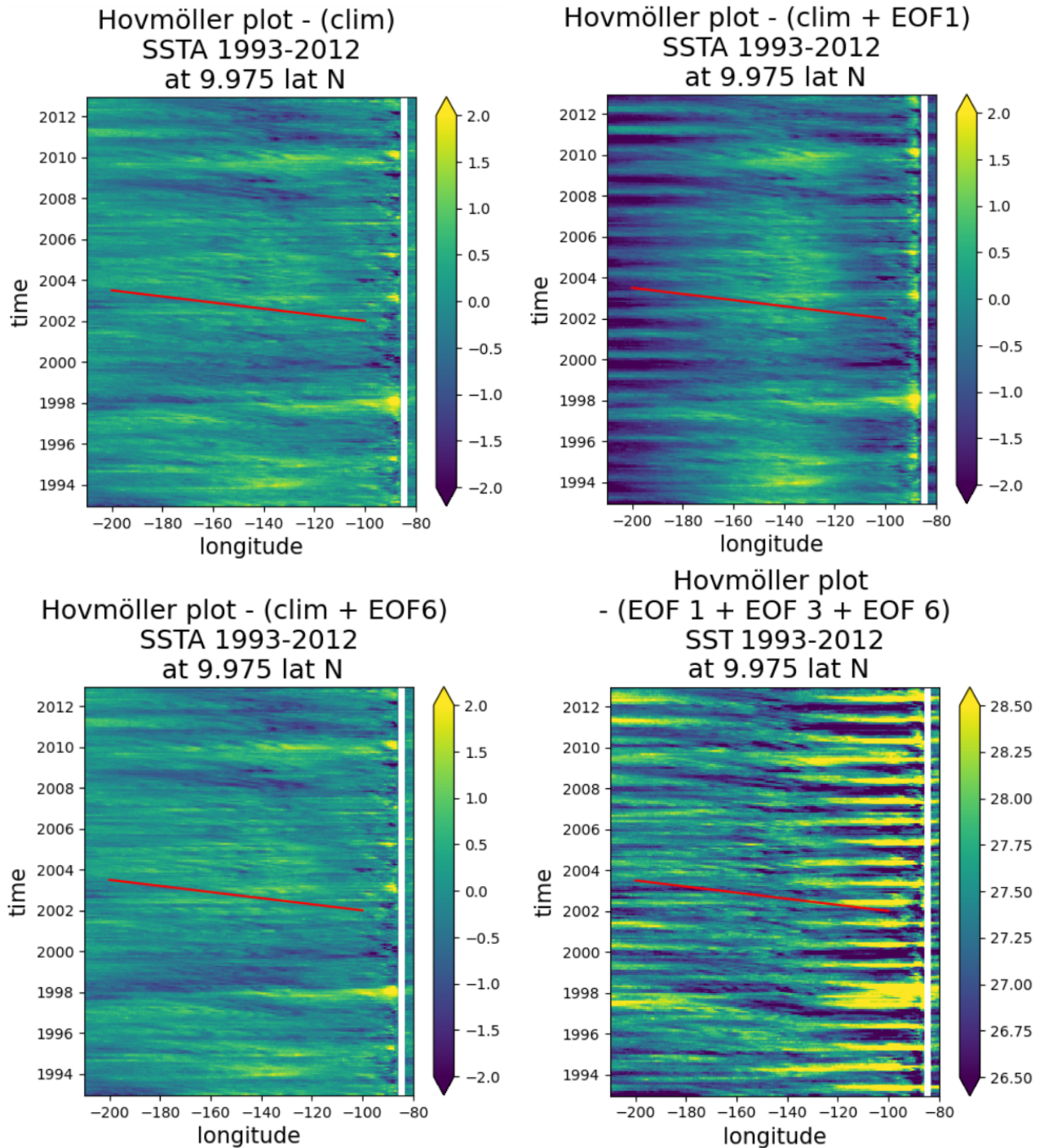
Fig. 25 – Hovmöller diagrams covering 20 years of data between 1993 and 2022 at $10°N$ of latitude. Top left: SST data with subtracted climatology. Top right: SST data with subtracted climatology and also EOF 1. Bottom left: SST data with subtracted climatology and also EOF 6. Bottom right: SST data with subtracted EOF 1, EOF 3 and EOF 6. The units of the color scale are in $°C$. The red line corresponds to the theoretical speed $v_1 \simeq 23cm/s$ at this latitude: in this case, it took 1 year and 6 months for planetary waves to travel from $-100°$ to $-200°$ of longitude.

Fig. 26 – Hovmöller diagrams by intervals of 10 years of SSH data between 1993 and 2022 at 10°N latitude.
Top left: between 1993-2002, top right: between 2013-2012, bottom: between 2013-2022. The red line
indicates the propagation speed calculated with the Radon transform for these different periods of remote
sensing observation (cf next subsection).

by subtracting the EOF 6 there is no large modification, by subtracting the

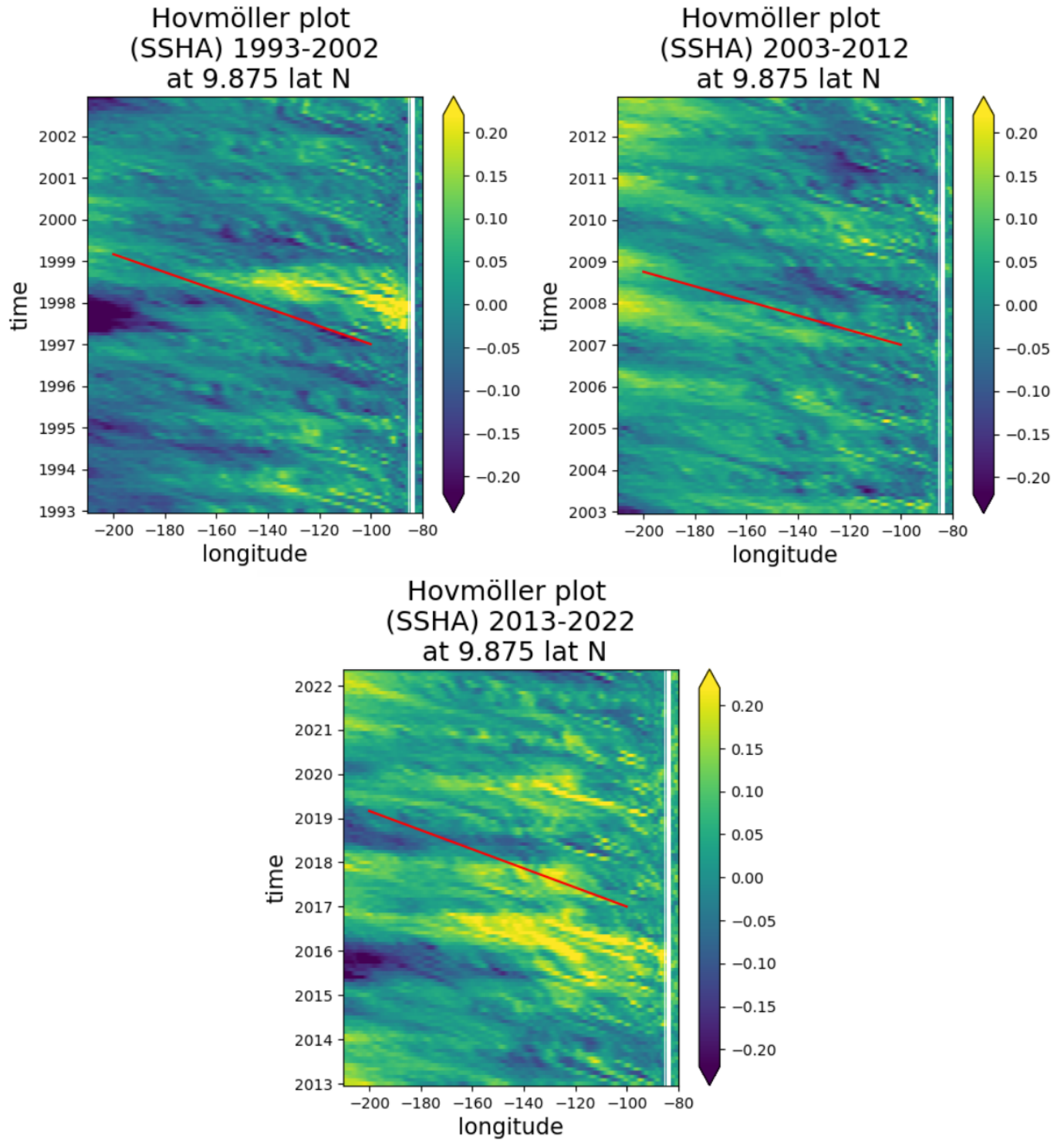EOF 1, 3, 6 without the climatology, lines viewed as signatures of planetary waves are more visible, but it also adds periodic patterns on the east. Unfortunately, the Radon transform did not reveal the speed of the planetary waves from these diagrams with subtracted EOF.

In Fig. 26, Hovmöller diagrams were plotted for periods of 10 years of satellite altimetry, at the constant latitude of $9.875°N$. This could reveal if the propagation speed of planetary waves (for Fig. 26, see speed values in Table 4 in next subsection) varies on a decadal scale. The red straight lines were added on the diagrams after calculation of the propagation speeds (cf next subsection) from the satellite observations. If the slope of the line is higher, the wave propagates more slowly and if the slope of the line is lower, the wave propagates more rapidly. What is expected is that planetary waves propagate more rapidly around $0°$ of latitude than around $10°$ of latitude (β is maximum at the equator and decreases to the poles and the Rossby radius is also higher at the equator), so the slope of the lines will be closer to the horizontal on Hovmöller diagrams at latitudes close to $0°$.

To estimate these speeds, a mathematical and numerical technique called the Radon transform was used. It is the subject of next subsection.

4.4   Radon transform

The propagation speed of the planetary waves can be estimated by measuring the inclination from the horizontal (or from the vertical) of wave lines on an Hovmöller diagram.

The chapters 9, 14 and 15 of the 2D imaging book (BRACEWELL 1995) are a good introduction to the special functions, transforms and projection techniques which are used to the *Radon transform.*
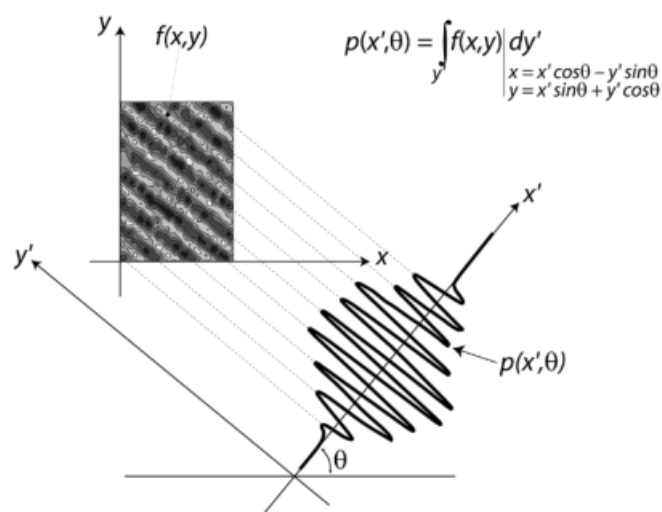

Fig. 27 – Illustration of the Radon transform, in the case of 1D function p(x') for a single orientation θ (from ROBINSON 2010).

This transform was developed by mathematicians, like Johann RADON which published a paper in this subject in 1917, to determine the orientation of alignments in a 2D image, seen as a function of two variables $f(x, y)$. The image is projected to a new frame of axes (x',y') rotated through an angle θ[5] from the original plane (x,y): this is done by calculating $x' = -sin(\theta)x + cos(\theta)y$ if the inclination angle is measured from the horizontal (in the Fig. 27, the (x,y) axis are rotated by θ). One then calculate the sum of the analysed variable along the rotated axis for each θ, called $\mathcal{R}$ hereafter: one sums all the values of the image perpendicularly to the x' axis for each x' to obtain $\mathcal{R}$. The resulting troughs and ridges are well separated for a particular value of θ. For all other values of the inclination angle, the resulting function is smoother and shows no particular structure. By choosing a range of θ, like from 0° to 70° by steps of 1°, one gets the 2D radon transform after evaluating an integral across this range.

---

[5]The definition for θ_{code} that I used in the code is different that the θ_{fig} represented in Fig. 27, by the relation $\theta_{code} = 90° - \theta_{fig}$. But to simplify the lecture, I denoted both by θ in the text.

The final steps of the process are to calculate $\mathcal{P}$ which is the mean of $\mathcal{R}^2$ and then to choose the value of θ which maximizes the Radon transform projection $\mathcal{P}$.
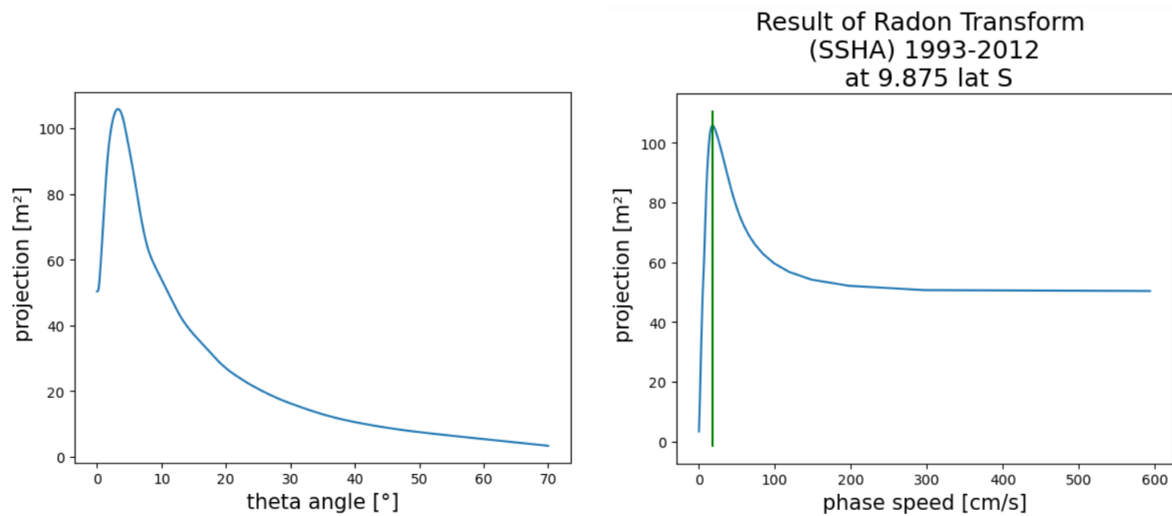
Fig. 28 – Radon transform for SSH anomalies between 1993 and 2012 (20 years of data) at 10°N latitude. Left: projection in function of the θ angle, right: projection in function of the calculated phase speed (only the x-axis is different). The vertical green line indicates the calculated value of the phase speed with the Radon transform.
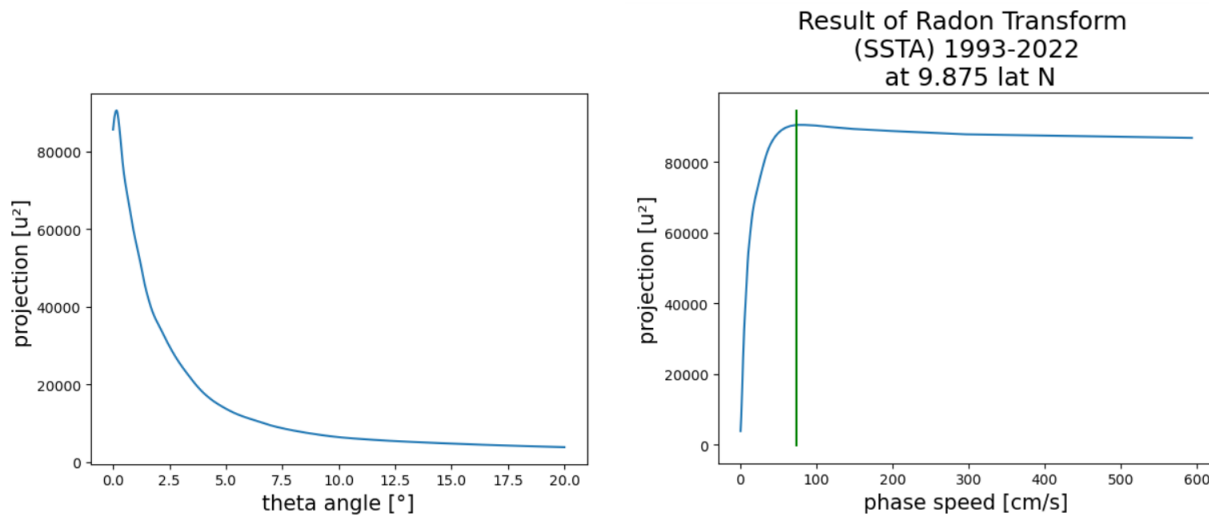
Fig. 29 – Radon transform for SST anomalies between 1993 and 2022 (30 years of data) at 10°N latitude. Left: projection in function of the θ angle, right: projection in function of the calculated phase speed (only the x-axis is different). The vertical green line indicates the calculated value of the phase speed with the Radon transform.

In the left Fig. 28 and Fig. 29, which are plots of the projection in function of the angle, we see a peak corresponding to the more probable orientations. We choose the value of θ which maximizes the projection $\mathcal{P}$, and calculate the

corresponding phase speed by taking into account that $1°$ of longitude $\sim 111\,km$ at the equator, the spatial resolution ($0.25°$ for SSH, $0.05°$ for SST) and temporal resolution (one month).

The speed is then calculated from $v_1 = (tan(\theta))^{-1}\delta x/\delta t$,
where $\delta x = R_{space}\,L_{eq}\,cos(latitude)$ and $\delta t = 2678400s$, with $R_{space} = 0.25$ is the spatial resolution for SSH and $L_{eq} = 111\ 10^3 m$ is the length of $1°$ of longitude at the equator.

Let us notice that it is important to select a large range of longitudes if we want to observe a signature of planetary waves by using the Radon transform: if we choose only a short range, like $[-170°, -120°]$ of longitude, there is no a sufficient amount of data to observe a peak by plotting the projection in function of the θ angle. This is why I could not investigate the variation of propagation speed of 1st baroclinic planetary waves in function of longitude in this work.

4.5 Summary of results

Let us now summarize the results on the westward propagation speeds of 1st baroclinic planetary waves in the region of interest during the period 1993-2022.

Table 3 – Table of the propagation speeds of planetary waves in the equatorial Pacific Ocean at different latitudes during the period 1993-2022, as calculated from SSHA Hovmöller diagrams by the Radon transform. The second column gives the theoretical speed by using the 2.5-layer model presented in section 3, to be compared with the third column which gives the calculated observed speed. The fourth column gives the value of the Rossby radius used to calculate the theoretical speed, the fifth column gives the value of the theta angle used to calculate the observational speed after applying the Radon transform technique.

latitude [°]	theor. speed v_{th} [cm/s]	obs. speed v_{obs} [cm/s]	R [km]	θ [°]
9.875	23	16	176	3.7
7.375	29	18	196	3.3
4.875	37	30	220	2.0
3.625	58	39	275	1.5
2.375	94	74	352	0.8
1.375	122	119	400	0.5
0.125	148	148	440	0.4
-1.375	122	129	400	0.46
-2.375	94	99	352	0.6
-3.625	58	49	275	1.2
-4.875	37	35	220	1.7
-7.375	29	23	196	2.6
-9.875	23	20	176	3.0

The results between theoretical and observed speeds are close enough to conclude that the 2.5-layer model is suitable for the study of oceanic planetary waves and that SSH data is useful to detect planetary waves by satellite altimetry. Unfortunately, I did not detect clearly planetary waves with SST data. Probably it is because the monthly resolution of the data set was not appropriate and to use directly daily SST data could be better to detect it.

Let us notice that the Rossby radius varies with the latitude, as first explained in section 3. The observed propagation speeds (Table 3, Fig. 30 right) are a bit higher in the southern hemisphere than in the northern hemisphere. This could be due to a difference in the stratification in the two hemispheres (so the height of the layers vary, and thus the Rossby radius, which modifies a bit the propagation speed). But this difference between the two hemispheres remains small and the variation of latitude is the main factor impacting the propagation speed of baroclinic Rossby waves, this variation being in theory (Fig. 30 left) symmetric around the imaginary equator line at 0° of latitude, if the stratification is the same in the two hemispheres and if the maximum phase speed corresponds to waves situated exactly at 0° of latitude.
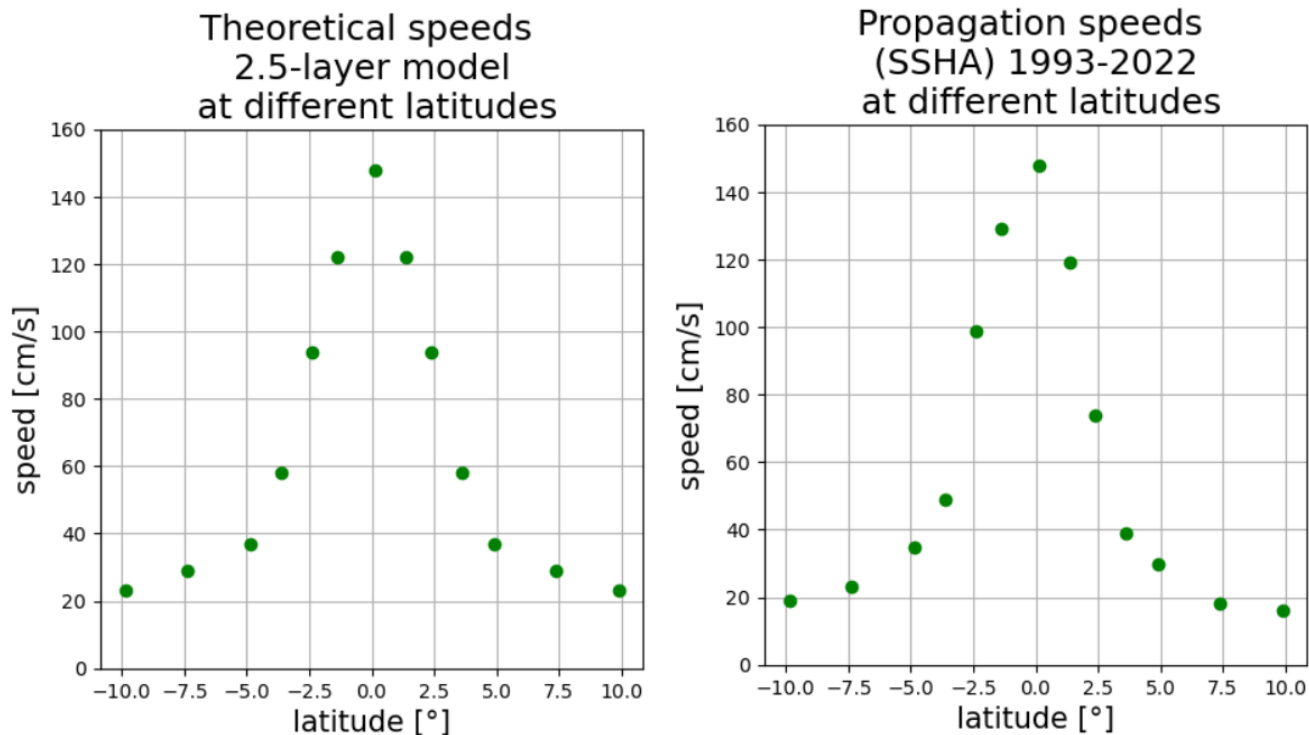
Fig. 30 – Propagation speeds of planetary Rossby waves at different latitudes in the equatorial Pacific Ocean. Left: calculated for a 2.5-layer model with an equatorial Rossby radius of $440km$. Right: calculated for SSH anomalies between 1993 and 2022 by using the Radon transform.
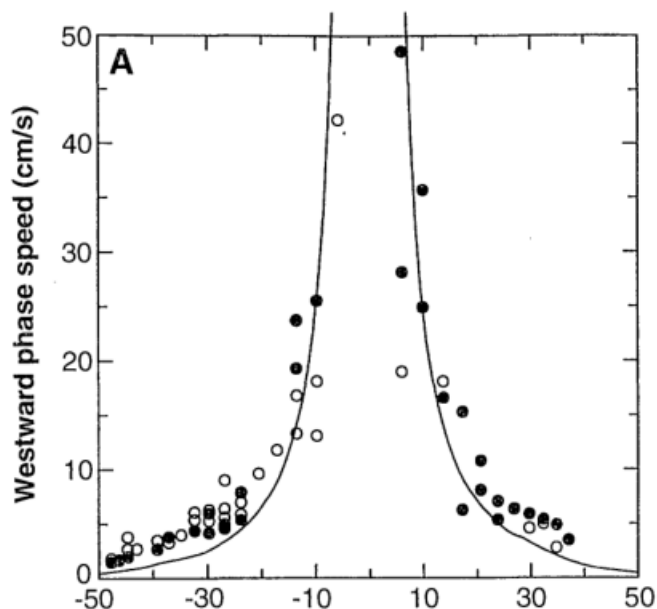
Fig. 31 – Propagation speeds of planetary Rossby waves estimated for SSH anomalies between 1993 and 1996 in function of latitude. The solid circles correspond to estimations for the Pacific Ocean, the open circles correspond to estimations for the Atlantic and Indian Ocean. The continuous line is the latitudinal variation of the phase speed as predicted by the standard linear theory for extratropical 1st baroclinic planetary waves (from CHELTON & SCHLAX 1996).

To compare it with the literature, the Fig. 31 (Chelton & Schlax 1996) obtained from the first results of satellite altimetry with TOPEX/Poseidon shows well that the westward phase speed decreases rapidly out of the equatorial band and speed $\simeq 20cm/s$ at 10° of latitude, with higher speed closer to the equator.

In most of papers about planetary Rossby waves, the propagation speed was not calculated close to the equator (below 10° of latitude), so this master thesis is a good complement to it. It is certainly important to have an order of magnitude of this speed at these small latitudes.

Let us also remember that it is the 1st baroclinic propagation speed (strongly dependent on the stratification) which is observed by most of the actual satellites, and not the speed of (lowest order) barotropic waves which are uniform vertically (so independent of the stratification) and not observable because they propagate too fast. The SSH variations are mirrored as thermocline depth variations of the opposite sign with about three orders of magnitude greater amplitude: a sea level variation of only $10cm$ corresponds to a thermocline displacement of $100m$ (LeBlond & Mysak 1978, Chelton & Schlax 1996). This variation of the ocean structure can have important implications about the role of the ocean in climate variations.

By curiosity, I rapidly looked at the variation of planetary wave speed in function of longitude, by dividing longitudinally my region of interest in 3 zones: from $-210.125°$ to $-170.125°$ (zone A), from $-170.125°$ to $-120.125°$ (zone B), and from $-120.125°$ to $-80.125°$ (zone C). But because this decreases strongly the longitudinal range, only a small amount of this splitted data gave results with the Radon transform. These results are presented in Table 4.

Table 4 – Table of the longitudinal variation of the propagation speeds of planetary waves in the equatorial Pacific Ocean at different latitudes, during the full period 1993-2022. The projection angle is indicated in the third column. The region of interest was divided in 3 zones: from $-210.125°$ to $-170.125°$ (zone A), from $-170.125°$ to $-120.125°$ (zone B), and from $-120.125°$ to $-80.125°$ (zone C). The symbol - means that the Radon transform did not give a value for these parameters.

latitude [°]	speed v_1 [cm/s] (A | B | C)	angle θ [°] (A | B | C)
9.875	(- | - | -)	(- | - | -)
7.375	(- | - | -)	(- | - | -)
4.875	(- | - | -)	(- | - | -)
3.625	(- | 297 | -)	(- | 0.2 | -)
2.375	(23 | 198 | 297)	(2.6 | 0.3 | 0.2)
1.375	(27 | 297 | 297)	(2.2 | 0.2 | 0.2)
0.125	(30 | 297 | 297)	(2.0 | 0.2 | 0.2)
-1.375	(23 | 297 | 297)	(2.6 | 0.2 | 0.2)
-2.375	(18 | 297 | 297)	(3.3 | 0.2 | 0.2)
-3.625	(17 | 297 | -)	(3.5 | 0.2 | -)
-4.875	(- | - | -)	(- | - | -)
-7.375	(- | - | -)	(- | - | -)
-9.875	(- | - | -)	(- | - | -)

We see in Table 4 that we obtain small values of the propagation speed in the western subdivision (zone A) for small latitudes. The very high values $\sim 3.0 m/s$ for the propagation speed obtained in the zones B and C are probably due to climatic events and not properly to the baroclinic planetary waves.

So this confirms that it is important to use a large range of longitudes to detect baroclinic planetary waves from satellite observations by using space-time Hovmöller diagrams and the Radon transform.

Moreover, with my data, I noticed a speed variation on a decadal scale, by comparing the speeds between 1993-2002, 2003-2012 and 2013-2022. This is shown in Table 5.

Table 5 – Table of the propagation speeds of planetary waves in function of latitude by decades. The projection angles between the line and the horizontal varied between 0° and 20°, in steps of 0.1°. The symbol - means that the Radon transform did not give a value for these parameters.

period [years]	latitude [°]	speed v_1 [cm/s]	angle θ [°]
1993-2002	9.875	16	3.6
	7.375	14	4.1
	4.875	25	2.4
	3.625	33	1.8
	2.375	42	1.4
	1.375	49	1.2
	0.125	54	1.1
	-1.375	49	1.2
	-2.375	42	1.4
	-3.625	35	1.7
	-4.875	28	2.1
	-7.375	21	2.8
	-9.875	17	3.5
2003-2012	9.875	20	2.9
	7.375	16	3.7
	4.875	59	1.0
	3.625	118	0.5
	2.375	148	0.4
	1.375	198	0.3
	0.125	198	0.3
	-1.375	198	0.3
	-2.375	198	0.3
	-3.625	148	0.4
	-4.875	-	-
	-7.375	29	2.0
	-9.875	29	2.0
2013-2022	9.875	16	3.7
	7.375	-	-
	4.875	39	1.5
	3.625	54	1.1
	2.375	148	0.4
	1.375	148	0.4
	0.125	198	0.3
	-1.375	198	0.3
	-2.375	148	0.4
	-3.625	85	0.7
	-4.875	54	1.1
	-7.375	45	1.3
	-9.875	29	2.0

We see in Table 5 that the speed of planetary waves at all the latitudes was slower during the first decade of data (1993-2002) and faster during the next two decades (2003-2012 and 2013-2022). Also the speed close to the equator obtained for separated periods 2002-2012 and 2013-2022 was a bit faster than for the complete period 1993-2022.

5 El Niño - Southern Oscillation

The El Niño - Southern Oscillation (ENSO) is an interannual phenomenon in the tropical ocean–atmosphere system. A recurring climate pattern occurs across the tropical Pacific Ocean: El Niño (warm phases) and La Niña (cold phases) events alternate.

5.1 Oceanic Niño index

The NOAA Satellite and Information Service provides timely access to global environmental data from satellites and other sources to monitor and understand our dynamic Earth. Its climate prediction center gives the Oceanic Niño Index (ONI) from 1950 until now.
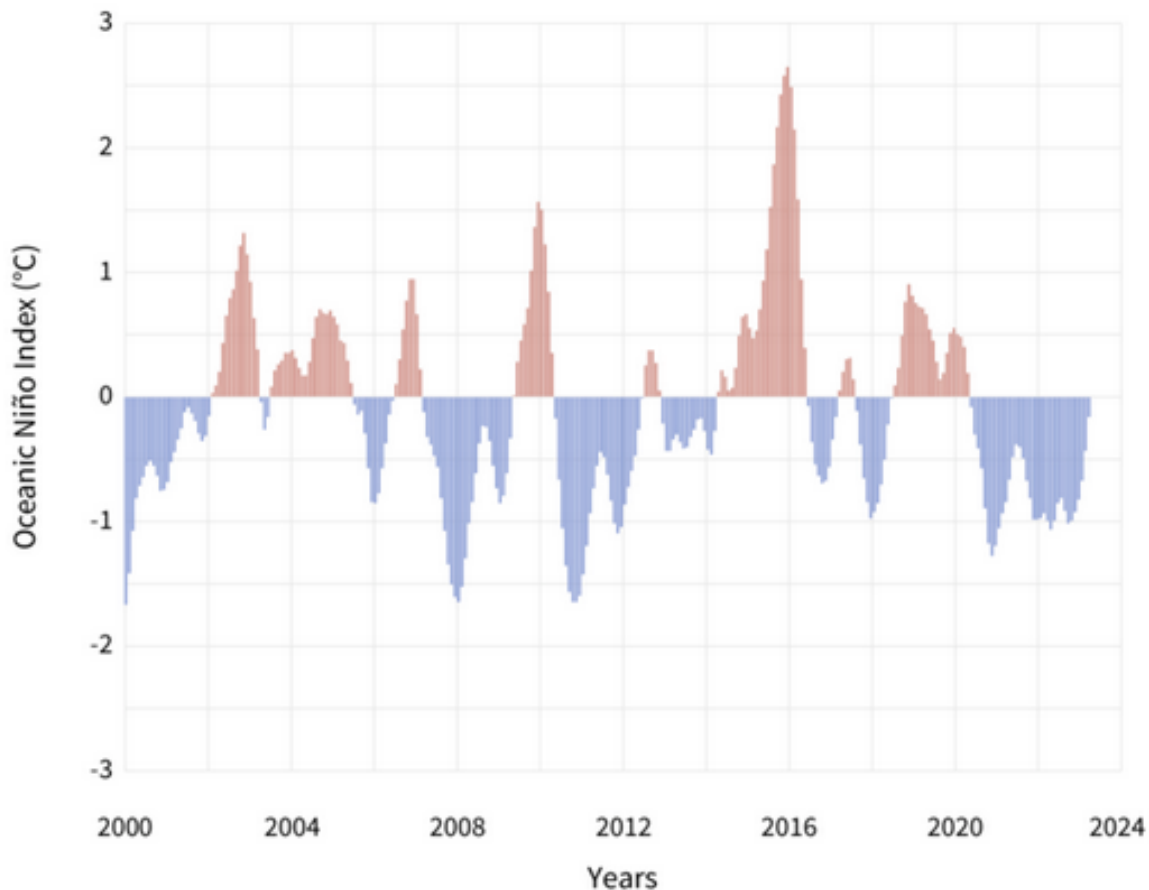

Fig. 32 – ONI: 3-month SST in the equatorial Pacific Ocean in function of time in the period 2000-now, compared to the 1981-2010 average. El Niño occurs for $ONI \geq 0.5°C$ above average and La Niña occurs for $ONI \leq 0.5°C$ below average (from climate.gov).

The ONI tracks the running 3-month average SST in the equatorial Pacific

Ocean, between $120°W$ and $170°W$ (Fig. 33). and quantifies how much warmer or cooler it is than average. It is shown in Fig. 32 for the period 2000-2024.
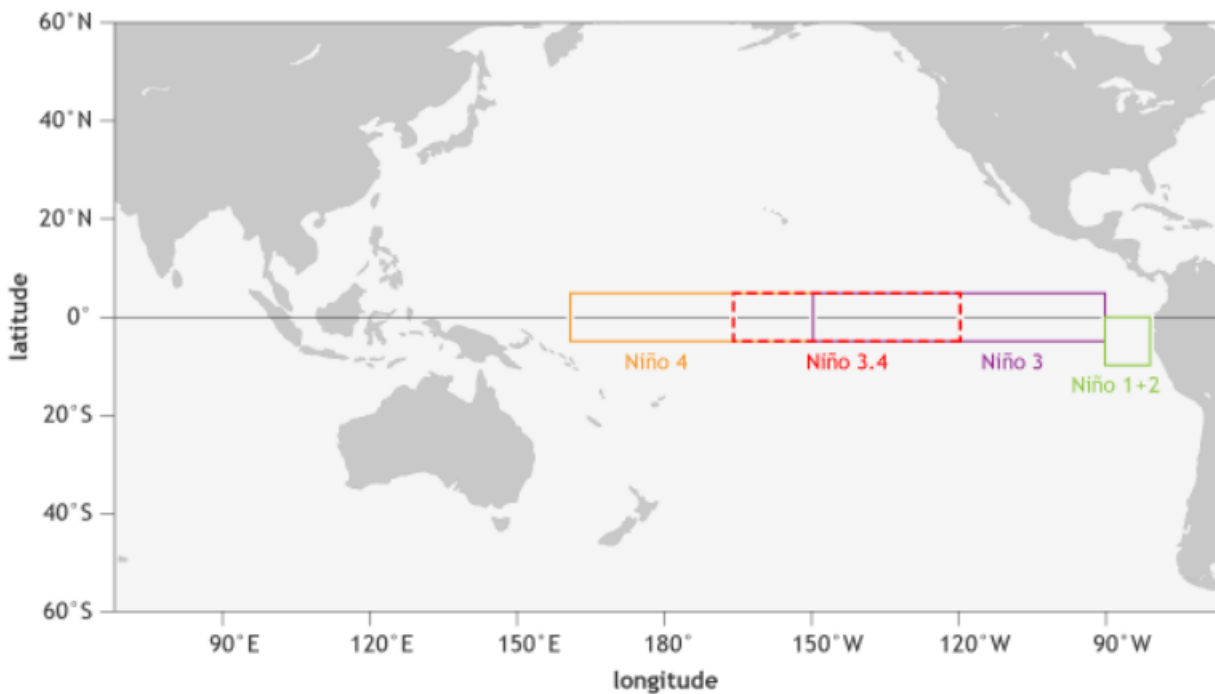

Fig. 33 – Map with the location of the parts of the equatorial Pacific Ocean used for monitoring SST. The Niño 3.4 region (red frame) is the region chosen for the ONI (from climate.gov).

Because of the quasi-periodicity of these events, it is not so easy to predict when will be the next warm or cold event. For example, there were two La Niña events between 2008 and 2012 but only one El Niño event between 2012 and 2018.

Historically, it was observed that the El Niño events were correlated with the Southern Oscillation Index (SOI) used in meteorology. The SOI (defined from surface pressure anomaly) is a measure of the southeast trade winds over the south equatorial Pacific Ocean. There is so an inverse relation between ONI (positive values with El Niño) and SOI (negative values with El Niño). This is the origin of the terminology El Niño - Southern Oscillation (ENSO) for this coupled ocean-atmosphere phenomenon.

5.2 Warm and cold events

El Niño(/La Niña) events are characterized by higher(/lower) SSTA in the equatorial region, but also by higher(/lower) SSHA.

MULTIVARIATE DETECTION AND PROPAGATION SPEED OF PLANETARY ROSSBY
WAVES FROM SATELLITE OBSERVATIONS OF THE EQUATORIAL PACIFIC OCEAN

63

The atmospheric circulation and coupled ocean currents are not anymore in normal conditions (mean climatic state) and became atypical. This pattern of atypical behavior can persist for several months in the equatorial Pacific Ocean (ROBINSON 2010).

The month of December 2015 was characterized by high SSTA and high SSHA: there was an El Niño event, illustrated in Fig. 34.
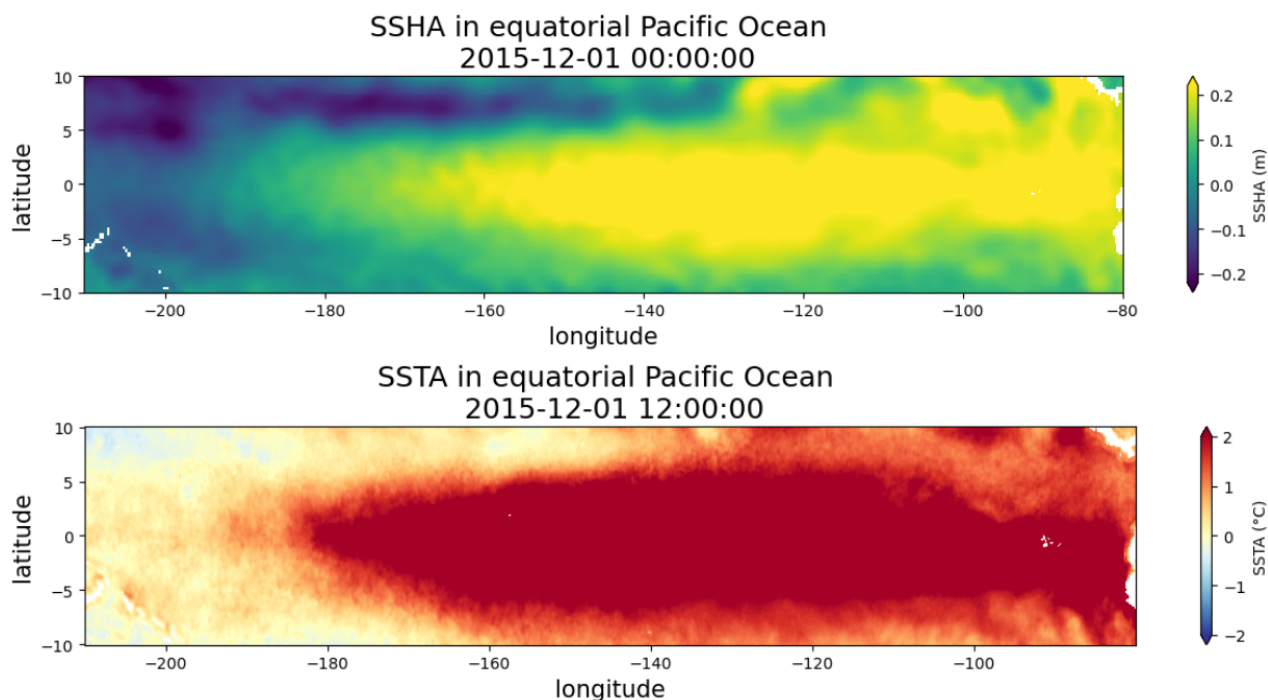

Fig. 34 – Maps of SSHA (top) and SSTA (bottom) for the 1st December 2015, showing an El Niño event.

Conversely, the month of November 2010 was characterized by low SSTA and low SSHA: there was a La Niña event, illustrated in Fig. 35.

Near the equator, the weakening of the trade winds in the western Pacific with the appearance of a warm SST in the central Pacific corresponds to El Niño events. In contrast, La Niña events correspond to the opposite situation with very cold SST in the eastern equatorial Pacific Ocean. Under normal conditions, northeasterlies and southeasterlies converge to the intertropical convergence zone (ITCZ) and blow westward, generating equatorial upwelling over the eastern part of the basin: there are thus warm waters in the west and cold waters in the east (CUSHMAN-ROISIN & BECKERS 2010). El Niño phenomenon has consequences in plankton and fish, but also birds which die due to the suppression of coastal upwelling during these events.
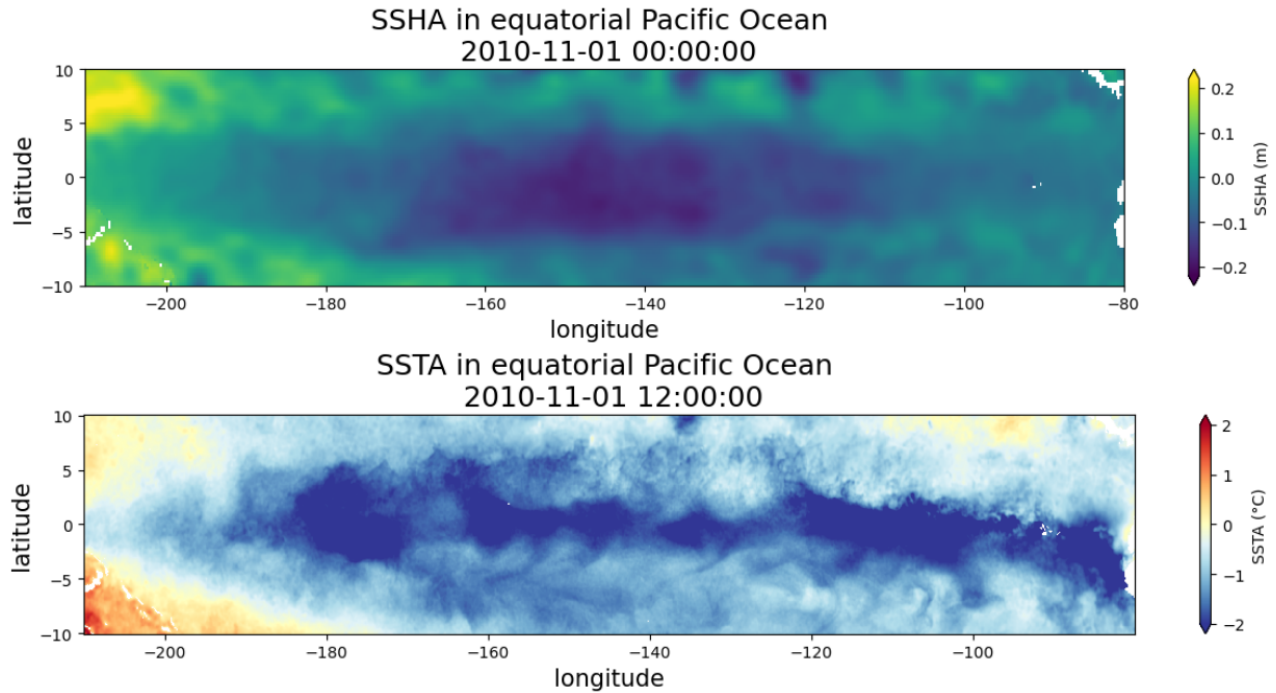
Fig. 35 – Maps of SSHA (top) and SSTA (bottom) for the 1st November 2010, showing a La Niña event.

There is thus a change in the volume of warm water above the thermocline in the equatorial Pacific during these events (Bosc & Delcroix 2008).

In the Hovmöller diagrams presented in section 4, we see clearly the El Niño events of 1998 and 2016 (in yellow). Ideally, it would be better for the data analysis whether we could subtract the ENSO variation (as tried with the EOF for the SST). Because the large EL Niño and La Niña events appear in anomalies, Hovmöller plots of SSHA and SSTA can help to improve the prediction of ENSO events.

Some researchers also do simulations to study the cloud feedbacks on the large-scale circulation with ENSO (Middlemas et al. 2019). There were related studies of SST and surface winds by satellite data, in particular near the Ecuador-Peru coast and in the central equatorial Pacific Ocean (Rasmusson & Carpenter 1982) since some decades. In this context, one can associate oceanic Rossby waves over the equatorial Pacific Ocean with ENSO events (Abe et al. 2014, Abe et al. 2016). In the viewpoint of weather forecast, there is an important coupling between the atmosphere and the ocean, with the Walker circulation.

5.3   Link to planetary waves

The ENSO mechanism is linked to equatorial Kelvin and Rossby waves. By looking at the SSHA, during an El Niño warm event, the characteristic signatures of equatorial Kelvin waves are visible in the east and the characteristic signatures of equatorial Rossby waves in the west. The surface currents are dominated by these trapped equatorial waves in the equatorial Pacific Ocean. At the beginning of an El Niño event, the SSHA is higher at the equator because of equatorial downwelling Rossby waves propagating to the west and the westerly winds induce equatorial downwelling Kelvin waves propagating to the east. Conversely, at the beginning of a la Niña event, the SSHA is lower at the equator because of equatorial upwelling Kelvin waves propagating to the east and the westerly winds induce equatorial upwelling Rossby waves propagating to the west where the sea level decreases. There is a constructive uplifting of the thermocline by equatorial upwelling Kelvin and Rossby waves, so lower SST (PICAUT et al. 2002). The equatorial upwelling is illustrated in Fig. 36 (b)(i).
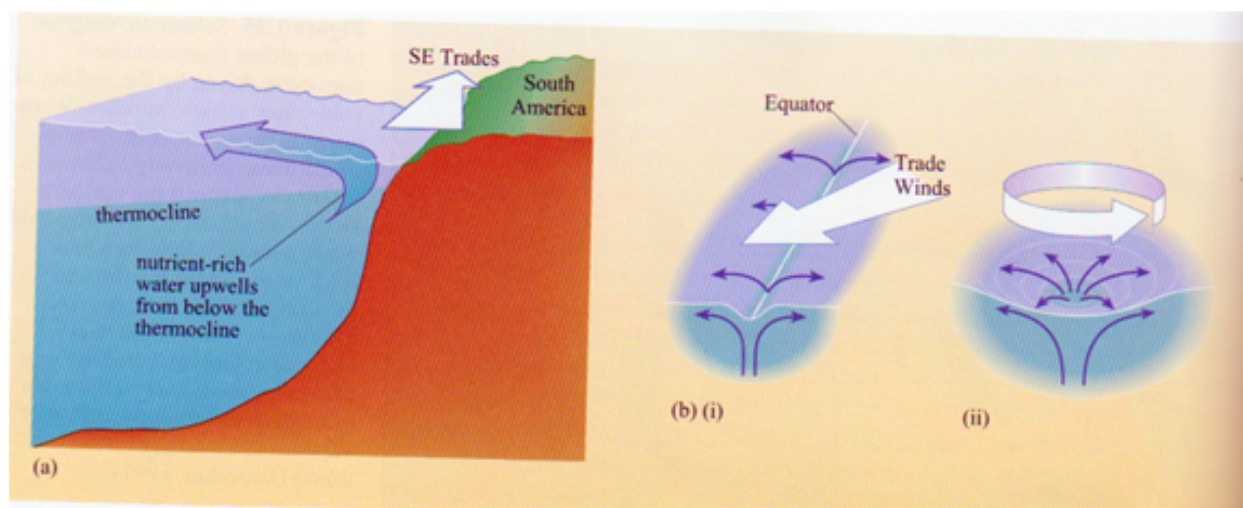
Fig. 36 – Illustration of the different types of oceanic upwelling: (a) coastal upwelling, (b)(i) equatorial upwelling, (b)(ii) cyclonic gyres upwelling (from COCKELL 2008).

1st baroclinic first meridional mode ($m = 1$) equatorial Rossby waves seem to be responsible for the anomalous meridional geostrophic transports of warm water in the Pacific Ocean (BOSC & DELCROIX 2008). In the viewpoint of the geostrophic transports, the downwelling Rossby waves generate meridional geostrophic divergence and upwelling Rossby waves generate meridional geostrophic convergence in the equatorial band. So in the coupled ocean-atmosphere system, the zonal wind forcing has an effect to drive Ekman trans-

port, but it also initiates equatorial Rossby waves.

The variation of the equatorial thermocline depth has an impact on the amplitude of ENSO events. This is usually explained with shallow-water models of oceanic Rossby waves. When there is a strong upwelling of water from below the thermocline at the equator, it can announce a future La Niña event.

MULTIVARIATE DETECTION AND PROPAGATION SPEED OF PLANETARY ROSSBY
WAVES FROM SATELLITE OBSERVATIONS OF THE EQUATORIAL PACIFIC OCEAN

67

6   Discussion: propagation speed

In general, baroclinic planetary waves move slowly, at typical speeds of a few cm/s. Such waves take months to cross an ocean basin at low latitudes, and years to decades at higher latitudes. Some scientists (CHELTON & SCHLAX 1996; KILLWORTH et al. 1997) remarked that the speeds of planetary waves observed by TOPEX/Poseidon at higher latitudes are mainly faster than those given by standard linear theory. But here we focussed on oceanic baroclinic planetary waves at low latitudes, where the standard linear theory is valid.

Both the Earth rotation and the ocean stratification are important for baroclinic planetary waves. Assuming the beta-plane approximation valid, theoretical speeds were estimated by using a 2.5-layer reduced gravity model and by looking on the stratification in the equatorial Pacific Ocean like with a meridional section of potential density by the World Ocean Circulation Experiment (NIKURASHIN & VALLIS 2011).

To answer the three initial questions of the introduction, we can detect the presence of planetary Rossby waves in the ocean by looking at SSH anomalies on a longitude versus time diagram and by applying the Radon transform technique. By constructing a theoretical model with includes both rotation and stratification, we can compare it with satellite observations about the propagation of baroclinic planetary waves. And the propagation speed of these waves varies with the latitude, decreasing from the equator to the mid-latitudes, but also it can vary on a decadal scale due to changes in the stratification or variation of the winds during climatic events.

The principles of the Hovmöller plots and the Radon transform are introduced in a reference book (ROBINSON 2010). We can apply the Radon transform to the study of planetary waves and obtain the alignment of planetary waves signatures in Hovmöller plots. Thanks to this method, we can analyze entire ocean basins or specific regions like here the equatorial region in the Pacific Ocean to identify the occurrence of planetary waves and to map their westward propagation speed.

Comparison between theory and satellite observations on the speed of waves were done in the Atlantic and Pacific basins and are available in the literature (KILLWORTH & BLUNDELL 1999), but usually it is a 1.5-layer or 2-layer model which is used in the theory. The 2.5-layer model assumes two active

layers instead of one. This can take into account motions in opposite directions in different layers and we know there is an equatorial countercurrent, but also an equatorial undercurrent at larger depth. I think the motion of the water layer below the thermocline can also impact these currents. So there are an effect visible at the surface with the 1st but also with the 2nd order baroclinic waves, which are better taken into account with the 2.5-layer model. Thus the 2.5-layer model used here is an improvement in this regard. The variation of the Rossby radius, chosen here at a higher value ($440km$) than in previous studies, is also an important point. This higher value comes from taking into account the 2nd active layer with a $800m$ thickness below the 1st active layer with a $200m$ thickness. The higher observed values of the propagation speeds in the southern hemisphere (in comparison with the northern hemisphere) can also be explained by a higher thickness of the 1st active layer in the equatorial Pacific Ocean (Fig. 2 (b)): if this height is higher, the Rossby radius is higher and also the propagation speed.

The more successful tool to detect oceanic planetary waves is by satellite altimetry. Some research groups (Hill et al. 2000, Cipollini et al. 2001, Heffner et al. 2008) also found detection by using other variables than SSH (SST, SSS, CHL), but it is clearer with the SSH. In this master thesis, the Radon transform technique worked well with SSH data, but not well with SST data. This is probably due to the chosen temporal resolution of anomalies (monthly instead of daily) and to precision of the instruments: the altimeter coverage is ideal for the detection of surface signatures of baroclinic planetary waves, with SSHA of a few centimeters, and so are observable to the accuracy of the altimeter. Or it could also be due to the combined variability of SST from different instruments: thermal-IR radiometers (measuring skin SST) and microwave radiometers (measuring sub-skin SST). Combining data from different instruments is good, but the accuracy is not always on the same order. In the beginning, the idea was also to look at salinity (SSS) or ocean color (CHL) and this could be investigated in further work. In that case, if the propagation speeds between different variables look similar, a multivariate Radon transform could be done.

The propagation speed of 1st baroclinic Rossby waves at $10°S$ in the Pacific Ocean was estimated at $v_1 \sim 20cm/s$, at $5°S$ it was $35cm/s$, at $2.5°N$ it was $100cm/s$, at $0°N$ it was $150cm/s$. A close correspondence was obtained between

the theoretical speed values from the 2.5-layer model and the observational speed values from SSH data for the period 1993-2022 by using the Hovmöller diagrams & the Radon transform.

Outside the equatorial zone, the wave speed reduces with increasing latitude and this latitude dependence of speed can be compared with theoretical predictions. Moreover, the wave speed could also vary with longitude: in general, it increases toward the west of ocean basins (HILL et al. 2000). But this aspect could not be investigated (because the Radon transform needs a large range of longitudes) in this master thesis where we principally looked at a constant latitude on all the available longitudes for the equatorial Pacific Ocean. So this aspect of variation with longitude could be further investigated by looking on smaller areas at different longitudes and then compute the observed propagation speeds by another technique than by the Radon transform as done here.

The climatology was mapped and then subtracted for the 30 years of satellite data to obtain SSH and SST anomalies. El Niño/La Niña events were observed by the SSHA and SSTA during this study, with some events appearing stronger in some years (like the strong El Niño in 1997-1998). This aspect could be important for the scientists trying to predict next large warm/cold events in the ocean-atmosphere system. These events impact the marine and human populations: the impact of ENSO events affects the marine fauna and the coastal fisheries in the equatorial Pacific Ocean (like in the Galápagos islands and near the coast of Peru). But we did not identify here a direct relation between these events and a possible future strong variation on the propagation speed of planetary waves. It could be the case if there is a significant change in the ocean stratification. The stratification can change with time for example if the salinity increases and the water density increases. Or conversely, if the mean surface temperature increases because of climate change, the water density decreases at the sea surface. Its consequence on the speed of Rossby waves could be an increase of the speed because in this case, the density differences between active layers are greater and so the reduced gravity takes a higher value, increasing the Rossby radius and the propagation speed.

A better knowledge of the propagation speed of planetary waves in the equatorial Pacific Ocean can help the scientific community to understand better the phenomena occurring in the equatorial band in the ocean, possibly previsions of the reflection of waves on the coast which then propagate in direction to

the opposite edge of the basin during long periods (because of the slow phase speed) or improve the prevision of ENSO events in the climate system by detecting the variable anomalies, as possible perspectives of this master thesis. Just to mention it, there are other large-scale phenomena not discussed here like tropical instability waves or equatorial Kelvin waves which also occur at the equator.

To close this discussion, a natural phenomenon like the propagation of a particular type of waves in an atmosphere or an ocean can be characterized through the direction and phase speed, by the knowledge of rotation and stratification properties of the body like here the Earth planet. The Rossby waves were investigated a series of papers in geophysics in the sixties (Matsuno 1966, Lindzen 1967), but the geophysics & oceanography research continues (Cipollini et al. 2001, Abe et al. 2014, Belonenko et al. 2016, Wang et al. 2023) where the relation with climatic events and the decadal variation became studied. As noted in the introduction, the Rossby waves were also detected in astrophysical bodies and are referred as r-modes in asteroseismology. So this master thesis shows that the planetary Rossby waves are observed and detected by artificial satellites which are more and more numerous around our planet and studied by oceanographers, meteorologists and remote sensing scientists.

References

Articles

ABE H. et al., *Oceanic Rossby waves induced by the meridional shift of the ITCZ in association with ENSO events*, J. Oceanogr. 70, 165 (2014).

ABE H. et al., *Oceanic Rossby waves over eastern tropical Pacific of both hemispheres forced by anomalous surface winds after mature phase of ENSO*, J. Phys. Oceanogr. 46, 3397 (2016).

ALBEKIONI M. et al., *Rossby waves on stellar equatorial beta planes: Uniformly rotating radiative stars*, Astron. Astrophys. 671, A91 (2023).

ALVERA-AZCARATE A. et al., *Reconstruction of incomplete oceanographic data sets using empirical orthogonal functions: application to the Adriatic Sea surface temperature*, Ocean Model. 9, 325 (2005).

ALVERA-AZCARATE A. et al., *Multivariate reconstruction of missing data in sea surface temperature, chlorophyll, and wind satellite fields*, J. Geophys. Res. 112, C03008 (2007).

ALVERA-AZCARATE A., BARTH A., *The surface circulation of the Caribbean Sea and the Gulf of Mexico as inferred from satellite altimetry*, J. Phys. Oceanogr. 39, 640 (2009).

BANKS C.J. et al., *Reduced ascending/descending pass bias in SMOS salinity data demonstrated by observing westward-propagating features in the South Indian Ocean*, Remote Sens. Environ. 180, 154 (2016).

BECKERS J-M., RIXEN M., *EOF calculations and data filling from incomplete oceanographic datasets*, J. Atmos. Ocean. Tech. 20, 1839 (2003).

BECKERS J-M. et al., *A method to generate fully multi-scale optimal interpolation by combining efficient single process analyses, illustrated by a DINEOF analysis spiced with a local optimal interpolation*, Ocean Sci. 10, 845 (2014).

BELONENKO T.V. et al., *Spectral characteristics of Rossby waves in the northwestern Pacific based on satellite altimetry*, Izvestiya, Atmospheric and Oceanic Physics 52, 920 (2016).

BELONENKO T.V. et al., *Horizontal advection of temperature and salinity by Rossby waves in the North Pacific*, Int. J. Remote Sens. 39, 2177 (2018).

BELONENKO T.V. et al., *Detection of waveguide for Rossby waves using satel-*

lite altimetry in the Antarctic Circumpolar Current, Int. J. Remote Sens. 41, 6232 (2020).

BOSC C., DELCROIX T., *Observed equatorial Rossby waves and ENSO-related warm water volume changes in the equatorial Pacific Ocean*, J. Geophys. Res. 113, C06003 (2008).

BRYDEN H.L., BRADY E.C., *Diagnostic model of the three-dimensional circulation in the upper equatorial Pacific Ocean*, J. Phys. Oceanogr. 15, 1255 (1985).

CABARCOS E. et al., *High-resolution productivity record and reconstruction of ENSO dynamics during the Holocene in the Eastern Equatorial Pacific using coccolithophores*, The Holocene 24, 176 (2014).

CHELTON D.B., SCHLAX M.G., *Global observations of oceanic Rossby waves*, Science 272, 234 (1996).

CHELTON D.B. et al., *Geographical variability of the first baroclinic Rossby radius of deformation*, J. Phys. Oceanogr. 28, 433 (1998).

CHELTON D.B. et al., *Satellite microwave SST observations of transequatorial tropical instability waves*, Geophys. Res. Lett. 27, 1239 (2000).

CIPOLLINI P. et al., *Rossby waves detected in global ocean colour data*, Geophys. Res. Lett. 28, 323 (2001).

DAMIANI C. et al., *Rossby modes in slowly rotating stars: depth dependence in distorted polytropes with uniform rotation*, Astron. Astrophys. 637, A65 (2020).

EMERY W.J. et al., *Geographic and seasonal distributions of Brunt-Väisälä frequency and Rossby radii in the North Pacific and North Atlantic*, J. Phys. Oceanogr. 14, 294 (1984).

HIDE R., *Jupiter's great red spot*, Scientific American, 74 (1968).

HILL K.L., ROBINSON I.S., CIPOLLINI P., *Propagation characteristics of extratropical planetary waves observed in the ATSR global sea surface temperature record*, J. Geophys. Res. 105, 21,927 (2000).

HEFFNER D.M. et al., *Indian Ocean Rossby waves detected in HYCOM sea surface salinity*, Geophys. Res. Lett. 35, L03605 (2008).

HOVMÖLLER E., *The trough-and-ridge diagram*, Tellus 1, 62 (1949).

JACOBS G.A. et al., *Rossby waves in the Pacific Ocean extracted from Geosat*

atimeter data, J. Phys. Oceanogr. 23, 1155 (1993).

JANICOT S. et al., *The dynamics of the west African monsoon. Part V: The detection and role of the dominant modes of convectively coupled equatorial Rossby waves*, J. Climate 23, 4005 (2010).

KILLWORTH P.D. et al., *The speed of observed and theoretical long extratropical planetary waves*, J. Phys. Oceanogr. 27, 1946 (1997).

KILLWORTH P.D., BLUNDELL J.R., *The effect of bottom topography on the speed of long extratropical planetary waves*, J. Phys. Oceanogr. 29, 2689 (1999).

KILLWORTH P.D. et al., *Physical and biological mechanisms for planetary waves observed in satellite-derived chlorophyll*, J. Geophys. Res. Atmos. 109, C07002 (2004).

LEE T. et al., *Aquarius reveals salinity structure of tropical instability waves*, Geophys. Res. Lett. 39, L12610 (2012).

LINDZEN R.D., *Planetary waves on beta-planes*, Monthly Weather Rev. 95, 441 (1967).

MATSUNO T., *Quasi-geostrophic motions in the equatorial area*, J. Meteorol. Soc. Japan 44, 25 (1966).

MENEZES V.V. et al., *Aquarius sea surface salinity in the South Indian Ocean: Revealing annual-period planetary waves*, J. Geophys. Res. 119, 3883 (2014).

MIDDLEMAS E.A. et al., *Cloud radiative feedbacks and El Niño-Southern Oscillation*, J. Climate 32, 4661 (2019).

NIKURASHIN M., VALLIS G., *A theory of deep stratification and overturning circulation in the ocean*, J. Phys. Oceanogr. 41, 485 (2011).

PAPALOIZOU J. & PRINGLE J.E., *Non-radial oscillations of rotating stars and their relevance to the short-period oscillations of cataclysmic variables*, Mon. Not. R. Astr. Soc. 182, 423 (1978).

PEDLOSKY J., *An inertial theory of the equatorial undercurrent*, J. Phys. Oceanogr. 17, 1978 (1987).

PICAUT J. et al., *Mechanisms of the 1997–1998 El Niño–La Niña, as inferred from space-based observations*, J. Geophys. Res. 107, C5-3037 (2002).

PROVOST J. et al., *Low frequency oscillations of a slowly rotating star: Quasi-toroidal modes*, Astron. Astrophys. 94, 126 (1981).

MULTIVARIATE DETECTION AND PROPAGATION SPEED OF PLANETARY ROSSBY
WAVES FROM SATELLITE OBSERVATIONS OF THE EQUATORIAL PACIFIC OCEAN

ix

RASMUSSON E.M., CARPENTER T.H., *Variations in tropical sea surface temperature and surface wind fields associated with the southern oscillation/El Niño*, Mon. Weather Rev. 110, 354 (1982).

ROSSBY C-G. et al., *Relation between variations in the intensity of the zonal circulation of the atmosphere and the displacements of the semi-permanent centers of action*, J. Mar. Res. 2, 38 (1939).

ROSSBY C-G., *On the propagation of frequencies and energy in certain types of oceanic and atmospheric waves*, J. Meteorol. 2, 187 (1945).

SAIO H. et al., *Theory and evidence of global Rossby waves in upper main-sequence stars: r-mode oscillations in many Kepler stars*, Mon. Not. R. Astr. Soc 474, 2774 (2018).

SUBRAHMANYAM B. et al., *Detection of Rossby waves in multi-parameters in multi-mission satellite observations and HYCOM simulations in the Indian Ocean*, Remote Sens. Environ. 113, 1293 (2009).

WANG J. et al., *Interdecadal variation of atmospheric equatorial Rossby waves during boreal summer*, Atmos. Res. 290, 106782 (2023).

WHITE W.B. et al., *Coupling of biennial oceanic Rossby waves with the overlying atmosphere in the Pacific basin*, J. Phys. Oceanogr. 28, 1236 (1998).

YIN X. et al., *SMOS sea surface salinity signals of tropical instability waves*, J. Geophys. Res. Oceans 119, 7811 (2014).

Websites

Climate variability: oceanic Niño index, https://www.climate.gov, consulted on 2023-08-14.

Cold & warm episodes by season, https://origin.cpc.ncep.noaa.gov, consulted on 2023-08-14.

How altimetry works?, https://cnes.fr/en/how-altimetry-works, consulted on 2023-08-14.

Product tutorial on sea surface temperature, https://resources.eumetrain.org, consulted on 2023-08-14.

Which levels are used for data processing?, https://help.marine.copernicus.eu, consulted on 2023-08-14.

Books

BRACEWELL R.N., *Two-dimensional imaging*, Prentice-Hall, 689p (1995).

COCKELL C., *An introduction to the Earth-Life system*, 326p (2008).

COLLING A., *Ocean circulation*, Open university course team, 2nd edition, 286p (2004).

CURRY J.A., WEBSTER P.J., *Thermodynamics of atmospheres and oceans*, 471p (1999).

CUSHMAN-ROISIN B., BECKERS J-M., *Introduction to geophysical fluid dynamics. Physical and numerical aspects.*, 786p (2010).

ELACHI C., VAN ZYL J., *Introduction to the physics and techniques of remote sensing*, 3rd edition, 534p (2021).

KLINGER B.A., HAINE T.W.N., *Ocean circulation in three dimensions*, 484p (2019).

LAU W.K.M., WALISER D.E., *Intraseasonal variability in the atmosphere–ocean climate system*, 2nd edition, 613p (2012).

LEBLOND P.H., MYSAK L.A., *Waves in the ocean*, 602p (1978).

MERLE J., *Océan et climat*, 222p (2006).

PEDLOSKY J., *Geophysical fluid dynamics*, 2nd edition, 732p (1987).

PEDLOSKY J., *Theoretical developments in ocean circulation theory*, 124p (1991).

PEDLOSKY J., *Ocean circulation theory*, 453p (1998).

ROBINSON I.S., *Measuring the oceans from space. The principles and methods of satellite oceanography*, 667p (2004).

ROBINSON I.S., *Discovering the ocean from space. The unique applications of satellite oceanography*, 678p (2010).

STEWART R.H., *Introduction to physical oceanography*, 354p (2008).

VALLIS G.K., *Atmospheric and oceanic fluid dynamics. Fundamentals and large-scale circulation*, 1st edition, 745p (2006).

VALLIS G.K., *Atmospheric and oceanic fluid dynamics. Fundamentals and large-scale circulation*, 2nd edition, 946p (2017).